Mathematical Model and Calendar Aging Study of Commercial Blended-Cathode Li-ion Batteries

by

Zhiyu Mao

A thesis
presented to the University of Waterloo
in fulfillment of the
requirements for the degree of
Doctor of Philosophy
in
Chemical Engineering

Waterloo, Ontario, Canada, 2016

AUTHOR'S DECLARATION

I hereby declare that I am the sole anthor of this thesis. This is a true copy of the thesis, including

any required final revisions, as accepted by my examiners.

I understand that my thesis may be made electronically available to the public.

Abstract

Commercial blended-cathode Li-ion battery (LIB) systems has been dominating the burgeoning market for portable energy, ranging from consumer electronics to automotive applications. In order to successively improve the energy-power density and usage life of blended-cathode cells, an understanding in terms of the electrode design, electrochemical performance, and cell aging are necessary. A mathematical model based research approach is effective to quantitatively estimate all factors in the complicated system has been developed in this work, which will be beneficial for research and development of Lithium ion battery technology.

In this thesis, a model based composition prediction technology for the of unknown commercial blended Li-ion battery cathodes is developed. It includes three steps of combined experimental and modeling methods. The electrochemically active constituents of the electrode are first determined by coupling information from low-rate galvanostatic lithiation data, and correlated with Scanning Electron Microscope (SEM) with Energy Dispersive X-Ray Analysis (EDX) analyses of the electrode. In the second step, the electrode composition is estimated using a physics based mathematical model of the electrode. The accuracy of this model based approach has been assessed by comparison of this electrode composition with the value obtained from an independent, non-electrochemical experimental technique involving the deconvolution of X-ray powder diffraction (XRD) spectra.

Based on the prediction technology, the commercial LIB with the composition of $LiNi_xMn_yCo_{1-x-y}O_2$ - $LiMn_2O_4$ (NMC-LMO=70:30 wt%) cathode was accurately delineated. Then, a physics based mathematical model, including the two dimensions of single particle and

electrode levels, is developed to describe the electrochemical performance of the NMC-LMO blended cathode. The model features multiple particle sizes of the different active materials and incorporates three particle-size distributions: one size for the LMO particles, one size for the NMC primary and one size for NMC secondary particles which presumably are agglomerates of NMC primary particles. The good match between the simulated and experimental galvanostatic discharge and differential-capacity curves demonstrates that the assumption of secondary particles being nonporous (i.e., solid-state transport) is reasonable under the operating conditions of interest in this case up to 2C applied current. In the modeling, a thermodynamic expression for diffusive flux and some parameters such as the effective electronic conductivity have been described and measured. A sensitivity of the fitted model parameters including kinetic rate constants and solid-state diffusivities has been analyzed.

Using the multi-particle model, the different Galvanostatic Intermittent Titration Technology (GITT) experiments with varying pulse currents and relaxation periods for a NMC-LMO blended lithium-ion electrode have been described. The good agreement between the simulated and experimental potential-time curves shows that the model is applicable for all GITT conditions considered, but is found to be more accurate for the case of small current pulse discharges with long relaxation times. Analysis of the current contribution and the solid-state surface concentration of each active component in the blended electrode shows a dynamic lithiation/delithiation interaction between the two components and between micron and submicron NMC particles during the relaxation periods in the GITT experiments. The interaction is attributed to the difference in the equilibrium potentials of the two components at any given

stoichiometry which redistributes the lithium among LMO and NMC particles until a common equilibrium potential is reached.

Moreover, the model can also be used to fit the galvanostatic charge curves from the rate of C/25 to 2C by adjusting model parameters. Through the comparative study with galvanostatic discharge experiment, the asymmetry of capacity contribution of each component during both charge and discharge, i.e., LMO contribution increases during discharging but decreases during charging when the C-rate is raised. Dynamic analysis of the blended cathode shows that this asymmetric charge/discharge behavior of the blended electrode can be attributed to the difference in the equilibrium potentials of the two components depending on Li concentration and electrode composition and to the difference in the rate of solid-state diffusion of Li and kinetics limitations in LMO and NMC.

At last, a calendar life under various aging conditions has been studied, including analysis at various states of charge (SOC) i.e., 35℃-0% SOC, 58℃-0% SOC, 35℃-100% SOC and 58℃-100% SOC, for a commercial NMC-LMO/graphite blended lithium-ion battery. Through the analysis of post-mortem for the 280 days aged cell at 58℃-100% SOC with the remaining capacity of 55%, the loss of cycleable lithium is the predominant reason of capacity loss, which can lead to a passivation layer formation on the surface of graphite and gas generation. The fitting result of 'open circuit voltage (OCV)-model' indicates the about 40% active materials have not been utilized due to the lack of cycleable lithium and gas generation in the aged pouch cell. A non-destructive pressure-loading experiment has been implemented, which demonstrated a recovery of the capacity of the aged cell by 21%, and the reason of redistribution of gas bubbles under pressure inside the pouch cell has been described in detail.

Acknowledgements

Firstly of all, I would like to sincerely thank my supervisors Prof. Michael Fowler and Prof. Zhongwei Chen, and advisor Prof. Mark Pritzker, for their remarkable guidance and unyielding support during my entire PhD study. Also, I would like to thank my PhD thesis examination committee members: Prof. Mark Pritzker, Prof. Aiping Yu, Prof. Patricia Nieva and Prof. Jeff Dahn for their time, effort and valuable discussions.

Special thanks to all of my group members for their support and assistance. I will never forget their kindness and enthusiasm for their research and every happy moment shared with them.

Also, I am greatly thankful for my parent's unyielding support. Without their understanding and inspiration, I have never gained this.

Table of Contents

List of Figures

List of Tables

Nomenclature

A cathode area (m^2)

$a_{n,m}$ specific surface area of active *material n* with particle size class m (m^{-1})

$c_{n,m}$ Li ion concentration in active material n with particle size class m (mol m^{-3})

c_e Li ion concentration in electrolyte (mol m^{-3})

c_T total Li ion concentration in electrolyte (mol m^{-3})

c_n^{max} maximum concentration of Li within active material n (mol m^{-3})

$\mathcal{D}_n$ solid-phase binary diffusion coefficient in active material n ($m^2 s^{-1}$)

$\mathcal{D}_e$ diffusion coefficient of electrolyte based on a thermodynamic driving force, ($m^2 s^{-1}$)

$D_{n,m}$ Li ion solid-phase diffusion coefficient in active material n with particle size class m ($m^2 s^{-1}$)

$D_{eff,sep}$ effective diffusion coefficient of electrolyte in separator ($m^2 s^{-1}$)

$D_{eff,cat}$ effective diffusion coefficient of electrolyte in cathode ($m^2 s^{-1}$)

D_e bulk diffusion coefficient in the electrolyte ($m^2 s^{-1}$)

E cell potential (V)

F Faraday constant (96480 C mol^{-1})

$f_\pm$ mean molar activity coefficient of inorganic salt in electrolyte

I applied current (A)

$i_{n,m}^0$ exchange current density for lithiation/delithiation on active material n with particle size class m (A m^{-2})

i_1 solid-phase current density (A m^{-2})

i_2 liquid-phase current density (A m^{-2})

$i_{n,m}$ faradaic current density on active material n with particle size class m (A m^{-2})

i_f^0 exchange current density for charge transfer reaction on Li foil (A m^{-2})

k_n rate constant (mol m^{-2} s^{-1}(mol m^{-3})$^{-3/2}$)

L electrode thickness (m)

L_{sep} separator thickness (m)

Q cathode capacity (Ah)

q_n practical capacity of type n particle (Ah kg^{-1})

$R_{n,m}$ particle radius of active material n with size class m (m)

R gas constant (8.314J mol^{-1}K^{-1})

r radial distance within a particle of active material (m)

T absolute temperature (K)

t time(s)

t_+^0 lithium ion transference number

$U_{n,m}$ equilibrium potential for lithiation/delithiation on active material n with particle size class m (V)

$y_{n,m}$ lithium content in active material n with particle size class m

Greek

$\alpha_{n,m}$ solid-state thermodynamic factor of active material n with particle size class *m*

β_n charge-transfer coefficient for lithiation/delithiation on active material *n*

β_f charge-transfer coefficient for charge transfer reaction at lithium foil electrode

γ Bruggeman exponent

ξ total volume fraction of all cathode active material in the electrode

$\xi_{n,m}$ volume fraction of active material n with particle size class *m*

$\xi'_{n,m}$ mass fraction of active material n with particle size class *m*

ε_{cat} porosity of cathode

ε_{sep} porosity of separator

$\eta_{n,m}$ surface overpotential on active material n with particle size class *m*   (V)

κ electrolyte ionic conductivity (S m^{-1})

$\kappa_{eff,cat}$ effective ionic conductivity in blended electrode (S m^{-1})

ρ_n density of type *n* particle (kg m^{-3})

σ_{eff} effective electronic conductivity in blended electrode (S m^{-1})

Φ_1 solid-phase potential of cathode (V)

Φ_2 liquid-phase potential of electrolyte (V)

Φ_f electrode potential of Li counter electrode (V)

Subscript

n active material type (NMC and LMO)

m particle size class

avg   average value

cat   cathode

eff   effective

sep   separator

sur   surface

test   test data

Chapter 1 Introduction

1.1 Challenges and Motivation

With the current rate of fossil fuel consumption, the world will face energy and environmental challenges in the middle of this century [1, 2]. Governments of the developed countries have been actively exploring alternative energy sources relying so far on increased renewable power and nuclear energy as the most feasible solution over the past decades. It is expected that other renewable energy sources such as wind, solar and hydropower, will gradually play more significant roles in global energy supply due to their environmentally-friendliness and sustainability. An effective way to use these intermittent power generation technologies is to store energy as electric power and to use the power in transportation applications. Hence, the storage and application of electric energy is a concern in the academia and industry.

Batteries have experienced a long-term development since Italian scientist Volta invented the first one in the 1800s. In 200 years of history, many different chemistries of batteries were developed. Figure 1.1 briefly describes several categories of batteries with a milestone meaning [3].
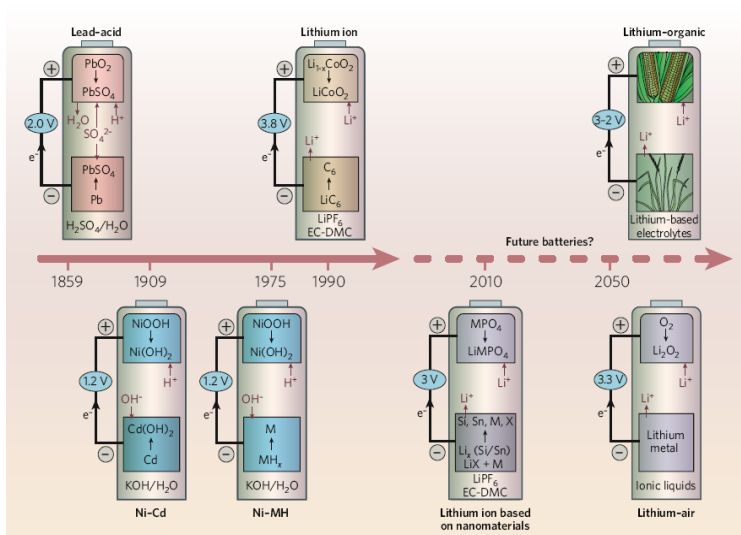
Figure 1.1: Changes in battery chemistry over the years [3].

Li-ion battery (LIB) is the one of products currently under nanotechnology development. Over the past two decades, the range of its application was broadened from the aerospace industry to people's daily life needs. Nowadays, high performance Li-ion batteries are of demand more than ever upon the emergence of new high technology applications such as electric and hybrid-electric vehicles. There are various factors that dictate the performance of Li-ion batteries including materials nanotechnology, composite electrode design and formulation and type of electrolyte. It is a complicated job for engineers to optimize all parameters and their correlations through experimental methods. Therefore, mathematical models coupled with experimental measurements, are required as valuable and effective tools for designing high-quality and long-life Li-ion battery cells. Moreover, such models can provide researchers and manufacturers with detailed theoretical understanding of the system of interest.

1.2 Objectives

The objective of this project is to investigate the energy and power capability and performance degradation of commercial mixed cathode Li-ion battery systems. Specific to this study is a 15Ah commercial electric vehicle/ hybrid electric vehicle (EV/HEV) battery under various operating conditions. Generally, various factors determine the cell performance including the type of active material, electrode and cell design (e.g. electrode compacted density, porosity, active material loading in electrode, and electrolyte match with other components and battery working conditions). The system of interest in this project consists of a blended cathode of Lithium manganese oxide ($LiMn_2O_4$ or LMO) and Lithium nickel manganese cobalt oxide ($LiNi_{1/3}Mn_{1/3}Co_{1/3}O_2$ or NMC) and a graphite anode designed for hybrid power and energy applications.

The goals pursued during this research project are:

1. Develop methodologies for the determination on the cathode composition and improve on the understanding of physical/chemical properties for blended-cathode batteries;

2. Devise a physics-based mathematical model to describe the electrochemical performance of the NMC-LMO blended cathode batteries. Particular affection is paid to measure important model parameters through independent experiments, such as electronic conductivity; and,

3. Based on the developed blended cathode model, some special experimental phenomena such as the synergistic interplay between LMO and NMC are illustrated in simulation analysis;

4. The final goal of this project is to study the calendar life of the blended cathode battery, a study span from coin cell to pouch cell level for the requirement of cooperation. The effect of various accelerated conditions such as temperature, storage SOC on the cell life-time will be studied and the degradation mechanism will be investigated.

As such this thesis will provide experimental and simulation tools for advancement of model based design of blended cathode Li-ion batteries.

1.3 Thesis Outline

This thesis consists of 7 chapters. In chapter 1, the motivation and objectives are presented. Next chapter (chapter 2) mainly reviews the electrochemical performance of two types of cathode active materials, namely, LMO and NMC in terms of structure and aging phenomena as well as mixing synergy. In chapter 3, a prediction technology to refine the composition of an unknown blended-cathode is developed, including experimental and simulation methods. Chapter 4 presents a multi-particle mathematical model to describe the electrochemical performance of the NMC-LMO blended cathode obtained from a commercial lithium-ion battery. Some significant parameters and expressions, such as the ionic diffusive flux and the effective electronic conductivity etc. are described and measured. Based on the model, an analysis of Galvanostatic Intermittent Titration Technology (GITT) for the commercial blended lithium-ion cathode is shown in chapter 5. A simulation charge-discharge behavior between different active materials and different size particles is qualitatively depicted for the NMC-LMO blended cathode. Chapter 6 shows the calendar life study for the commercial pouch cell in which the capacity loss mechanisms is analyzed and a pressure effect on the aged pouch cell is researched. Chapter 7

lastly summarizes the conclusions of the current work and introduces the recommendations for

the future research.

Chapter 2 Background and literature review

2.1 Lithium-Ion Technology

By comparing with several commercial secondary batteries, Li-ion battery displays its superiority in terms of energy and power density, electrochemical performance and working windows as Figure 2.1 and Table 2.1 show.
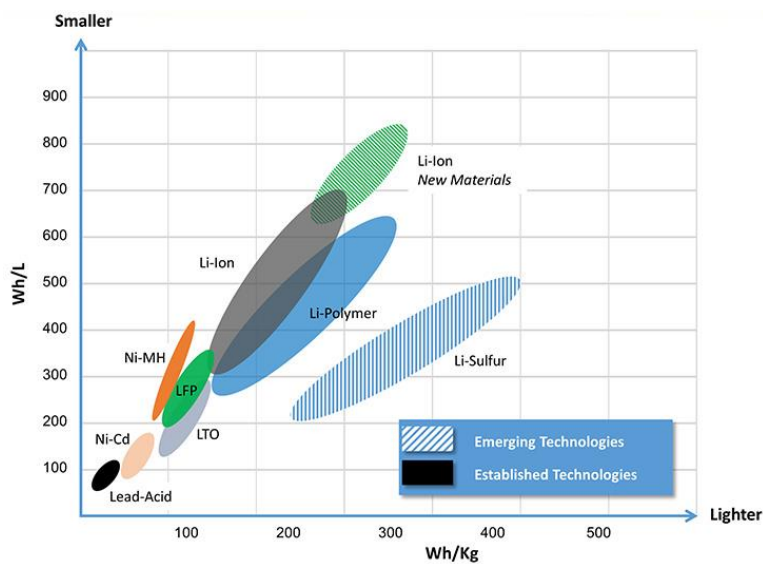
Figure 2.1: The energy density of different rechargeable batteries [4].

(a) High energy density: currently, the specific energy of commercial Li-ion batteries could reach 250 WhKg^{-1}/700 WhL^{-1}[4], which is much higher than that of nickel metal hybrid (NiMH) and Ni-Cd batteries. With the application of high energy density materials, such as Si composite material with a specific capacity of more than 2000mAhg^{-1}[5], the specific energy of Li-ion batteries will make a further improvement.

6

(b) High open circuit potential: the working voltage window is usually between 3.0V and 4.2V in Li-ion batteries. Therefore, average working voltage is about 3.6V which is three times higher than that of NiMH or Ni-Cd cells. Therefore, it is possible to make smaller and lighter batteries.

Table 2.1: The performance of different rechargeable batteries

Batteries category		Ni-Cd battery	Nickel Metal Hydride battery	Li-ion battery
Volume energy density (WhL^{-1})		~160	~200	~650
Mass energy density (WhKg^{-1})		~70	~80	~200
Average output voltage /V		1.2	1.2	3.6
Cycling life		~500	~500	~2000
	charge	0-45	0-45	0-45
Temperature range/℃	discharge	-20-65	-20-65	-20-60
	storage	-20-45	-20-45	-20-45
Month self-discharge rate /%		~15	~25	~2

(c) Long cycling life: the cell with LiFePO$_4$ cathode can cycle over 2000 times while the remaining capacity keeps above 80%.

(d) Low self-discharge rate: the self-discharge is below 2% per month under room temperature, which results from a good protection role of solid electrolyte interface (SEI) film on the surface of negative electrode.

(e) Environment-friendly: Li-ion batteries are low- pollution power supply systems.

In addition, Li-ion battery has no memory effect.

As a stable electrochemical system, Li-ion battery realizes the conversion between chemical energy and electric energy repeatedly during cell charging and discharging. Figure 2.2 shows the working principle of a Li-ion battery.
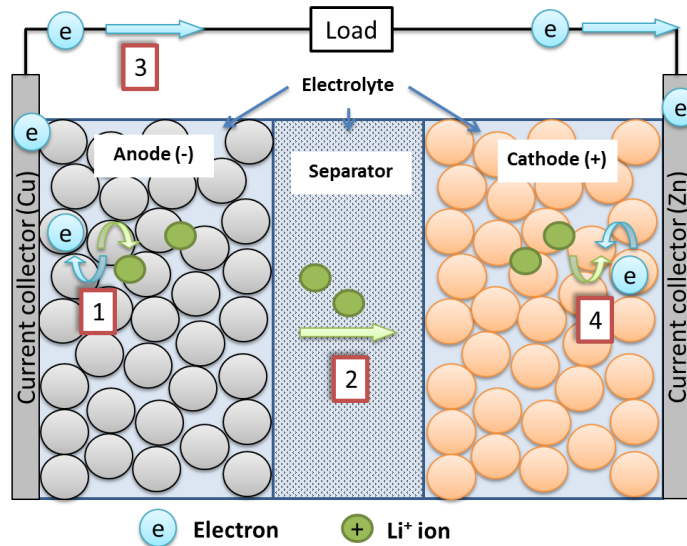
Figure 2.2: The working principle of a Li-ion battery [6].

A Li-ion battery includes two composite electrodes coated on metallic current collectors (i.e., aluminum foil for positive electrode and copper foil for negative electrode) and separated by an ion-conducting and electron-insulating separator [7]. The electrolyte plays a crucial role of conducting ions during cell operation. When discharging, lithium ions leave the negative electrode active material to the positive electrode through electrolyte, while the electrons flow from the negative to positive electrode by an external circuit. The negative electrode material is oxidized while the counterpart electrode is reduced during discharging. Opposite reactions occur while charging the cell. In a Li-ion battery, the active material is blended with other constituents, i.e., conductive agent and binding agent. So far, the main commercial anodes

consist of graphite with the theoretical capacity of 372 mAhg^{-1}. Though several high specific energy active materials were discovered several years ago, such as Si, Si-Sn, they have been researching in the lab due to some drawbacks like a huge volume difference between lithiated and delithiated states. Thanks to the breakthrough by Toshiba Corporation to overcome the technological bottleneck of gas-generation, lithium titanium oxide ($Li_4Ti_5O_{12}$) as a high safety performance anode material, can be used and commercialized today. Compared to the anode, many cathode materials can be chosen, ranging from lithium cobalt oxide ($LiCoO_2$) first used by Sony Corporation 1n 1991 [8] to lithium manganese oxide ($LiMn_2O_4$), lithium iron phosphate ($LiFePO_4$) and lithium nickel manganese cobalt oxide ($LiNi_{1/3}Mn_{1/3}Co_{1/3}O_2$). Recently, the blended-composite electrode made of $LiMn_2O_4$ (LMO) and $LiNi_{1/3}Mn_{1/3}Co_{1/3}O_2$ (NMC) as cathode has shown an excellent electrochemical performance. These two materials are mutually complement, mediating a new balance on the energy and power density, voltage plateau as well as cycling life, which is satisfied with the requirement of design and application. Due to the stability and durability of the blended cathode, this type of blended positive electrodes is being applied to Li-ion batteries for use in electric vehicle (EV) and hybrid electric vehicle (HEV). Taking a mixture of LMO and NMC as the cathode and graphite as the anode and for example, the electrochemical reactions read:

positive electrode oxidation reaction:

$$LiMn_2O_4 \leftrightarrow Li_{1-x}Mn_2O_4 + xLi^+ + xe^-,$$

$$LiNi_{1/3}Mn_{1/3}Co_{1/3}O_2 \leftrightarrow Li_{1-y}Ni_{1/3}Mn_{1/3}Co_{1/3}O_2 + yLi^+ + ye^-,$$
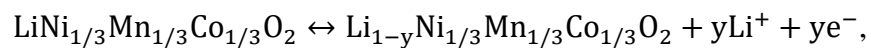
negative electrode reduction reaction:

$$6C + zLi^+ + ze^- \leftrightarrow Li_zC,$$
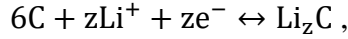
and the full-cell reaction:

$$LiMn_2O_4 + LiNi_{1/3}Mn_{1/3}Co_{1/3}O_2 + 6C \leftrightarrow Li_{1-x}Mn_2O_4 + Li_{1-y}Ni_{1/3}Mn_{1/3}Co_{1/3}O_2 + Li_zC.$$
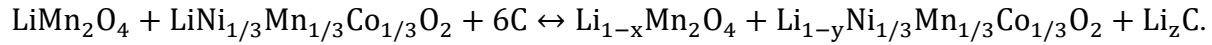
2.2 Lithium Manganese Oxide (LiMn$_2$O$_4$)

LiMn$_2$O$_4$ (LMO) is nowadays being used as one of cathode materials in commercial Li-ion batteries, thanks to its intrinsic advantages of low cost, abundance, safety and eco-friendliness. Its specific capacity is ca. 148mAhg^{-1} in theory while the practical one approaches ca. 110mAhg^{-1}. Currently, LMO-based batteries are mainly used for high power tools such as lawn mowers and electric drills. Nevertheless, two drawbacks are attributed to this material including a) Mn ion dissolution in electrolyte and thereafter a series of degradation effects, b) Jahn-Teller effect of Mn ions. They will give rise to serious aging phenomena during cycling and storage, resulting in an increase of impedance and capacity fade. Because of its excellent rate capability, researchers try to solve these shortcomings to obtain a good electrochemical performance.

2.2.1 The structure and electrochemical performance of LiMn$_2$O$_4$

The crystallographic structure of LMO spinel is shown in Figure 2.3.
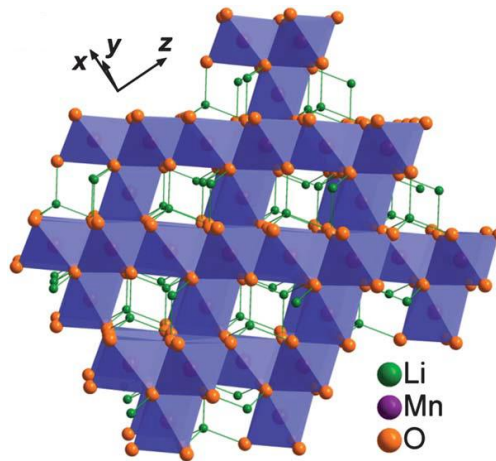
Figure 2.3: Crystal structure of LMO spinel shows Li Mn O ions arrangement and a 3-demensional channels for Li ions transport [9].

The Li and Mn ions occupy the tetrahedral and octahedral sites, respectively, constituted by oxygen ions. This structure provides three-dimensional pathways for Li ions to diffuse resulting in a high power capability. Table 2.2 lists the values of diffusion coefficients and electronic conductivities of the various commercial cathode materials in comparison with those of LMO.

In the spinel framework, ¾ of Mn ions reside in Mn ions layers; the rest of Mn is located in the adjacent Li ions layers. Therefore, during the process of Li deinsertion from the structure, there are sufficient Mn ions in every layer to supply a sufficiently high binding energy and maintain a stable oxygen array[39,40]. Spinel LMO was used as a cathode material for the first time in 1983[41]. Currently, 120mAhg^{-1}of practical capacity is achievable with a good retention upon further cycling. Various types of LMO have synthesized to improve its electrochemical performance and cycle life. Porous LMO nanorods with high crystallinity and phase purity were prepared by Jun Chen group [9].

11

Table 2.2: Diffusion coefficient and electronic conductivity of the commercial cathode materials.

Electrode Material	Diffusion Coefficient (cm^2s^{-1})	Technique	Electronic Conductivity (Scm^{-1})	Description
$LiMn_2O_4$	10^{-9} [10]	CV*	3×10^{-5} to 3×10^{-4} [17]	1.0% Cabon
	10^{-11} [12]	CV	3.2×10^{-5} [18]	
	5×10^{-10} [11] (Single crystal)	PSCA**		
	10^{-12} to 10^{-9}	PSCA		
	10^{-11} to 10^{-8} [13 -15] (thin-film)	EIS***		
	2.8×10^{-13} [16]	Model		
$LiNi_{1/3}Mn_{1/3}Co_{1/3}O_2$	10^{-12} to 10^{-10}[19]	Model	5.45×10^{-7} [20]	T=303K
	3.86×10^{-17} to 2.41×10^{-13}[21]	EIS		
$LiCoO_2$	10^{-10} to 10^{-8} [22-26]		5.6×10^{-4} to 20 [27-29]	
$LiFePO_4$	1×10^{-8} [30]		10^{-9} [36] to 10^{-7} [37 -38]	including intrinsic and apparent diffusion coefficient and electronic conductivity
	2.2×10^{-16} to 7.4×10^{-13} [31-35]			

*CV: cyclic voltammetry

**PSCA: potential step chronoamperometry

***EIS: Electrochemical impedance spectroscopy

The porous LMO nanorods exhibited superior electrochemical behavior (e.g., 127 mAhg^{-1} of attainable capacity and high capacity retention). Thanks to one-dimensional nanostructure providing fast Li ions and electronic intercalation/deintercalation kinetics, the nanomaterial shows excellent rate capability.

2.2.2 Aging mechanisms of LiMn$_2$O$_4$

Li-ion batteries suffer from various degradation mechanisms. The manifestations of aging phenomena are capacity fade, power reduction and impedance increase. This part will mainly review the sources of capacity fade and contributions of LMO material to battery aging processes.

2.2.2.1 Mn Dissolution into the electrolyte

In the early 1996, Seung et al. [42] studied the Mn dissolution in an LMO cathode. Comparing three LMO samples with different surface areas, they found that the sample with the smallest surface area shows the slowest aging rate upon cycling at 1 mAcm^{-2} between 3.6 and 4.3V vs. Li. According to further research, Mn dissolution was not significant at potentials below 4.1V, but it begins to dissolve fast above 4.1V. In addition, Experiments also demonstrated that Mn dissolution in PC/THF(Propylene carbonate/Tetrahydrofuran) or PC/DME(Propylene carbonate/2-dimethoxyethane) electrolyte aggravates with increasing carbon content loaded in cathodes because the solvent molecules are oxidized on carbon surfaces and a generated species can promote the Mn dissolution [43,44].

In a water-contaminated organic electrolyte, acids form from hydrolysis of $LiPF_6$ [45] inducing a disproportionation reaction as shown in Figure 2.4. Benedek et al. [47] obtained the free energy of Mn dissolution in acid using first principles calculations, which confirmed the role of disproportionation reaction in the Mn dissolution.

Disproportionation: $LiMn_2O_4 \rightarrow Li[Li_xMn_{2-x}]O_4 + Mn^{2+}$

Acid dissolution by HF: $Li_{1-x}Mn_2O_4 + HF \rightarrow \lambda - Mn_2O_4 + LiF + Mn^{2+} + H_2O$
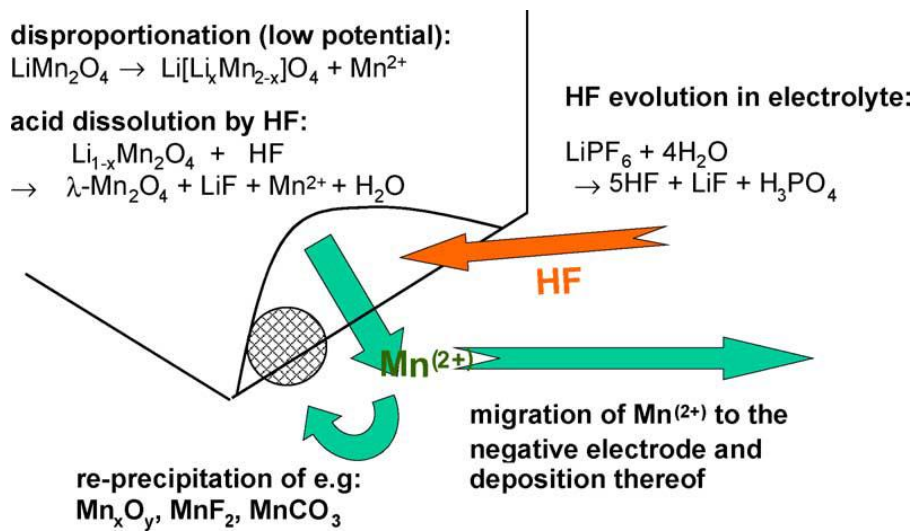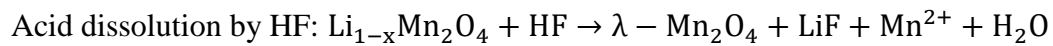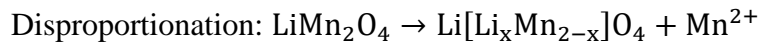
Figure 2.4: Dissolution of LMO spinel results from disproportionation and acid dissolution by HF formed by reaction between H_2O and $LiPF_6$, and dissolved Mn ions will migrate to negative electrode and deposit thereof [46].

About 1/3 of total capacity fade directly results from Mn dissolution [42, 48]. Mn dissolution has various consequences. First of all, Due to Mn dissolution, an inactive layer will form at the spinel/carbon interface which increases the contact resistance resulting in a capacity loss because of additional polarization [42]. In addition, further studies [49] show that Mn ions dissolved from

14

the LMO cathode migrate to the negative electrode and are reduced on the lithiated graphite

electrode surface, causing a high increase in the charge-transfer impedance at the interface

between graphite and electrolyte, which can deteriorate cell performance. Thirdly, Mn

dissolution in LMO/Graphite cells could result in a coulombic imbalance in a cell [50]. Figure

2.5 is a schematic diagram about the coulombic imbalance. During charging, 1 Mn^{2+} ion

accompanies 8 Li^+ migrating from the cathode to the anode where the 10 coming electrons

reduce the cations. During discharging, the 8 Li^+ travels back to the cathode and Manganese

deposits on the surface of the graphite particles in the anode. Therefore, only 8 electrons rather

than 10 electrons are passed through the external circuit during discharging. In brief, not all the

energy stored in the battery during charging is recovered when discharging the cell.
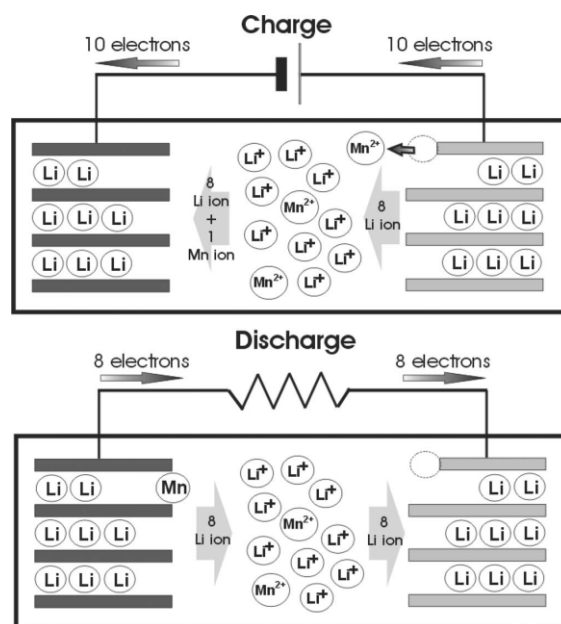
Figure 2.5: A schematic diagram of the coulombic imbalance caused by Mn dissolution in

LMO/Li cells. A difference of two charges between charging and discharging displays a loss

capacity due to one Mn ion deposits in the graphite [50].

15

Mn dissolution and its subsequent effects are considered as the predominant cause for capacity

fade of LMO. Physical properties of LMO (especially surface area), type of electrolyte and

carbon content are important factors for Mn dissolution. SubstitutingLiPF$_6$ with another

electrolyte salt such as LiBoB (Lithium bis(oxalate)borate) could reduce Mn dissolution and

lower the rate of capacity fade as shown in Figure 2.6 [46].
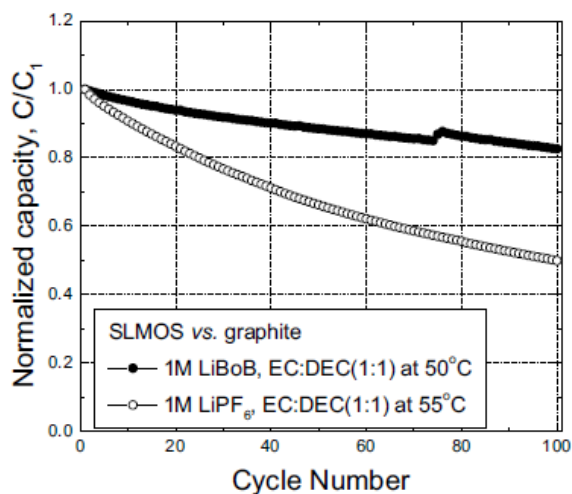
Figure 2.6: A cycling capacity comparison using 1M LiBoB/ EC:DEC (1:1) and 1M

LiPF$_6$/EC:DEC (1:1) electrolytes. C$_1$ is the initial discharge capacity and defined as 1.0 [46].

2.2.2.2 Jahn-Teller distortion

In the electronically degenerate state, the orbitals are thought to be asymmetrically occupied and

get more energy. In order to get rid of this extra energy, the system tries to lower the overall

symmetry of the molecule by undergoing distortion, which is otherwise known as Jahn-Teller

effect [51]. Usually, it is observed in high spin d^4, low spin d^7 and d^9 electron configuration in

the octahedral environment. Therefore, due to Mn^{3+} electron configuration and occupation

16

position in LMO, it tends to happen Jahn-Teller distortion. As Figure 2.7 shows, $Li_xMn_2O_4$ causes a step-wise change in electrode potential to reach a flat potential equal to 3.0V vs. Li. [52-54].
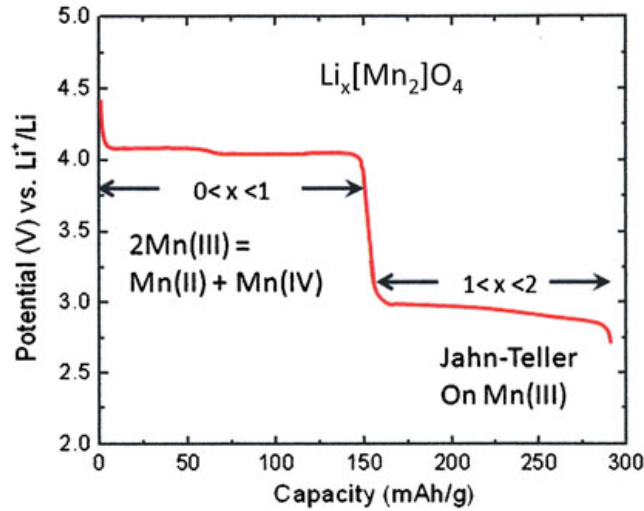
Figure 2.7: Potential profile LMO and John-Teller effect.

2.3 Lithium Nickel Manganese Cobalt Oxide ($LiNi_{1/3}Mn_{1/3}Co_{1/3}O_2$)

Due to the drawbacks of layered cathode materials (e.g., high cost, low safety and stability) and the difficulty of synthesizing and instability (e.g., $LiNiO_2$), a great deal of work to optimize the layered oxide has been conducted. Dahn et al. [55] have synthesized a set of $Li[Ni_xCo_{1-2x}Mn_x]O_2$ compounds with $0 \leq x \leq 1/2$. Their materials showed good specific capacities from 110 mAhg^{-1} to 130mAhg^{-1} between 3.0V and 4.2V vs. Li and had a very little capacity loss. Ohzuku and Makimura [56] have reported $LiNi_{1/3}Mn_{1/3}Co_{1/3}O_2$ with the capacity of 150mAhg^{-1} over a potential range from 2.5V to 4.2V vs. Li. Combining computational and experimental studies, Ceder and his co-workers [57] clarify the valence states in $LiNi_{1/3}Mn_{1/3}Co_{1/3}O_2$; the results

17

indicate the material can provide a high capacity and excellent capacity retention due to its stable crystallographic structure.

2.3.1 The Structure and electrochemical performance of LiNi$_{1/3}$Mn$_{1/3}$Co$_{1/3}$O$_2$

LiNi$_{1/3}$Mn$_{1/3}$Co$_{1/3}$O$_2$ (NMC) has a layered α-NaFeO$_2$ type structure. In this framework, the oxygen atoms stack in ABCABC arrangement and slabs of CoO$_2$, NiO$_2$ and MnO$_2$ were proposed by Koyama et al. [58] to alternatingly occupy the space between oxygen layers, as shown in Figure 2.8. Such a layered structure provides a high Lithium ion diffusion coefficient (refer to Table 2.2) leading to a high rate capability.
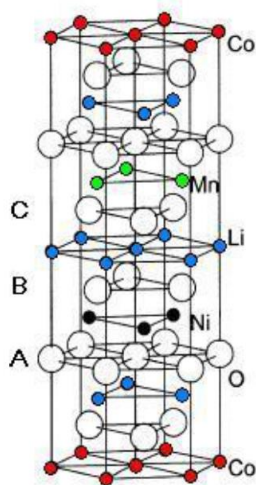
Figure 2.8: Structural models of NMC [57, 58].

For the valence states in NMC, electron configurations of Nickel, Cobalt and Manganese with their oxidation states are displayed as Ni^{2+}: t$_{2g}^6$e$_g^2$, Co^{3+}: t$_{2g}^6$, Mn^{4+}: t$_{2g}^3$, respectively in Ref. [55, 57]. As seen in Figure 2.9, for Li content between 2/3 and 1 the redox reaction is Ni^{2+}/Ni^{3+} ,

18

for Li content between 1/3 and 2/3 the reaction is Ni^{3+}/Ni^{4+}, and for Li stoichiometry between 0

and 1/3 the reaction is Co^{3+}/Co^{4+}. For the Mn^{4+}, there is no valence change or redox reaction

during charging and discharging, whose function is to provide a stable fundamental structure for

NMC.
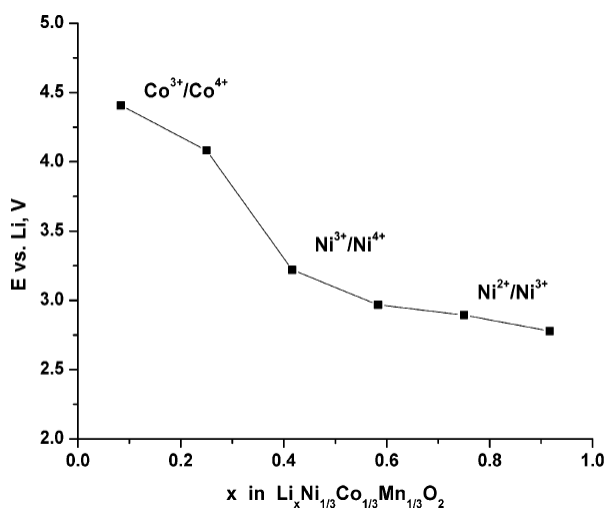
Figure 2.9: Calculated average voltage points in NMC [57].

2.3.2 Aging mechanisms in $LiNi_{1/3}Mn_{1/3}Co_{1/3}O_2$

Studies of the chemical and structural stability of NMC cathode under different cutoff charge

voltage show that NMC becomes unstable at 4.6V and higher. By chemically delithiating NMC,

Manthiram et al. [59] investigated the oxidation state of group $Ni_{1/3}Mn_{1/3}Co_{1/3}$ and the oxygen

content in $Li_{1-x}Ni_{1/3}Mn_{1/3}Co_{1/3}O_2$ with lithium content (Figure 2.10a) and found that the

oxidation state increases to about +3.6 with decreasing lithium content from 1.0 to 0.35, and

then, it begins to decrease. Meanwhile, oxygen loss occurs for lithium content between 0 and

0.35. Based on the above mentioned study, an energy diagram of $Li_{0.35}Ni_{1/3}Mn_{1/3}Co_{1/3}O_2$ was

proposed, shown in Figure 2.10b. The energy band of $Ni^{3+/4+}$ redox couple has a slight overlap with that of O^{2-}, while there is a much larger overlap of $Co^{3+/4+}$ energy band with O^{2-} 2p band. Hence, the positions of $Ni^{3+/4+}$ e_g, $Co^{3+/4+}$ t_{2g} and O^{2-} 2p bands result in a bulk oxygen loss, which leads to structural instability of NMC during lithium contents $1-x<0.35$ (Voltage >4.6V).
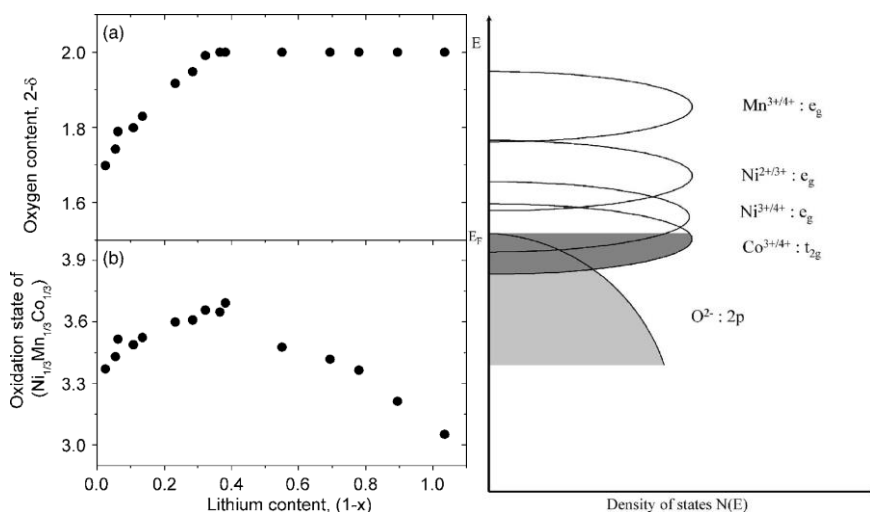
Figure 2.10: Variations of (a) oxygen content and (b) the average oxidation stage of $(Ni_{1/3}Mn_{1/3}Co_{1/3})$ with lithium content and Energy diagram for $Li_{0.35}Ni_{1/3}Mn_{1/3}Co_{1/3}O_2$ [59].

Zeng [60] observed a so-called "zigzag layer" on the surface of NMC particles by transmission electron microscopy (TEM) for the NMC cathode specific-capacity-degraded to 85% after 300 cycles between 2.75V and 4.2V at 1 C. As shown in Figure 2.11, the zigzag layer includes three layers marked as BU, NS and SE from interior to the surface of the active material particle. Elements Ni, Mn and O all suffer a loss in the whole zigzag layer and it is serious in the SE area where the weaker spots disappeared as seen in TEM image (Figure 2.12).
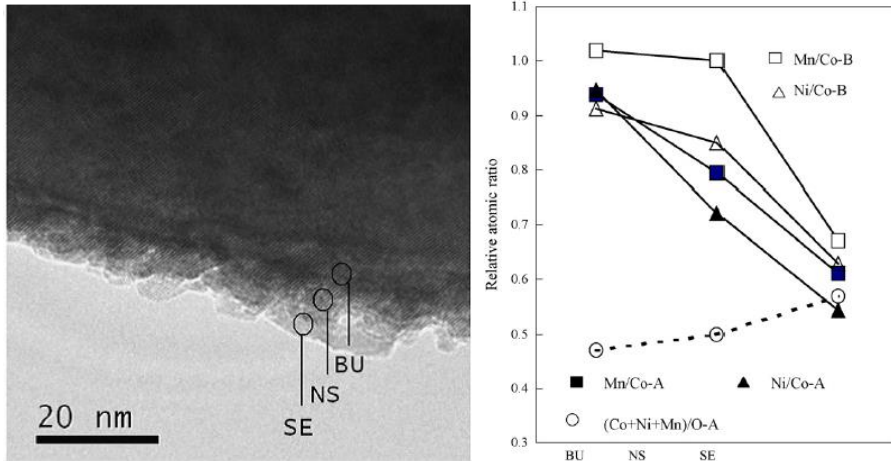
Figure 2.11: The three location (marked as BU NS and SE) in the zigzag layer and the charge of Mn/Co, Ni/Co and (Co+Ni+Mn)/O in the zigzag; A and B represent two selected research regions for the same sample [60].

The capacity loss in NMC is mainly from structural damage on the surface of its particles, which may lead to the blockage of the Li channels thus decreasing the rate capability of the material.
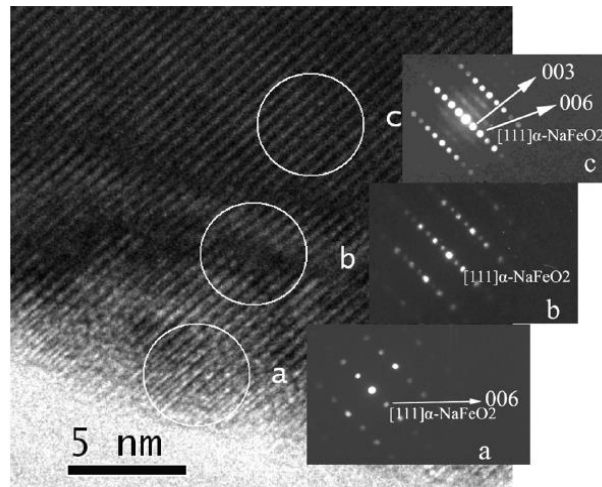
Figure 2.12: TEM images for the zigzag layer, spots a, b and c are located in SE NS BU areas, respectively; the intensity of diffraction points becomes gradually weak from spot c to a [60].

21

2.4 The Blended Cathode of LiMn$_2$O$_4$ and LiNi$_{1/3}$Mn$_{1/3}$Co$_{1/3}$O$_2$

LMO spinel cathode has a high voltage plateau but suffers from low discharge capacity, poor

cycle life, and small capacity retention after a long-term storage at elevated temperatures, while

NMC has a high capacity, high capacity retention, and good thermal stability. Therefore, by

considering a mixture of NMC and LMO as an active cathode material may yield in an optimized

electrochemical performance. Indeed, by blending the two materials, a balance characteristic in

terms of capacity density and voltage plateau was obtained (Figure 2.13) and a synergy effect

was discovered. The effect can make NMC suppress Mn dissolution so that the blended cathode

displayed an enhanced cycling durability and an improved high-temperature storage

performance.
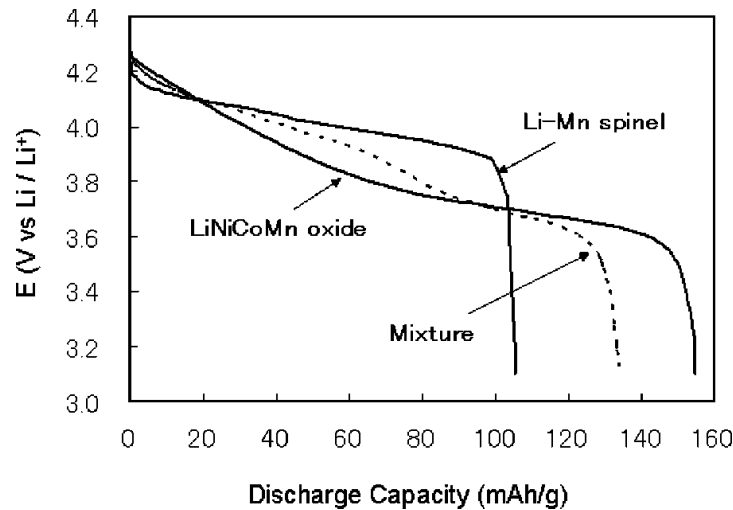
Figure 2.13: Initial discharge curves of some positive materials [61].

22

2.4.1 Synergy effect

Synergic effects in blended LMO and NMC electrodes have currently been proposed by Dahn and co-workers [50]. They blended LMO and NMC together by weight ratios of 100%:0%, 75%: 25%, 50%:50%, 25%:75% and 0%:100%. The blended-material cathodes were then cycled at C/10 between 3.0V and 4.3V at 30°C, 40°C, 50°C and 60°C. As Figure 2.14 shows, the cycling stability decreases with temperature increase. For an adding of small ratio LMO such as less than 50% in a blended cathode has a little reduce in capacity retention.
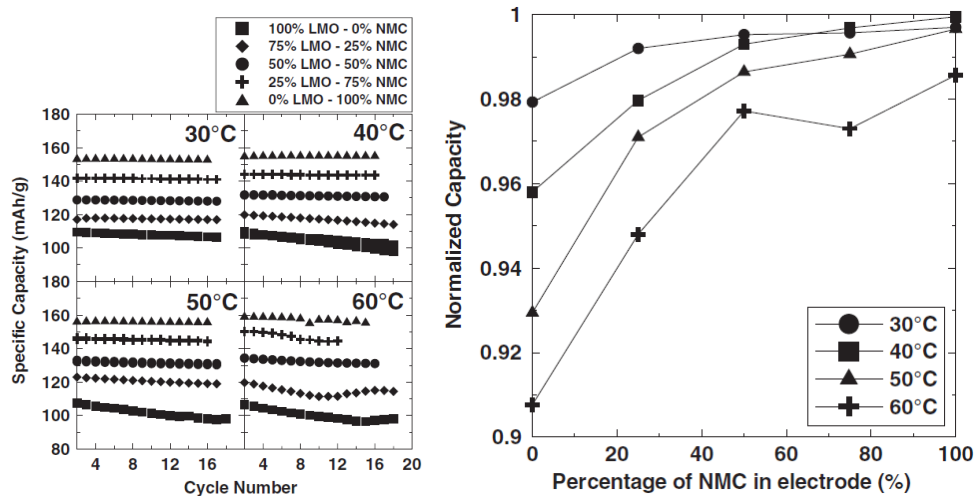
Figure 2.14: Cycling performance at various ratios of LMO and NMC, and the correlation between percentage of NMC in electrode and capacity retention after 14 cycles under different temperatures [50].

In the capacity/voltage (dQ/dV) differential analysis shown in Figure 2.15, the two peaks at ~4.00V and ~4.15V correspond to LMO and the one at ~3.75V corresponds to NMC. The

intensity of peaks qualitatively demonstrates the amount of materials in the mixture. The capacity loss of the blended cathode mainly results from LMO degradation after certain numbers of cycles. The change in terms of the height of LMO characteristic peaks at ~4.00V and ~4.15V decreases with an increase in the ratio of NMC in the electrode, which displays that NMC stabilizes LMO to some extent during cycling. This is the synergy effect that NMC helps to suppress Mn dissolution in a blended cathode.
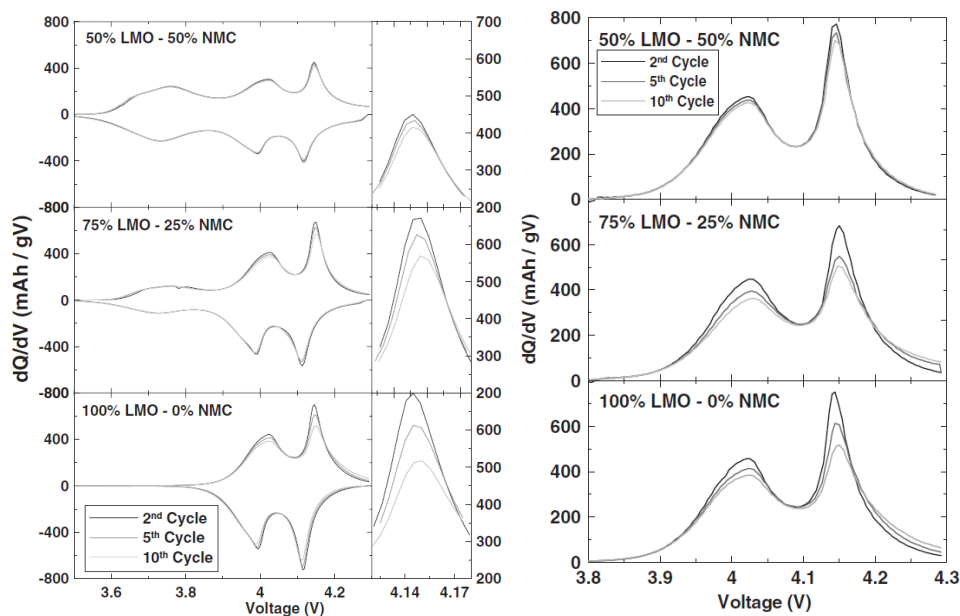
Figure 2.15: Capacity/Voltage (dQ/dV) vs. Voltage (V) of the three most LMO-rich electrodes cycled at 50°C [50].

The studies above for the synergy effect simultaneously involve the response of the blended-electrode for cycling and high-temperature. The same conclusions can be obtained by individual research, i.e. cycling stability and high-temperature storage. Nahm et al.[62] have prepared four types of blended LMO-NMC samples, as listed in Table 2.3.

Table 2.3: Samples and classification used to study cycling capability of blended LMO-NMC electrodes in Ref.[62]

Sample	Class
Sa1	LMO
Sa2	$Li/Li[Li_{1/15}Ni_{1/3}Co_{2/5} Mn_{1/3}]O_2$
Sa3	Sa1:Sa2=1:1 by simple mixing
Sa4	Sa1:Sa2=1:1 by Ball milling and calcinations at 800°C

After 50 cycles between 2.5-4.5V, the samples Sa3 and Sa4 keep high capacity retention (Figure 2.16). They concluded that $Li[Li_{1/15}Ni_{1/5}Co_{2/5}Mn_{1/3}]O_2$ enhances the cycling stability of LMO and slows down the degradation rate. Contrary to the case of ball-milled sample, simple mixing can avoid structural damages in both components which guarantee high capacity efficiency in the whole cycling test.
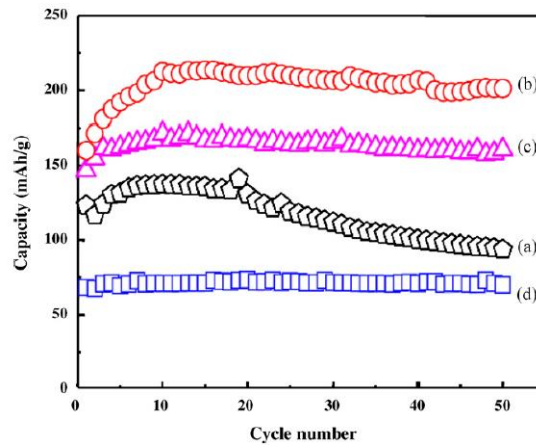
Figure 2.16: Cycling durability for the samples in Table 3 (a) Sa1, (b) Sa2, (c) Sa3 and (d) Sa4 [62].

Takeda and co-workers [61] have investigated storage performance under elevated temperature for the blended cathode of $Li_{1.1}Mn_{1.9}O_4$ and $LiNi_{0.4}Co_{0.3}Mn_{0.3}O_2$ (6:4 by weight ratio). As shown

in Figure 2.17, after 30 days of storage at 45°C, the blended cathode showed a higher capacity recovery ratio than both single active material electrodes.
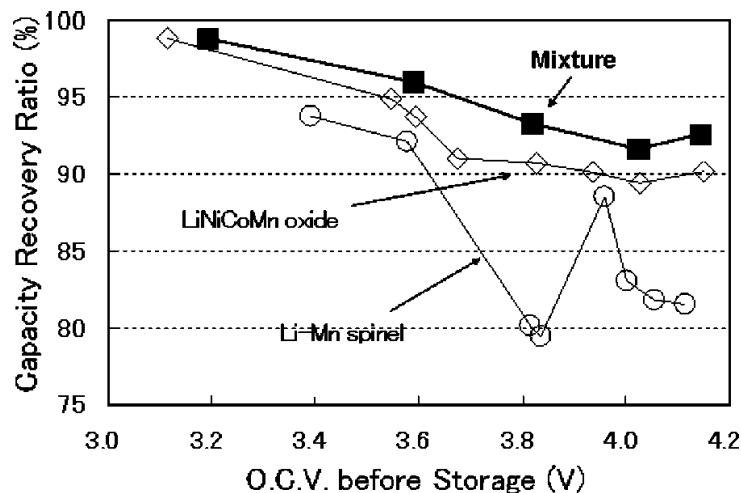
Figure 2.17: Capacity recovery ratio of Li-Mn spinel, NMC and a mixture of these two cathode active materials according to Ref. [61].

The synergy effect in the LMO-NMC electrode can improve the capacity retention of LMO after cycling and storage, especially a distinct enhancement under a high temperature. Takeda [61] tried to study the mechanism behind by analyzing the changes in lattice parameters of single and blended active materials upon storage, but it is still no a clear conclusion.

2.4.2 A refinement of active material ratio in a blended cathode

A method has been recently proposed by Kobayashi et al. to estimate the contribution of each active material to the total capacity of a blended cathode [63] of NMC: $LiAl_{0.1}Mn_{1.9}O_4$ =3:7 (abbreviated as NML37) by weight ratio.

26
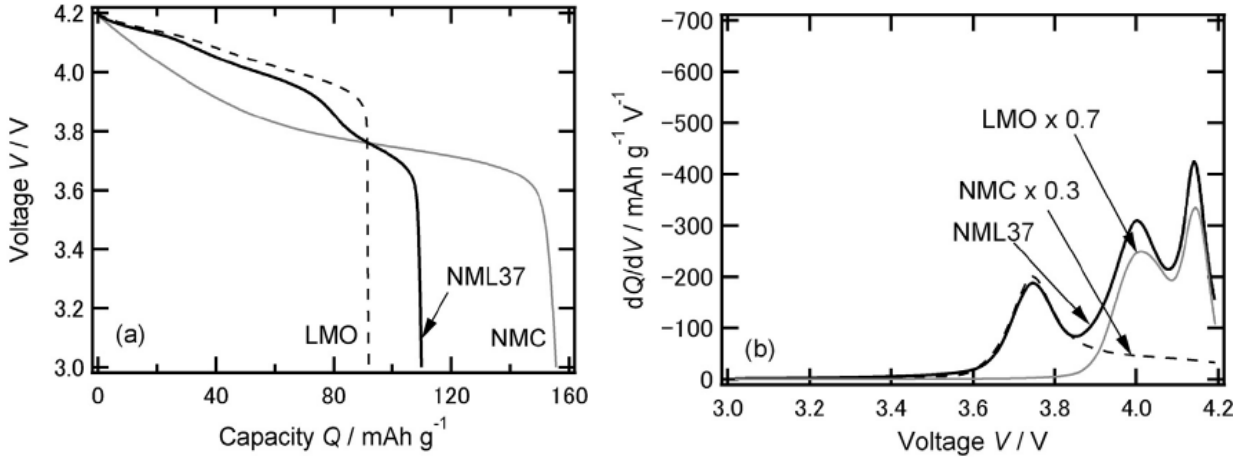
Figure 2.18: Discharge curves for LMO, NMC and mixture, and dQ/dV analysis curves [63].

Figure 2.18 shows a comparison of the discharge capacities and the dQ/dV curves of single and blended materials cathode. Both peaks at~4.0V and ~4.14V are the signatures of LMO, showing the reaction rang of LMO between 3.85V and 4.2V; while the peak at ~3.75V represents NMC. The fact that NMC peak reinforces the intensity of two LMO peaks indicates the contribution of NMC for the all capacity will remain during the whole process.

Using the deconvoluted dQ/dV curve, the capacities of the blended cathode (NML37) were separated into the capacities of two unitary active material cathodes (NMC and LMO), which had a good agreement with the experiment data (Figure 2.19). In addition, the method could also be applied for capacity analysis of the degraded blended cathode.
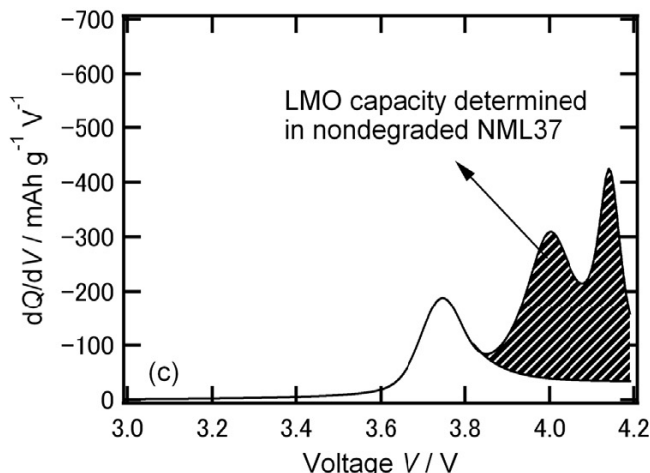
Figure 2.19: The deconvoluted dQ/dV curve corresponding to the blended LMO/NMC electrode Studied in Ref. [63].

2.5 Graphite and Aging

Currently, graphite is the most popular anode active material in commercial Li-ion cells. Graphite electrode significantly contributes to capacity fade in a Li-ion battery. Lithiated graphite has a high chemical or electrochemical activity. When the battery is opened under high state of charge (SOC) the graphite electrode has a color of golden yellow. But when exposed to air for a few seconds, the electrode becomes black, which means lithiated graphite is chemically oxygenized, and when exposed to water, a strong spontaneous reaction might happen. In a sealed anaerobic system such as a commercial cell, such unstable lithiated graphite reacts with salt and organic solvent, e.g., $LiPF_6$ and dimethyl carbonate (DMC), in the electrolyte and forms the so-called "solid-electrolyte interphase" (SEI) film on the surface of active particles [64].

SEI film generally forms during the first charge of the battery. Regularly, SEI film consists of two layers with different compositions. One layer is inorganic compounds, such as Li_2CO_3, LiF,

Li_2O, of about 2nm thick, deposited on the inner of SEI. The outer layer is made of organic species, such as $(CH_2OCO_2Li)_2$ and ROLi, $ROCO_2Li$, (R is an organic group) [65,66]. The composition of SEI changes mainly with the type of electrolyte and the operating condition. The positive function of SEI is to prevent direct contact between active graphite and electrolyte to reduce the side reactions. On the other hand, SEI layer increases the transfer impedance and causes the power of the battery to degrade.

Many studies proposed that the aging of a Li-ion battery mainly stems from parasitic reactions on the surface of anode particles. There are several mechanisms to describe the capacity fade related to the graphite electrode. Firstly, during cycling and storage of battery, the thickness of SEI film gradually increases while cyclable Li ions are consumed. Secondly, Lithium ions and electrons may bond to form metallic lithium on the surface of the anode electrode if the cell is overcharged or charged at low temperatures and high rates. Table 2.4 shows the situation of Lithium plating on the surface of graphite anode after fully charging cell at different temperatures. A poor cell design or production process also can result in lithium plating to occur more likely under harsh operating conditions. The lithium metal on the surface continually reacts with the electrolyte, causing electrolyte deficiency even drying of the cell. Finally, solvent or contaminating species may co-intercalate into the graphite particles leading to graphite exfoliation, thus loss of active material [67].

Table 2.4: The situation of Lithium plating for cell charged up to 4.2V (set value) at 3A [68].

Charge Temp.(°C)	Voltage (mV)	IR (mOhm)	Picture	Li plating
0	4086	17.8		No
-5	4073	18.1		No
-10	4055	18.4		Little
-15	4036	18.8		Yes
-20	4005	19.4		Yes

Overall, the instability of lithiated graphite anode could cause safety issues and degradation of Li-ion battery. The application of other active materials, such as lithium titanium oxide ($Li_4Ti_5O_{12}$), could improve the safety preformation of the whole cell. However, the difficulties of new materials themselves and compatibility with other components need to be overcome.

Chapter 3 Composition prediction for the blended cathode

The following section is based on previously published work 'Model-Based Prediction of Composition of an Unknown Blended Lithium-Ion Battery Cathode, *J. Electrochem. Soc.,* 162(4), A716(2015)' by Z. Mao et al. and is reproduced by permission from *Journal of The Electrochemical Society*. This thesis author specific contribution to this paper was to: develop the model, conduct the simulations and experiments, prepare all the graphics and results, and prepare the final manuscript and reviewer edits with direction from the project supervisors who were M. Fowler, Z. Chen and M. Pritzker. M. Safari and M. Farkhondeh offered advice on the modelling and experiments.

3.1 Introduction

Lithium-ion batteries (LIBs) are promising devices for portable storage of energy. The high volumetric and gravimetric energy densities of these batteries have enabled them to surpass other alternatives such as Ni-Cd and Ni-MH batteries for applications such as cellular phones and lap-top computers. However, LIBs have still not achieved significant penetration into the automotive industry due to challenges associated with their safety, service life and cost [69]. This has led to considerable research interest both from chemists and engineers to improve the formulation of cell components and develop tools for design, performance assessment and durability improvement of the cell. Promising results regarding the overall improvement of electrode performance have been reported when the cathode is made up of a blend of oxides. Physical mixtures of layered oxides such as $LiNi_xMn_yCo_{1-x-y}O_2$ (NMC) or $LiNi_xCo_yAl_{1-x-y}O_2$ (NCA) with

spinel $LiMn_2O_4$ (LMO) are good examples where the electrode performance benefits from a synergy between the individual components [70-73]. Not surprisingly, this has led to the increasing popularity of using blended cathodes in LIBs [74].

Due to the complex nature of the phenomena associated with the operation of LIBs, their design and performance are best optimized and analyzed with the aid of mathematical models [75]. Such models have been developed for a broad range of purposes, from the estimation of kinetic and transport properties of the active material to the prediction of battery service life [76-78]. Few mathematical models have been reported in the literature which simulate the electrochemical behavior of known blended electrodes [63, 73, 79-80]. An open-circuit voltage model or "OCV model" has been used to estimate the mass ratios of two well-characterized insertion compounds, mainly $LiNi_{0.8}Co_{0.15}Al_{0.05}O_2$ and $LiMn_2O_4$ in Ref. [81], $LiNi_{1/3}Mn_{1/3}Co_{1/3}O_2$ and $LiAl_{0.1}Mn_{1.9}O_4$ in Ref. [63] and $LiNi_{1/3}Mn_{1/3}Co_{1/3}O_2$ and $LiMn_2O_4$ in Ref. [79]. In such models, the blended cathode composition is estimated from differential-capacity curves obtained from low-rate galvanostatic data (i.e., quasi-equilibrium condition). In this approach, the capacity of the blended electrode (i.e., inverse of the quasi-equilibrium curve as a function of capacity) is related to those of the individual active compounds as a function of potential through a summation weighted linearly according to their mass ratios. In studies where it was used to predict the composition of blended cathodes with known composition, its estimation error was found to be approximately 6% [63, 81]. Furthermore, this procedure becomes more difficult and less accurate when the identity of the active compounds is not well known. The need to quantitatively assess the performance of LIBs with unknown electrode

formulations is becoming ever more important given the increasing popularity of introducing batteries with blended cathodes into the commercial market.

In this chapter, a systematic procedure is followed to determine the composition of an unknown blended electrode with an acceptable accuracy less than ~1% error that is validated with ex-situ measurements. The cathode morphology and its elemental composition are first characterized using scanning electron microscopy (SEM) and energy-dispersive X-ray (EDX) analyses, respectively. The electrochemically-active components of the cathode are then identified by analysis of experimental electrode galvanostatic discharge data obtained at a very low current. In the next step, a physics-based model of the blended cathode is fitted to the galvanostatic lithiation curve to estimate the electrode composition. Finally, the prediction of the proposed model-based method is validated against a calibration curve obtained by independent and purely experimental X-ray diffraction (XRD) measurements. Accordingly, the cathode composition is determined in a non-destructive way once the component oxides are identified. It is important to emphasize that the objective of the model used in this procedure is not to describe lithiation and delithiation of the cathode under all conditions. Instead, this model is intended only to estimate the composition of the blended cathode. By choosing to apply this method to discharge data obtained at very low current, a relatively simple model can be used since porous electrode effects can be neglected. Although this procedure is demonstrated on discharge data, it could equally well be applied to a blended cathode during charging.

3.2 Single Particle Model

A simple physics-based model is used to simulate the galvanostatic discharge of the unknown blended cathode Li-ion cell under low current. As noted in the Introduction, porous electrode effects are neglected since the model is being applied to data obtained at low C-rates. Such an assumption has been shown previously to be acceptable for low C-rate conditions up to 1C in typical electrode designs [34-35, 82-83]. According to this assumption, the active particles are connected to a uniform sink or source of electrons (i.e. a conductive matrix) and Li^+ ions in the electrolyte. The blended cathode is assumed to be made of a physical mixture of N total types of active materials. Each type n of the active materials is present as a spherical particle with radius R_n within which Li diffuses, as described in Eqns. 3.1-3.3 below:

$$\frac{\partial c_n}{\partial t} = \frac{1}{r^2}\frac{\partial}{\partial r}\left(D_n r^2 \frac{\partial c_n}{\partial r}\right), \tag{3.1}$$

$$\frac{\partial c_n}{\partial r}\Big|_{r=0} = 0, \tag{3.2}$$

$$\frac{\partial c_n}{\partial r}\Big|_{r=R_n} = -\frac{i_n}{FD_n}, \tag{3.3}$$

where c_n and D_n are the concentration and diffusion coefficient, respectively, of lithium within the active particles of type n. i_n is the current density over the active surface area of the particles of type n and is related to the electric potential Φ of the cathode according to the following form of the Butler-Volmer equation:

$$i_n = Fk_n\sqrt{c_e}\sqrt{c_n^{max}-c_n^s}\sqrt{c_n^s}\left\{\exp\left(\frac{0.5F}{RT}(\Phi-U_n)\right)-\exp\left(-\frac{0.5F}{RT}(\Phi-U_n)\right)\right\}, \tag{3.4}$$

where U_n is the equilibrium potential evaluated according to the lithium concentration c_n^s at the particles surfaces, c_n^{max} is the maximum lithium concentration and k_n is the rate constant for the charge-transfer reaction at the surface of the nth particle type. Finally, c_e, T, F and R are the electrolyte concentration, temperature, Faraday constant and gas constant, respectively. It should be noted that the overpotential at the Li electrode is neglected under the condition of the very low currents used in our simulations and, thus, Φ corresponds to the cell potential vs. Li reference electrode.

The total current I_t is distributed over all the N types of particles as follows:

$$3M_t \sum_{n=1}^{N} \frac{\varepsilon_n i_n}{\rho_n R_n} = I_t, \tag{3.5}$$

where ρ_n is the density of the nth type of particles and ε_n is the mass fraction of the nth type of particles with respect to the total mass M_t of active material in the electrode and is subject to the condition:

$$\sum_{n=1}^{N} \varepsilon_n = 1 \tag{3.6}$$

The overall capacity Q of the blended electrode is related to the capacity q_n of the nth type of particles and their mass fractions in the electrode as follows:

$$M_t \sum_{n=1}^{N} \varepsilon_n q_n = Q \tag{3.7}$$

In this expression, q_n is the practical mass-specific capacity of the nth type of active compound, which generally is an empirical value depending on the material synthesis method and the

operating voltage range. It is obtained from the literature in accordance with a voltage range of 3V to 4.2 V and is listed in Table 3.2.

The governing equations were solved using the COMSOL Multiphysics 4.2 simulation package with a particle domain (i.e., one-dimensional) discretized into 20 equal intervals in the radial direction. The same formulation presented here can be used without any modification for the simulation of the dynamic behavior of the cell under low to medium applied currents. In this case, the solid-state diffusion and the surface resistance due to charge transfer will contribute to the capacity and potential loss of the electrode. If ionic and electronic transport effects at the electrode scale are explicitly included, the assumption of negligible porous electrode effects is relaxed and the resulting pseudo-2D model [84] can be used to simulate the discharge behavior at high rates. However, as noted previously, this is not required to estimate the blended cathode composition according to the procedure described in the following sections.

3.3 Results and Discussions

3.3.1 Surface morphology and elemental composition
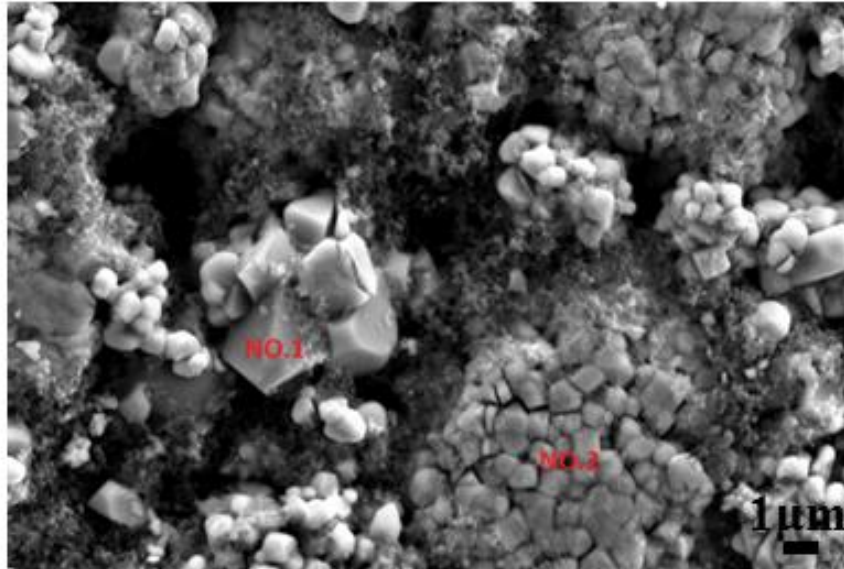
Figure 3.1: SEM image of the unknown cathode surface. EDX analysis was conducted on the two groups of particles labeled NO.1 and NO.2 above.

The surface of the unknown cathode was examined by SEM and EDX. Figure 3.1 shows an SEM image of a portion of the electrode surface showing the presence of two different types of particle agglomerates/clusters within the electrode. The first group (denoted as NO.1) is made of a few particles with dimensions ranging from 1-2 μm whereas the second group (denoted as NO.2) is composed of many particles smaller than 1 μm. The particle size distributions for both particle groups obtained from SEM image analysis are found to obey log-normal distribution functions yielding a d_{50} of 1.74 μm for group NO.1 and 0.87 μm for group NO.2. The results of

the elemental analysis of these two particle groups are summarized in Table 3.1. O, Mn, Co and Ni are found to be present in both groups. Not surprisingly, O is a dominant element in both groups. Among the metals, Mn is the major element in group NO.1, while the composition is more evenly split among Mn, Ni and Co in group NO.2. This preliminary analysis suggests that the active materials in the electrode are composed of two types of metal oxides: the first type is likely a Mn-oxide (i.e. LMO), while the second one is likely a blended-oxide with nearly equal atomic fractions of Ni and Co (i.e. NMC, the excess Mn may be due to LMO).

Table 3.1: EDX analysis of elemental composition of the unknown cathode corresponding to zones NO.1 and NO.2 in Figure 3.1.

		O	Co	Ni	Mn
atomic %	group NO.1	61.12	0.15	0.28	26.05
	group NO.2	58.25	6.53	5.98	9.34

3.3.2 Active material components

The discharge profile of the unknown-cathode/Li cell at a current corresponding to C/25 is presented in Figure 3.2a. The discharge capacity of this cell is found to be approximately $Q_{C/25} = 2$ mAh. The discharge profile is presented in terms of the normalized capacity Q_{norm} (i.e., with respect to the end-of-discharge capacity) defined as:

$$Q_{\mathrm{norm}} = \frac{Q}{Q_{C/25}} \tag{3.8}$$

This enables the intrinsic electrochemical signature of the electrode to be more easily compared to those of known individual active materials reported in the literature. The differential capacity is a property that can effectively delineate the subtle electrochemical changes of the electrode over the course of lithiation/delithiation. Accordingly, plots of differential capacity versus electrode potential provide rich information about the active materials in a given electrode [85]. Typically, at least one peak appears in these plots for the active materials used in LIBs. The potentials at which peaks appear are unique for a given active material and so potentially can be used to identify the components of a blended electrode [63, 81]. Figure 3.2b presents the differential capacity plot of the unknown cathode that has been determined from the electrode discharge data obtained at C/25 and shown in Figure 3.2a. Three distinct peaks at 3.743, 4.005 and 4.136 V appear in the plot. Based on the SEM/EDX results in the previous subsection, one should be able to match the three peaks in Figure 3.2b with those of a Mn-oxide and a Mn-Co-Ni blended oxide. However, different varieties of active materials composed of these metals have been reported in the literature. We examined different candidates from the literature by comparing their differential capacity signatures to that of our unknown cathode. The first peak at 3.743 V closely matches that observed for $LiNi_{1/3}Mn_{1/3}Co_{1/3}O_2$ denoted here as NMC [19], whereas the other two peaks at 4.005 and 4.136 V correspond well to $LiMn_2O_4$ denoted as LMO [73] (see Figure 3.2c). This agreement provides strong support for the results obtained from the SEM and EDX analysis.
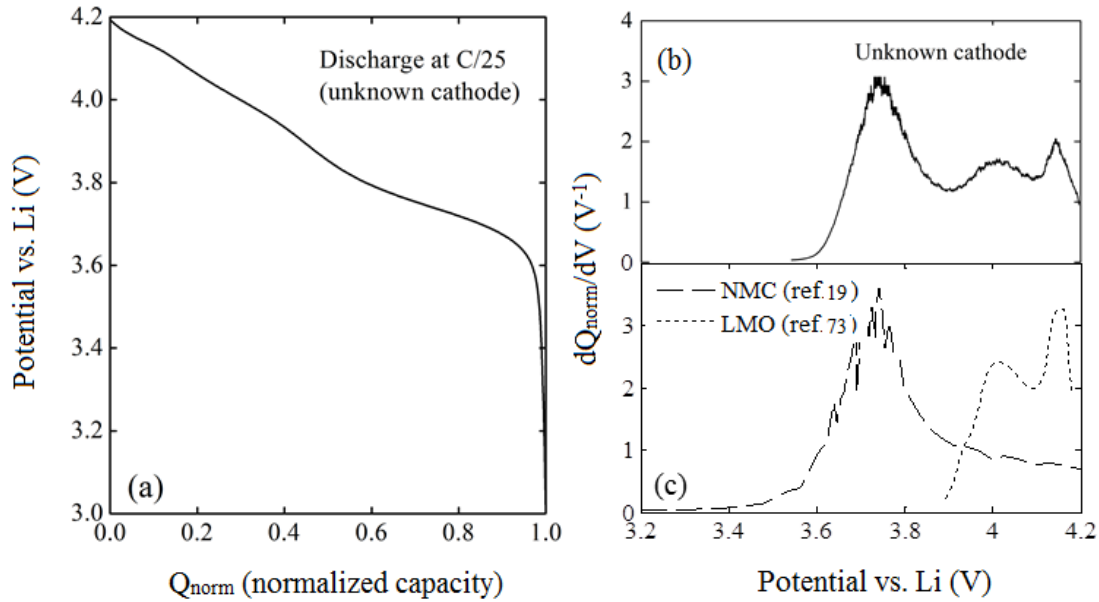
Figure 3.2: (a) Experimental potential-Q_{norm} profile and (b) corresponding experimental differential capacity signature of the unknown cathode/Li cell discharged at current C/25. (c) Differential capacity profiles of LMO and NMC electrodes reported in Refs.[73] and [19], respectively.

3.3.3 Model-based composition estimation

In the previous section, LMO and NMC were identified as the active compounds in the unknown cathode. Here, the mathematical model introduced earlier is used to simulate the discharge curves from which the composition of the unknown cathode can be determined. The list of model parameters used in the simulations is presented in Table 3.2.

Table 3.2: List of model parameters.

Parameter	Symbol	LMO	NMC
Number of particle groups	N	2	
Faraday constant (C mol^{-1})	F	96478	
Gas constant (J mol^{-1} K^{-1})	R	8.314	
Temperature (K)	T	298	
Electrolyte concentration (mol m^{-3})	c_e	1000^{m}	
Radius of type n particle (µm)	R_n	0.87^{m}	0.435^{m}
Capacity of unknown cathode (Ah)	Q	0.002^{m}	
Density of type n particle (kg m^{-3})	ρ_n	4220	4770
Capacity of type n particle (Ah kg^{-1})	q_n	100[73]	150[19]
Maximum lithium concentration in type n particle (mol m^{-3})	c_n^{max}	23339[73]	49761[19]
Rate constant of charge transfer reaction on type n particle surface (mol/[m^{2}s(mol m^{-3})$^{1.5}$])	k_n	5×10^{-10}[73]	1×10^{-10}[73]
Diffusion coefficient of Li in type n particle (m^2 s^{-1})	D_n	6.5 10^{-15}[73]	$1.25\ 10^{-13}\ y^2 - 2.68\ 10^{-13}\ y + 1.44\ 10^{-13}$ (y is coefficient in $Li_y Ni_{1/3} Mn_{1/3} Co_{1/3} O_2$)[19]

m: measured or based on experimental conditions.

In the solid phase, a constant diffusion coefficient for LMO is used with a slight adjustment based on Ref. [73], while a variable diffusion coefficient for NMC that depends on the Li content is fitted in accordance with GITT (galvanostatic intermittent titration technique) analysis in Ref.[19]. The equilibrium potentials U_n for LMO and NMC have been obtained from Ref. [73] and Ref. [19], respectively, to be within the operating potential window of 3V–4.2V used in this

study. Accordingly, given the theoretical capacities and assuming both active materials are fully-lithiated at the potential of 3 V, Li stoichiometry is determined to vary from 0.35 to 1 in LMO and from 0.457 to 1 in NMC in the blended cathode of our study. It should be noted that C/25 conditions were considered in Refs. [73] and [19] to be slow enough that the potentials measured during discharge approximate the open-circuit potentials and, thus, are suitable equilibrium potentials of the individual compounds. With these values as well as the reaction rate constant and solid-state diffusion coefficient known from the literature, the only unspecified parameters are the total active material loading M_t and the mass fractions ε_n of the two active materials. The model can then be used to simulate the discharge profiles for different arbitrarily-set values of ε_n and the corresponding M_t obtained from Eqn. 3.7 to yield the values shown in Table 3.3.

Table 3.3: Calculated total active material loading $\boldsymbol{M_t}$ for the mass fractions ε_n used in the simulations.

Parameter	Values										
ε_1	0	0.1	0.2	0.3	0.4	0.5	0.6	0.7	0.8	0.9	1.0
ε_2	1.0	0.9	0.8	0.7	0.6	0.5	0.4	0.3	0.2	0.1	0
M_t(mg)	13.3	13.8	14.3	14.8	15.4	16.0	16.7	17.4	18.2	19.0	20.0

Figure 3.3 presents the simulated LMO–NMC blended cathode discharge profiles (dashed lines) obtained at C/25 for 11 NMC compositions at equal intervals between 0 wt% and 100 wt%. The experimental discharge profile (solid line) of the unknown cathode is superimposed in Figure 3.3 to compare with the model-computed curves. It should be emphasized that no parameters have been adjusted to fit the model to the measured discharge curve and the computed and experimental curves are simply overlaid together. The comparison clearly shows that the

simulation corresponding to a NMC composition of 70 wt% provides a very close match to the experimental data.
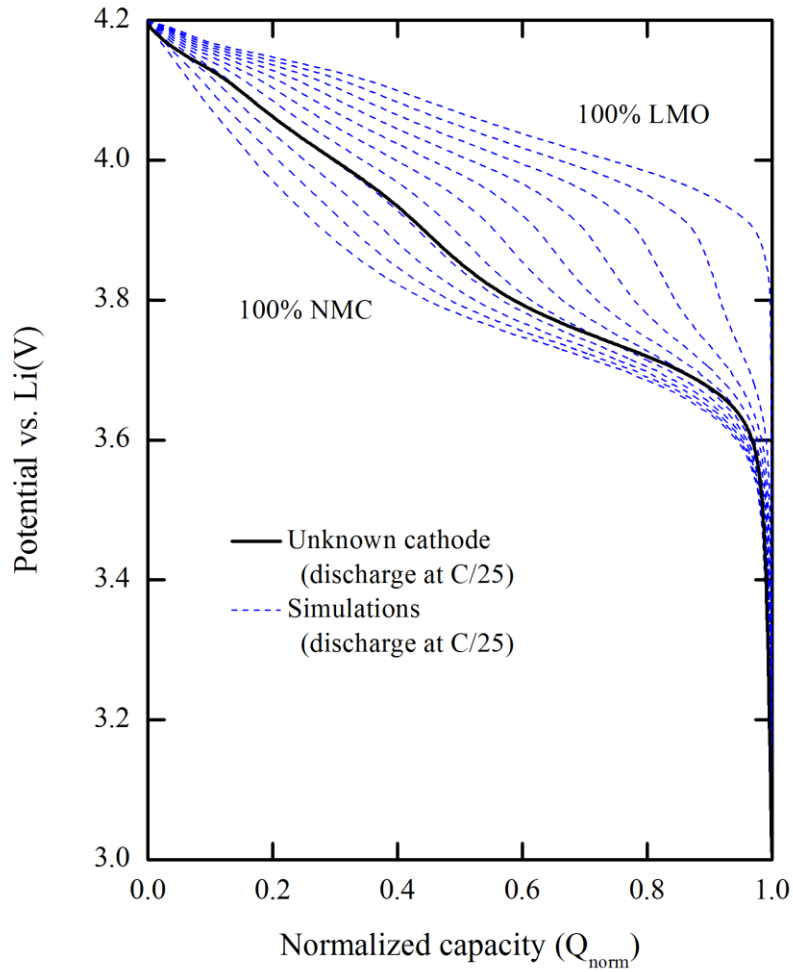
Figure 3.3: Experimental discharge profile (solid line) of unknown cathode at C/25 and simulated discharge profiles (dashed lines) of a LMO-NMC blended-cathode discharge at C/25 for 11 NMC compositions at equal intervals between 0 and 100 wt%.

3.3.4 X-ray-based composition refinement

In order to validate the model prediction, an X-ray-based method is used to estimate the composition of the unknown cathode. This method is based on the concept that the composition of a mixture of crystalline phases in a sample can be determined from the relative areas under their characteristic diffraction peaks. Accordingly, a calibration curve consisting of a plot of the ratio of the areas under the characteristic XRD peaks associated with the two components in a LMO–NMC mixture versus the mixture composition was prepared. To obtain such a calibration curve, pure LMO and NMC powders from Sigma Aldrich were blended in different mass ratios (i.e., 20%, 40%, 60%, 80% NMC) and the XRD patterns of these mixtures together with those of pure LMO and NMC powders were obtained. For this purpose, the evolution of the relative XRD peak intensities corresponding to the (101) plane ($R\bar{3}m$ space group) for LMO and the (311) plane ($Fd3m$ space group) for NMC was used for all compositions [58, 86-87]. The experimental XRD patterns for the four samples composed of 20 to 80 wt% NMC are presented in Figure 3.4.
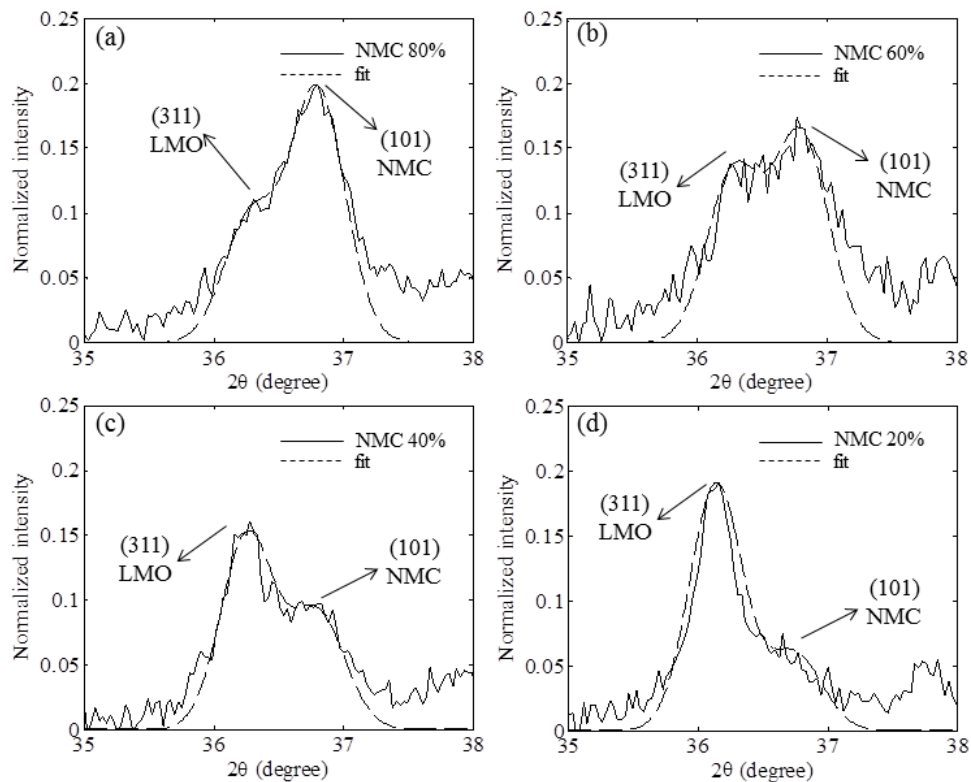
Figure 3.4: Experimental XRD patterns (solid lines) of NMC-LMO powder mixtures with compositions (a) 20, (b) 40, (c) 60 and (d) 80 wt% NMC and pseudo-Voigt fitted patterns (dashed lines) of (101) NMC and (311) LMO peaks for 2θ between 35° and 38°.

Figure 3.4a-d clearly show that the (101) NMC peak grows at the expense of the (311) LMO peak as the weight percentage of NMC in the mixture increases. The pseudo-Voigt function is fitted to each of the patterns in Figure 3.4a-d to approximate the area under each peak. The ratio of the area under the (101) NMC peak to the area under both (101) NMC and (311) LMO peaks is plotted versus the weight fraction of NMC in the NMC–LMO mixture in Figure 3.5(circles).
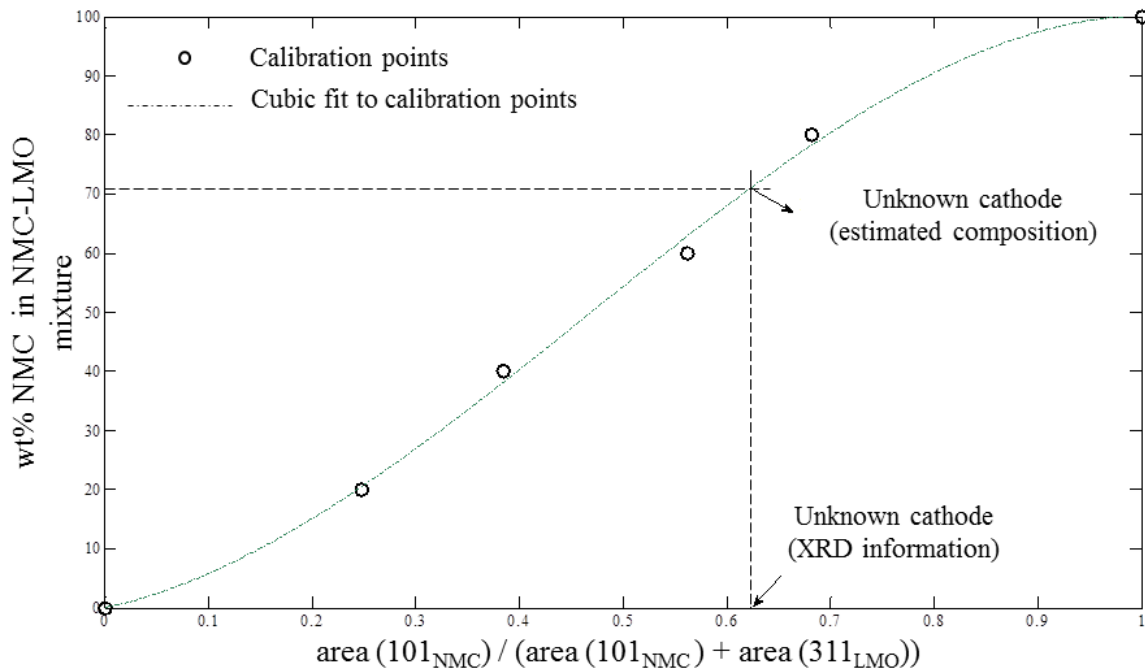
Figure 3.5: XRD-based calibration plot (circles and dotted line) correlating the ratio of the area under (101) NMC peak to the area under both (101) NMC and (311) LMO peaks to wt% NMC in a NMC-LMO mixture.

The cubic function below (Eqn. 3.9) has been found to fit the experimental data very well and is also included in Figure 3.5 (dashed line) so that the composition of any unknown mixture of NMC and LMO can be estimated from the XRD data:

$$y = -1.6x^3 + 2.3x^2 + 0.34x + 0.0007 \tag{3.9}$$

where x is the ratio of the area under the (101) NMC peak to the area under both (101) NMC and (311) LMO peaks and y is the weight fraction of NMC in the NMC–LMO mixture.

The XRD diffractogram of the unknown blended cathode is presented in Figure 3.6. The inset shows the diffraction pattern magnified between 35° and 38° (solid line) and the pseudo-Voigt

functions fitted to the (101) NMC and (311) LMO peaks (dashed lines). From the areas under these peaks obtained from the pseudo-Voigt fits and the calibration curve in Figure 3.5, the composition of the unknown cathode is estimated to be 71 wt% NMC. This composition is very close to the one predicted by the model-based method (i.e., 70%). This level of agreement between the two methods indicates that the simple model-based approach proposed in this study is of acceptable accuracy and should prove valuable as a versatile technique for determination of the composition of unidentified blended electrodes. One reason for the very good level of agreement achieved using the physic-based model may be that it is able to capture interactions between the active compounds by considering the particles to be connected to each other in parallel at every location across the electrode so that they remain at the same electric potential throughout lithiation/delithiation regardless of the rate condition. If the particles have the same chemistry (i.e., identical equilibrium potential curves), they will have identical Li-content; however, if the particles have different chemistries, they will be lithiated/delithiated to different extents at any particular time depending on their equilibrium potentials. Possible interactions between active components are not considered in the previous OCV models in which the differential capacity curve of the blended cathode is obtained through a linear combination of the OCVs of the individual compounds weighted according to their mass ratios. The error associated with the OCV models [63, 79, 81] would likely diminish if the actual equilibrium potentials (i.e., potential of the relaxed electrode under open-circuit condition) rather than the quasi-equilibrium potentials (i.e., C/25 galvanostatic discharge curve) were being measured because the interactions between the active compounds disappear under this condition. Although C/25 condition is slow enough for the galvanostatic potential-capacity curve to approximate the

equilibrium potential of a single active-compound electrode, care must be taken in making such

an assumption for an electrode containing different active chemistries.
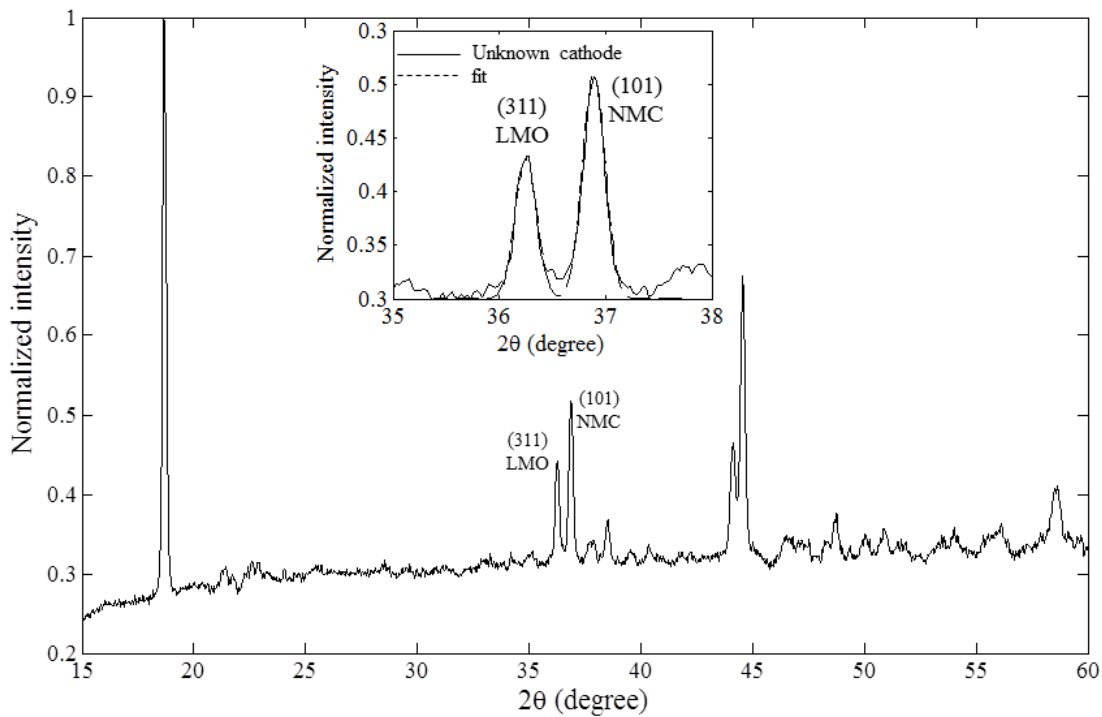
Figure 3.6: XRD pattern of unknown blended cathode. The portion of the pattern and the pseudo-Voigt fit of the (101) NMC and (311) LMO peaks (dashed line) are shown at higher resolution over the 2θ range between 35° and 38° in the inset.

Chapter 4 Multi-Particle model for the blended cathode

The following section is based on previously published work 'Multi-Particle Model for a Commercial Blended Lithium-Ion Electrode, *J. Electrochem. Soc.,* 163(3), A458 (2016)' by Z. Mao et al. and is reproduced by permission from *Journal of The Electrochemical Society*. This thesis author specific contribution to this paper was to: develop the model, conduct the simulations and experiments, prepare all the graphics and results, and prepare the final manuscript and reviewer edits with direction from the project supervisors who were M. Fowler, Z. Chen and M. Pritzker. M. Farkhondeh offered advice on the modelling and experiments.

4.1 Introduction

Research and development of lithium-ion batteries (LIBs) has been underway for several decades. Numerous successive technical breakthroughs have enabled them to become more and more commercially viable for applications ranging from portable electronics to power tools. However, for automotive applications, LIBs face particular materials and engineering challenges: both their energy and power requirements have to be met simultaneously while slowing the aging process so that vehicle lifespan is commercially viable. Such a synergic effect has been realized to a good extent by loading battery electrodes with two or more active materials. Each of the active materials features at least one required characteristic property of the blended electrode systems [88]. Examples of such blended systems are layered-layered mixtures of $LiNi_xCo_yAl_{1-x-y}O_2$ - $LiCoO_2$ (NCA-LCO) [81], layered-spinel mixtures of $LiNi_xCo_yAl_{1-x-y}O_2$ -$LiMn_2O_4$ (NCA-LMO) [73, 84], $LiNi_xMn_yCo_{1-x-y}O_2$ -$LiMn_2O_4$ (NMC-LMO) [79], layered-olivine mixtures of $LiCoO_2$-$LiFePO_4$ (LCO-LFP)[89] and spinel-olivine mixtures of $LiMn_2O_4$-$LiFePO_4$ (LMO-LFP) [90].

Porous composite electrodes are at the heart of LIBs and their properties and manufacturing methods are of crucial importance. The main steps for the preparation of LIB electrodes include active-material selection, material synthesis and electrode manufacturing (formulation and fabrication). Properties such as the active particle size distribution (PSD) are the primary objectives when optimizing the performance of an electrode since these properties directly determine the power capability of the electrode. Electrode manufacturing, on the other hand, contributes to the electrode microstructure. More specifically, additives and fillers should be well dispersed and undergo little or no particle clustering or agglomeration. This will assure a uniform porosity distribution across the electrode and less tortuous ionic and electronic pathways reaching the active particles. Overall, the fabrication of electrode should contribute to maximizing and stabilizing battery capacity, lifetime and rate capability.

Active material PSD has been shown to affect the electrochemical performance of LIB electrodes [35, 83, 91-93]. These studies have been used to theoretically explain some phenomena associated with the particle-size distribution, such as poor columbic efficiency and longer open-circuit relaxation time of an electrode with a non-uniform PSD compared to the one with a uniform PSD [91], rate-dependent dynamics of $LiFePO_4$ electrodes [35, 83], the effect of particle size on lithium deposition when a LIB becomes overcharged [92] and the influence of non-uniform size distribution on the electrode packing density [93].

Optimal design and operation of blended cathode systems benefits from physics-based mathematical models which can describe the response of the electrode to various charge/discharge pulses. Few mathematical models for blended cathodes have been reported in the literature. Albertus et al. used a physics-based model to simulate the electrochemical

behavior of NCA-LMO blended electrodes at various compositions. Their model which featured a distribution of resistances among the electrode particles (i.e., in line with the resistive reactant model [34, 83, 94]) and was able to satisfactorily fit experimental data [73]. Jung et al. compared simulation results to experimental galvanostatic discharge data from graphite-soft carbon/NMC-LMO full cells at various anode and cathode compositions [79].

In Chapter 3, a simple mathematical model was developed to estimate the composition of an unknown commercial blended cathode by simulating galvanostatic discharge under a low-rate condition. This approach which combines experimental data from X-ray powder diffraction and differential-capacity analysis with a mathematical model was shown to successfully characterize the unknown blended electrode (NMC-LMO) and accurately estimate its composition (in that case a 7:3 mass ratio). The model presented in the current communication is intended for a different purpose. It is more comprehensive and accounts for porous electrode effects and the particle-size distribution of the active materials in the previously identified NMC-LMO blended cathode. The model is suitable for a wide range of rate conditions from C/25 to 2C. Simulations are compared with experimentally determined galvanostatic discharge and differential-capacity curves and used to determine the contribution of each cathode component to the capacity. Finally, the effect of particle size on the electrode rate capability is discussed.

4.2 Experimental

In this study, some physical and electrochemical parameters of a fresh and unused commercial NMC-LMO blended cathode such as thickness and the effective electronic conductivity were measured and then used to develop parameters for a mathematical model. To obtain its

electrochemical performance, the same blended cathode was used to fabricate cathode|separator|Li coin cells. The procedure involved opening and disassembling a commercial pouch cell, taking out a cathode sheet (double-side-coated on aluminum current collector) and removing the electrode coating on one side of the sheet. This was done using N-methyl-2-pyrrolidone (NMP) solvent. Circular samples (A = 1.013 cm^2) were then punched from the one-sided electrode for coin cell assembly. To remove any possible electrolyte salt deposit, the circular samples were washed and rinsed with dimethyl carbonate (DMC). The washed samples were examined by SEM (Zeiss ULTRA) to characterize their surface morphology and to measure the electrode thickness prior to being fabricated into coin cells. Li was used as the reference/counter electrode in the coin cells. The electrodes were separated by Celgard 2500 soaked with an electrolyte containing 1 M $LiPF_6$ dissolved in a 1:1 EC/DMC solution. The entire cell fabrication process from the opening of the pouch cell to the washing of the samples in DMC and finally to the assembly of the coin cells was carried out in an argon-filled glove box.

A series of galvanostatic experiments was conducted on coin cells using a Neware CT-3008-5V10 mA-164-U battery cycler. Prior to these experiments, the cells were first subjected to a sequence of 5 formation cycles identical to the one used in our previous study in Chapter 3 to ensure that the coin cells had reached a stable state and behaved consistently and repeatable during the subsequent galvanostatic tests. The waveform during each of these 5 formation cycles was identical. It consisted of the following steps: i) charging at a constant rate of C/2 until a potential of 4.2 V was reached, ii) 60 min. rest period (i.e., zero current), iii) charging at a constant rate of C/100 until a potential of 4.2 V was reached, iv) 60 min. rest period, v) discharging at a constant rate of C/2 until a potential of 3.0 V was reached, vi) 60 min. rest

period, vii) discharging at a constant rate of C/100 until a potential of 3.0 V was reached and viii) 60 min. rest period. Due to equipment limitations, galvanostatic experiments were conducted in the constant-current constant-current (CC-CC) mode instead of constant-current constant-voltage (CC-CV) mode, and the second CC step at a very small C-rate i.e., steps iii) and vii) above, was to ensure that the electrode was fully lithiated (delithiated) by the end of discharge (charge), whose purpose is the same to that of CV in CC-CV mode.

Following these 5 formation cycles, a series of galvanostatic experiments was carried out, each of which consisted of the following steps: i) charging at a particular rate until a potential of 4.2 V was reached, ii) 3-hour rest period, iii) charging at C/100 until a potential of 4.2 V was reached, iv) 3-hour rest period, v) discharging at the same rate as step i) until a potential of 3.0 V was reached, vi) 3-hour rest period , vii) discharging at C/100 until a potential of 3.0 V was reached , iv) and 3-hour rest period. Currents applied during steps i) and v) of this series of experiments followed the sequence: C/25, C/10, C/5, C/2, 1C and 2C. 1C rate corresponds to 2mA applied current.

The effective electronic conductivity of the electrode was measured using a four-probe setup consisting of a probe fixture (probe head: C4S 67/1, Cascade microtech Inc.) and a source meter (Keithley 2440 5A Source Meter, Keithley Instruments Inc.). More details regarding this measurement procedure are given in Ref. [95]. The electronic conductivity of the porous electrode is expected to be several orders of magnitude smaller than that of the aluminum current collector ($\sim 3.5 \times 10^7$ S m^{-1}). Conductivity measurement of a 2-layer aluminum/porous electrode medium is therefore prone to a significant error because most of the applied current flows through the aluminum layer and bypasses the porous electrode, not to mention the

influence of the contact resistance between the two layers on conductivity measurements. To avoid such unnecessary errors, the aluminum current collector was dissolved by dipping the samples in a 1 M NaOH solution for a very short period of time (1-3 minutes). The electrode was then rinsed with DI water to remove the remainder of the solute as well as the reaction products and dried on a glass slide at room temperature. Care was taken not to damage the delaminated electrode.

4.3 Mathematical Model Development
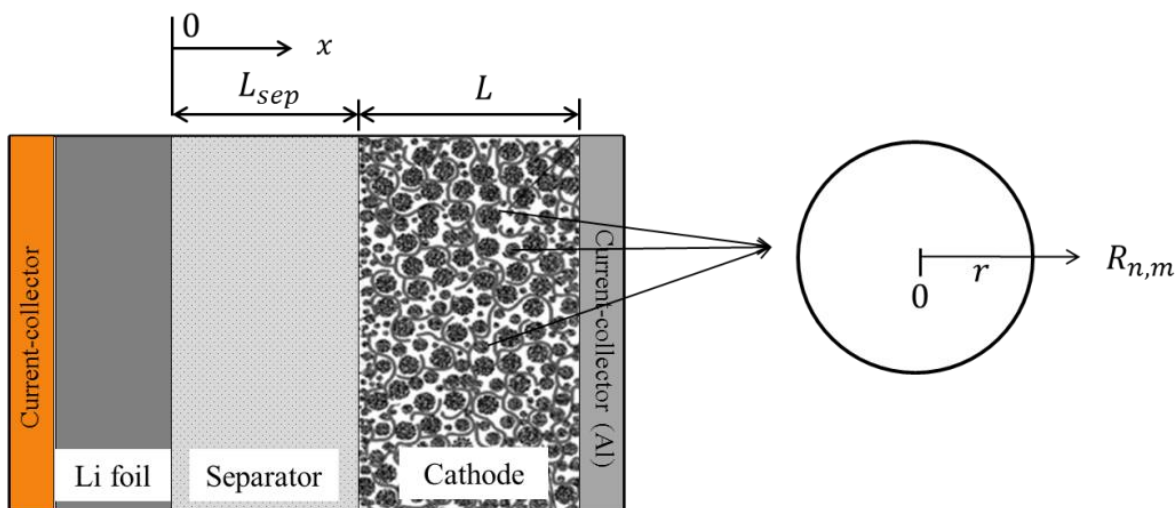
Figure 4.1: Schematic diagram of the porous half-cell containing a blended cathode for which a multi-particle pseudo-two-dimensional model is developed.

A previously developed pseudo-two dimensional (P2D) electrochemical model [84] is adapted here to account for particles having a different chemical nature and a non-uniform size distribution as shown in Figure 4.1. The model is used to simulate the rate capability of NMC-LMO blended cathodes and is validated against experimental data. The charge/discharge process

involves phenomena occurring on the particle-scale and electrode-scale which are included in the model. At the particle-scale, lithiation/delithiation within each particle is controlled by solid-state diffusion of lithium ions that is coupled with charge-transfer reactions at the surface. The porous-electrode theory of Newman and co-workers [96] is applied to describe electrode-scale transport within the cathode domain. It is assumed that the blended electrode consists of spherical particles that are distinguished in terms of their active material type n and size class m defined by their radii $\boldsymbol{R_{n,m}}$. N total types of active material are present and the range of particles radii is discretized into M total size classes. Furthermore, any single particle consists of only one type of active material. The transport equation and associated boundary conditions describing the diffusion of Li ions within each particle of radius $\boldsymbol{R_{n,m}}$ are given by Eqns. 4.1-4.3 below:

$$\frac{\partial c_{n,m}}{\partial t} = \frac{1}{r^2}\frac{\partial}{\partial r}\left(D_{n,m}r^2\frac{\partial c_{n,m}}{\partial r}\right) \tag{4.5}$$

$$\frac{\partial c_{n,m}}{\partial r}\Big|_{r=0} = 0 \tag{4.6}$$

$$\frac{\partial c_{n,m}}{\partial r}\Big|_{r=R_{n,m}} = -\frac{i_{n,m}}{FD_{n,m}} \tag{4.7}$$

where $c_{n,m}$ is the intercalated Li concentration in the active material n with the particle size class m, $i_{n,m}$ is the current density on the surface of active material n with the particle size class m, r is the radial distance from the center of the particle, t is time and F is the Faraday constant. $D_{n,m}$ is the chemical diffusion coefficient for the intercalated species within active material n with the particle size class m and is related to the thermodynamic factor $\alpha_{n,m}$ and binary diffusion coefficient $\mathcal{D}_n$, as given in Eqns. 4.4-4.5 below [35, 83, 97]:

$$D_{n,m} = \alpha_{n,m} \mathcal{D}_n \tag{4.4}$$

$$\alpha_{n,m} = -\frac{F}{RT} y_{n,m} (1 - y_{n,m}) \frac{\partial U_{n,m}}{\partial y_{n,m}} \tag{4.5}$$

Active materials are considered to be non-ideal solid solutions with the non-idealities manifested by their thermodynamic factors. The derivation of the above expression for the thermodynamic factor from the equilibrium potential can be found in detail in Refs. [83] and [35]. In Eqns. 4.4 and 4.5, $y_{n,m}$ is the normalized lithium concentration in active material n with the particle size class m calculated from the ratio of the lithium concentration $c_{n,m}$ at any point along the particle radius to the maximum concentration c_n^{max}, i.e., $y_{n,m} = c_{n,m}/c_n^{max}$. The current density $i_{n,m}$ is related to the exchange current density $i_{n,m}^0$ and overpotential $\eta_{n,m}$ on the surface of active material n with the particle size class m by the Butler-Volmer equation:

$$i_{n,m} = i_{n,m}^0 \left[\exp\left(\frac{(1-\beta_n)F}{RT} \eta_{n,m} \right) - \exp\left(-\frac{\beta_n F}{RT} \eta_{n,m} \right) \right] \tag{4.6}$$

where,

$$i_{n,m}^0 = F k_n (c_e)^{(1-\beta_n)} \left(c_{s,n,m} \right)^{\beta_n} \left(c_n^{max} - c_{s,n,m} \right)^{\beta_n} \tag{4.7}$$

$$\eta_{n,m} = \Phi_1 - \Phi_2 - U_{n,m}(y_{n,m}) \tag{4.8}$$

$c_{s,n,m}$, $U_{n,m}(y_{n,m})$, k_n and β_n are the surface concentration, equilibrium potential, rate constant and transfer coefficient, respectively, associated with the charge-transfer reaction on the surface of active material n with the particle size class m. Φ_1 is the potential of the solid-phase (conductive matrix) and Φ_2 is the potential of the liquid-phase (electrolyte) in immediate contact

with the active materials along the electrode thickness. Finally, c_e, T and R are the electrolyte concentration, temperature and gas constant, respectively. The governing equations describing the system at the electrode level are listed in Table 4.1.

Table 4.1: Electrode-level equations.

Solid-phase charge balance	Boundary conditions
$i_1 = -\sigma_{\text{eff}}\nabla\Phi_1$	$i_1 = 0$ at $x = L_{\text{sep}}$
$\nabla \cdot i_1 = -\xi \displaystyle\sum_{n=1}^{N}\sum_{m=1}^{M} \xi_{n,m} a_{n,m} i_{n,m}$	$i_1 = I/A$ at $x = L_{\text{sep}} + L$
$\displaystyle\sum_{n=1}^{N}\sum_{m=1}^{M} \xi_{n,m} = 1$	
$a_{n,m} = \dfrac{3}{R_{n,m}}$	
$E = \Phi_1\big\|_{x=L_{\text{sep}}+L} - \Phi_{\text{f}}$	

Liquid-phase charge balance	
$\nabla . i_2 = 0$	$\Phi_2 = 0$ at $x = 0$
$i_2 = -\kappa_{\text{eff,sep}}\nabla\Phi_2 + \dfrac{2\kappa_{\text{eff,sep}}RT(1-t_+^0)}{Fc_e}\left(1 + \dfrac{d\ln f_\pm}{d\ln c_e}\right)\nabla c_e$	$i_2\|_{\text{sep}} = i_2\|_{\text{cat}}$ at $x = L_{\text{sep}}$
$\kappa_{\text{eff,sep}} = \kappa\varepsilon_{\text{sep}}^{\gamma}$	
$\nabla . (i_1 + i_2) = 0$	$i_2\|_{\text{sep}} = i_2\|_{\text{cat}}$ at $x = L_{\text{sep}}$
$i_2 = -\kappa_{\text{eff,cat}}\nabla\Phi_2 + \dfrac{2\kappa_{\text{eff,cat}}RT(1-t_+^0)}{Fc_e}\left(1 + \dfrac{d\ln f_\pm}{d\ln c_e}\right)\nabla c_e$	$i_2 = 0$ at $x = L_{\text{sep}} + L$
$\kappa_{\text{eff,cat}} = \kappa\varepsilon_{\text{cat}}^{\gamma}$	

Electrolyte mass balance	
$\varepsilon_{\text{sep}}\dfrac{\partial c_e}{\partial t} = \nabla \cdot \left(\varepsilon_{\text{sep}} D_{\text{eff,sep}}\nabla c_e\right) - \dfrac{i_2 \nabla t_+^0}{F}$	$\varepsilon_{\text{sep}}\dfrac{\partial c_e}{\partial x} = -\dfrac{I(1-t_+^0)}{FD_{\text{eff,sep}}A}$ at
$D_{\text{eff,sep}} = D_e\varepsilon_{\text{sep}}^{\gamma-1}$	$x = 0$

$$\dfrac{\partial c_e}{\partial x}\Big|_{\text{sep}} = \dfrac{\partial c_e}{\partial x}\Big|_{\text{cat}} \text{ at } x = L_{\text{sep}}$$

$$\varepsilon_{\text{cat}}\dfrac{\partial c_e}{\partial t} = \qquad\qquad \dfrac{\partial c_e}{\partial x}\Big|_{\text{sep}} = \dfrac{\partial c_e}{\partial x}\Big|_{\text{cat}} \text{ at } x = L_{\text{sep}}$$

$$\nabla \cdot \left(\varepsilon_{\text{cat}}D_{\text{eff,cat}}\nabla c_e\right) - \dfrac{i_2 \nabla t_+^0}{F} + \dfrac{(1-t_+^0)\xi \sum_{n=1}^{N}\sum_{m=1}^{M}\xi_{n,m}a_{n,m}i_{n,m}}{F} \qquad \dfrac{\partial c_e}{\partial x} = 0 \text{ at } x = L_{\text{sep}} + L$$

$$D_{\text{eff,cat}} = D_e \varepsilon_{\text{cat}}^{\gamma-1}$$

$$D_e = \dfrac{c_T}{c_0}\left(1 + \dfrac{\text{dln}f_\pm}{\text{dln}c_e}\right)\mathcal{D}_e$$

Lithium foil counter electrode kinetics

$$I = -Ai_f^0\left[\exp\left(\dfrac{(1-\beta_f)F}{RT}(\Phi_f - \Phi_2|_{x=0})\right) - \exp\left(-\dfrac{\beta_f F}{RT}(\Phi_f - \Phi_2|_{x=0})\right)\right]$$

The charge balance across the conductive matrix of the porous electrode can be expressed as the sum of the electronic current densities entering/leaving all active material particles [96]:

$$\nabla \cdot i_1 = -\xi \sum_{n=1}^{N}\sum_{m=1}^{M}\xi_{n,m}a_{n,m}i_{n,m} \tag{4.9}$$

where i_1 is the electronic current density through the conductive matrix and obeys the electroneutrality condition with the liquid-phase current density i_2, i.e., $\nabla \cdot (i_1 + i_2) = 0$. ξ is the total volume fraction of all active materials in the entire electrode and can be calculated from the electrode capacity Q and active material capacity q_n. $a_{n,m}$ is the specific surface area and is calculated from the particle radius $R_{n,m}$, i.e., $a_{n,m} = 3/R_{n,m}$. $\xi_{n,m}$ is the volume fraction of particles composed of active material n with size m relative to the volume of all active materials and can be calculated from the density ρ_n and mass fraction $\xi'_{n,m}$ as follows:

$$\xi_{n,m} = \dfrac{\xi'_{n,m}/\rho_n}{\sum_{n=1}^{N}\left(\sum_{m=1}^{M}\xi'_{n,m}/\rho_n\right)} \tag{4.10}$$

subject to the condition,

$$\sum_{n=1}^{N} \sum_{m=1}^{M} \xi_{n,m} = 1 \qquad\qquad (4.11)$$

The mass fraction of each active material was determined using the method described in detail in the previous chapter. The mass fraction of each particle size class in each active material was obtained by fitting the model to experimental discharge curves, as will be discussed in the next section.

All equations at the particle and electrode scales were coupled and solved simultaneously using the COMSOL Multiphysics 4.4 finite-element simulation package. The electrode and separator in the x-direction were each discretized into 10 intervals, while the particle domain was discretized into 20 elements in the r-direction. All equations were solved numerically until the simulation reached the stop condition corresponding to a cell voltage of 3.0 V on discharge.

4.4 Results and Discussions

4.4.1 Surface morphology and particle size measurement
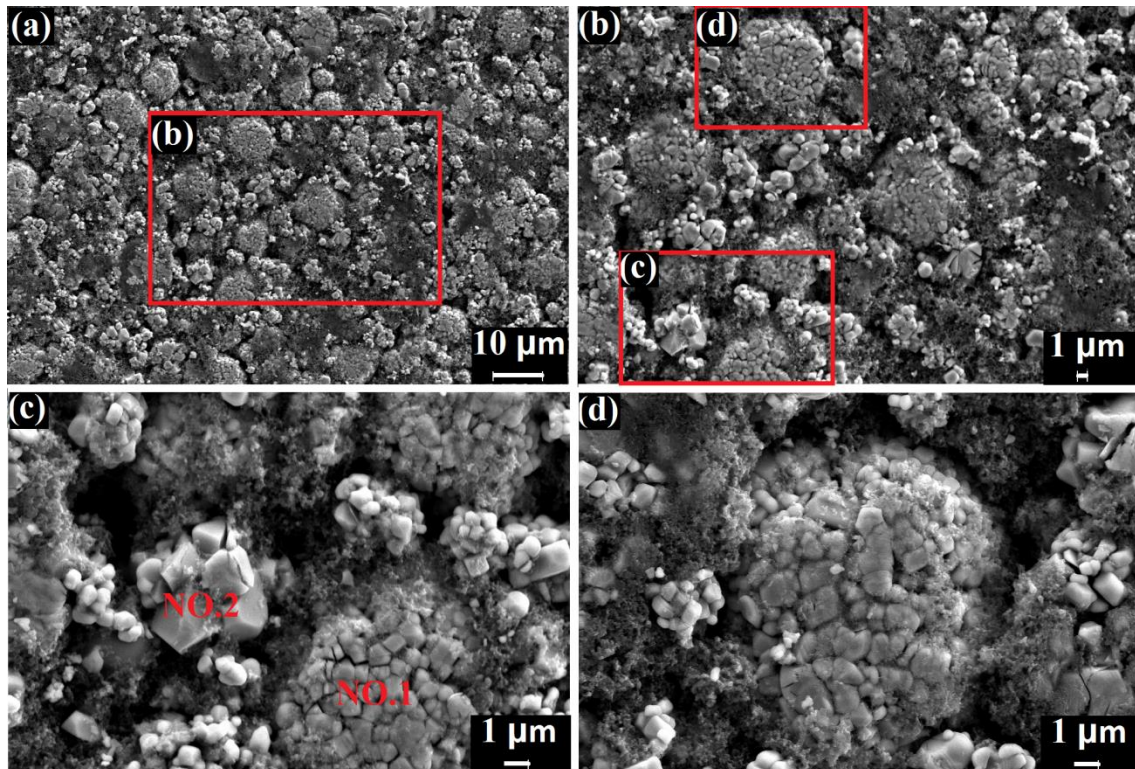
Figure 4.2: SEM images of NMC-LMO blended cathode surface obtained at different magnifications. Image in (a) is shown at 1000x. Highlighted region in (a) is shown at magnification 2000x in (b). Highlighted regions in (b) are shown at magnification 5000x in (c) and (d).

SEM examination of the morphology of the electrode surface at 1000x and 2000x magnification in Figure 4.2a and 4.2b, respectively, reveals a structure that is relatively homogeneous, but made up of particles with a complex size distribution. Figure 4.2c shows an enlarged view of the

area labelled as (c) in Figure 4.2b. It clearly reveals two types of particles that are labelled as NO.1 and NO.2. As described in detail previously (Chapter 3), NO.1 corresponds to NMC particles and NO.2 to LMO particles, while the composition of the blended cathode is 70 wt% NMC and 30 wt% LMO. Furthermore, previous SEM and EDX analysis of the morphology of the electrode surface shown in Figure 4.2c and 4.2d clearly revealed the presence of NMC particles with two distinctly different size distributions. The first group of these particles is very small with a diameter smaller than 1µm and is termed 'primary' or 'submicron' for our purposes here. The other group includes larger particles that are a few micrometers in diameter and termed 'secondary' or 'micron' particles. These secondary particles have presumably formed by the agglomeration/clustering of the primary particles. The LMO particles for the most part are large with diameters of 1 – 3 µm. The large size difference between NMC primary and secondary particles, i.e., 'submicron' and 'micron' scale, with a ratio of ca. 1:10 can be observed while LMO 'clusters' are composed of only a few distinguishable particles of a ratio of ca. 1:3 compared to the size of the cluster itself. Based on these considerations, we sub-divided NMC particles into a submicron group and a micron group and fit a separate particle-size distribution for each portion. Due to the difficulty in experimentally separating the NMC and LMO particles from each other and using standard particle size measurement techniques on each group to obtained their size distributions, we determined their sizes directly from SEM images and took advantage of the fact that EDX analysis enabled us to distinguish between NMC and LMO particles. The method we adopted was to analyze more than 300 NMC particles from several SEM images obtained at 5000x and 1000x magnification, measure their diameters from these images, separate them into submicron (smaller than 1µm) and micron (larger than 1µm) groups

and fit functions to the size distributions of these two groups. Similarly, we analyzed more than 300 LMO particles from several SEM images at 5000x magnification, measured their diameters and fit a single function to their size distribution.

The cumulative PSDs of the three groups of active materials, i.e., submicron and micron groups for NMC and one group for LMO, measured from the SEM images are shown in Figure 4.3. In each of the three cases, a log-normal function was found to fit the experimental data very well. d_{50} values of 0.87μm and 9.29 μm were obtained for the NMC submicron and micron groups, respectively, and 1.74 μm for the LMO particles.
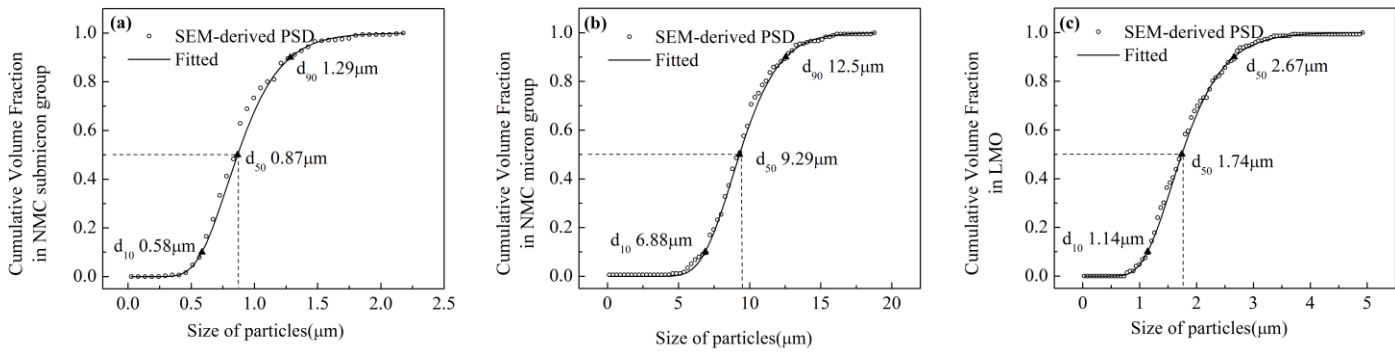
Figure 4.3: Measured (symbols) and fitted (solid line) particle size distributions for (a) NMC submicron group, (b) NMC micron group and (c) LMO. d_{10}, d_{50} and d_{90} values are marked in each case.

Although the complete size distributions for the submicron and micron groups of NMC particles and micron group of LMO particles can be incorporated into Eqns. 4.1-4.3, this would greatly complicate the model. Before resorting to such a level of complexity, we adopt the simpler approach of assuming the particles in each of these groups have uniform size with a diameter

given by the corresponding d_{50}. Thus, using the nomenclature presented above, $N = 2$ since the cathode contains two types of active materials NMC and LMO. NMC particles have two sizes ($M = 2$), while LMO particles have only one size ($M = 1$). If $n = 1$ corresponds to NMC and $n = 2$ to LMO, then the particle radius $R_{1,1} = 0.435$ μm, $R_{1,2} = 4.65$ μm and $R_{2,1} = 0.87$ μm (see Table 4.2).

Table 4.2: List of model parameters.

Parameter	Symbol	LMO	NMC
Cathode area (m^2)	A	0.0001013^{m}	
Electrode thickness (m)	L	$5.7\times10^{-5\text{m}}$	
Cathode capacity (Ah)	Q	0.002^{m}	
Total active-material volume fraction	ξ	0.558^{Cal}	
Solid-state thermodynamic factor	$\alpha_{n,m}$	Eqn. 5	
Radius of type n particle in size class m (m)	$R_{n,m}$	$8.7\times10^{-7\text{m}}$	$4.65\times10^{-6\text{m}}$ (micron group) $4.35\times10^{-7\text{m}}$ (submicron group)
Capacity of type n particle (Ah kg^{-1})	q_n	$100^{[73]}$	$151^{[19]}$
Maximum lithium concentration in type n particle (mol m^{-3})	c_n^{max}	$23339^{[73]}$	$49761^{[19]}$
Density of type n particle (kg m^{-3})	ρ_n	$4220^{[a]}$	$4770^{[a]}$
Charge-transfer coefficient for charge transfer on type n cathode particle	β_n	$0.5^{[a]}$	$0.5^{[a]}$
Electrode porosity	ε_{cat}	$0.35^{[a]}$	
Initial electrolyte concentration (mol m^{-3})	c_e	1000^{m}	

Separator thickness (m)	L_{sep}	2.5×10^{-5}[m]
Lithium ions transference number	t_+^0	0.36[a]
Bulk diffusion coefficient in the electrolyte $(m^2 s^{-1})$	D_e	5.2×10^{-10}[83]
Bulk ionic conductivity of the electrolyte (S m^{-1})	κ	1.3[83]
Charge-transfer coefficient for charge transfer on Li foil electrode	β_f	0.5[a]
Separator porosity	ε_{sep}	0.37[Celgard]
Bruggeman exponent	γ	1.5[a]
Effective electronic conductivity (S m^{-1})	σ_{eff}	9.65[m]
Exchange current density on Li foil electrode $(A\ m^{-2})$	i_f^0	20[a]
Faraday constant (C mol^{-1})	F	96485
Gas constant (J $mol^{-1}\ K^{-1}$)	R	8.314
Temperature (K)	T	298

m: measured

Celgard: Celgard product data sheet

a: assumed based on literature

Cal: Calculated based on measurement

According to the model proposed by Dargaville and Farrell [98], agglomerates constitute mesoscale porous particles composed of smaller primary particles and conductive additives with electrolyte filling in the pores. The charge-transfer reaction occurs at the surfaces of the smaller particles wherever both electron and reacting ion are present. In brief, porous-electrode theory can be applied to the secondary particles. However, it adds to the complexity of the model and requires agglomerate parameters to be known. In this analysis, we assume the secondary

particles are nonporous and solid-state diffusion is the sole means of species transport across the particle.

4.4.2 Equilibrium-potential functions

The equilibrium potentials for lithiation/delithiation of NMC and LMO have been obtained from references [19] and [73], respectively. For both materials, C/25 galvanostatic charge/discharge conditions were found to be slow enough for the resulting potential-stoichiometry curves to reflect suitable equilibrium potentials over the potential window of 3.0 - 4.2V. In the current study, we assume that the equilibrium potential of each active material is the average of the charge and discharge curves at any given degree of lithiation obtained at the rate of C/25.

The stability window of the electrolyte used for the cell assembly determines the upper and lower cut-off potentials of any battery active material. With the active materials and the electrolyte used here, the potential window of 3.0 – 4.2 V vs. Li/Li$^+$ guarantees the stability of the two active materials as well as the electrolyte. The theoretical capacity of NMC is 277Ah kg^{-1} while its usable capacity is about 151Ah kg^{-1} (the remaining unused capacity of 126Ah kg^{-1} is used to protect the crystal structure from damage due to excessive charging beyond 4.2 V) [19]. Therefore, the initial value of $y_{n,m}$ for NMC particles in the blended cathode during discharge (final value during charging), which corresponds to the minimum lithium content, was taken to be (277-151)/277 = 0.45. The same analysis holds true for LMO where $y_{n,m}$ = 0.35 for LMO particles at a potential of 4.2V and so $y_{n,m}$ = 0.35 is taken to be the initial value for this component of the blended cathode. Both the simulations and experiments were conducted until $y_{n,m}$ = 1.0 (i.e., assumed to coincide with the lower cut-off potential of 3.0 V) in both types of

particles during discharge. Based on the above consideration, two functions previously proposed in Refs. [99] and [100] are fitted separately to the experimental equilibrium potentials of NMC and LMO to yield Eqns. 4.12 and 4.13, respectively:

$$U_{\text{NMC}}(y_{\text{NMC}}) = 6.51176 - 8y_{\text{NMC}} + 7.1086y_{\text{NMC}}^2 - 1.55y_{\text{NMC}}^3 - 0.459y_{\text{NMC}}^6 - 5.00034 \times$$
$$10^8 \exp(135.089y_{\text{NMC}}^2 - 118.089) \tag{4.12}$$

$$U_{\text{LMO}}(y_{\text{LMO}}) =$$
$$0.225 - 0.392y_{\text{LMO}} + 2.2 \tanh[-1010(y_{\text{LMO}} - 0.994)] + 1.9 \tanh[-21.4(y_{\text{LMO}} - 1.04)] +$$
$$0.181 \operatorname{sech}[23.4(y_{\text{LMO}} - 0.397)] - 0.175\operatorname{sech}[24.2(y_{\text{LMO}} - 0.399)] +$$
$$0.0164 \operatorname{sech}[13.1(y_{\text{LMO}} - 0.567)] + 0.33 \operatorname{sech}[48.1(y_{\text{LMO}} - 1)] \tag{4.13}$$

4.4.3 Effective electronic conductivity

The effective electronic conductivity of the electrode was measured using a four-probe setup. Prior to this conductivity measurement, the samples had been treated by soaking in a 1M NaOH solution for few minutes at ambient temperature and a fast delamination of the electrode had been observed driven by hydrogen bubbling at the interface between the porous electrode and the aluminum current collector. This is due to the fast Al dissolution in the presence of sodium hydroxide according to the following chemical reactions:

$$2\text{Al} + 6\text{H}_2\text{O} \rightleftharpoons 2\text{Al(OH)}_3 + 3\text{H}_2 \uparrow$$

$$\text{Al(OH)}_3 + \text{NaOH} \rightleftharpoons \text{Na}^+ + [\text{Al(OH)}_4]^-$$
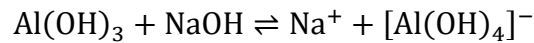
It has been shown in previous studies that the PVDF binder [101-103] and conductive additive [104-105] are not damaged and that the electrode active materials NMC [106-107] and LMO [108] are not corroded under the conditions applied during this process.

The 4-point probe setup consists of four equally spaced metal tips with finite radius making contact with the test subject along a line. The electric current is carried through the two outer probes and the voltage is recorded across the inner two probes. Valdes [109] considered seven different measurement cases and provided formulas and correction divisors to compute the resistivity based on geometrical considerations for each one. The samples in this study fall into case 7 analyzed by Valdes (after removal of the aluminum collector). Accordingly, the equation used to determine the effective electronic conductivity is given as:

$$V_{\text{test}} = \frac{1}{\sigma_{\text{eff}}} \left(\frac{\ln 2}{\pi L} \right) I_{\text{test}} \tag{4.14}$$

where I_{test}, V_{test} and L are the applied current, measured potential difference and electrode thickness, respectively. Once the voltage response to various applied currents was determined (Figure 4.4), the effective electronic conductivity was calculated by fitting Eqn. 4.14 to the data. It should also be noted that the applied current was small enough not to burn the porous electrode.
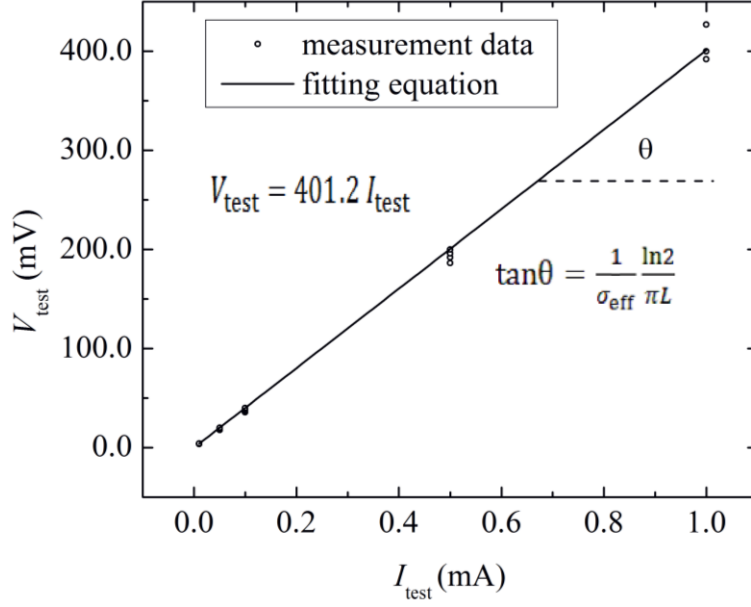
Figure 4.4: The measurement of effective electronic conductivity of the electrode.

The estimated value of the effective electronic conductivity (9.65 S m^{-1}) is within the range of conductivity values of various porous battery electrodes measured using a multi-probe method developed in Ref. [110].

The dimensional analysis of Ohm's law applied to porous electrodes reported in Ref. [97] yields the following simple equation for Φ_1 across the x-axis in a porous electrode:

$$\Phi_1 = \frac{IL}{\sigma_{\text{eff}}}\left(\frac{x^2}{2} - \frac{1}{6}\right) + \Phi_1^{\text{avg}} \tag{4.15}$$

where Φ_1^{avg} is the average solid-phase potential. Given that the parameters L and σ_{eff} have values of 57×10^{-6} m and $= 9.65$ S m^{-1}, respectively, the order of the first term is $O(10^{-6}I)$, while the second term Φ_1^{avg} is of order $O(1)$. Therefore, only at extremely high currents is the solid-phase potential non-uniform given the uniform conductive filler dispersion and the effective

68

conductivity estimated earlier. In other words, the value of such a large effective electronic conductivity has no significant impact on the electrode potential over the operating conditions of interest to this research. The effect of the electrode formulation and its microstructure on the effective conductivity is beyond the scope of this paper and will not be discussed here. The model parameters either measured or obtained from the literature are listed in Table 4.2.

4.4.4 Fitting of model to experimental potential-capacity curves

The six remaining model parameters with unknown values are the rate constants for charge transfer k_1 of NMC and k_2 of LMO, binary diffusion coefficient $\mathcal{D}_1$ of Li in NMC particles and binary diffusion coefficient $\mathcal{D}_2$ of Li in LMO particles and the mass fractions $\xi'_{1,1}$ and $\xi'_{1,2}$ of NMC particles in the submicron and micron groups, respectively, relative to the total mass of active material. Since the total mass fraction of NMC particles in both the submicron and micron groups is already known from our previous study to be 0.7, $\xi'_{1,1}$ and $\xi'_{1,2}$ are no longer independent of each other, i.e., $\xi'_{1,1} + \xi'_{1,2} = 0.7$. The five parameters are then adjusted to fit the model presented in the previous section to the complete set of experimental potential-capacity curves obtained at the rates C/25, C/10, C/5, C/2, 1C and 2C. The results are shown in Figure 4.5. Table 4.3 presents the values of $k_1, k_2, \mathcal{D}_1, \mathcal{D}_2, \xi'_{1,1}$ and $\xi'_{1,2}$ so obtained by this fitting procedure. As shown in Figure 4.5a, the agreement between the model-fitted and experimental curves is very good at all currents. A small discrepancy is observed at potentials close to 3.6V. This can be explained by the fact that the NMC equilibrium potential in the model is assumed to be the average value between the potentials obtained during a low-rate discharge and a low-rate charge

at each Li stoichiometry, as detailed before, and the hysteresis between the discharge and charge curves is largest at this potential.
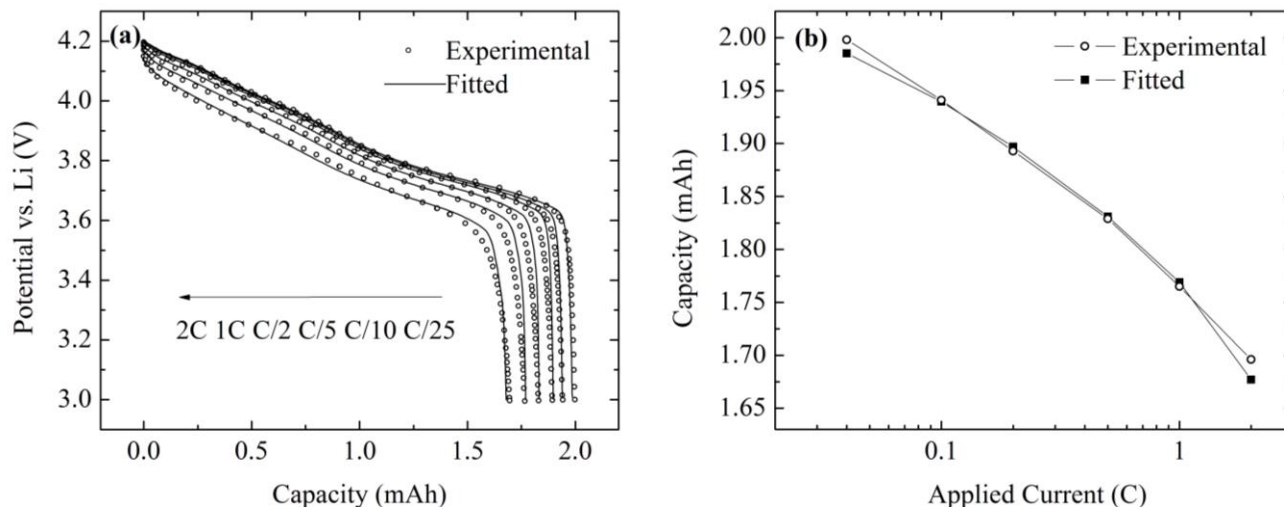
Figure 4.5: Comparison of the experimental and model-fitted (a) potential-capacity curves and (b) end-of-discharge capacity-current curves for discharge of a blended cathode with NMC: LMO composition of 0.7:0.3 by mass.

The dependence of the end-of-discharge capacity on the current for the NMC-LMO (70:30 wt%) blended cathode as determined experimentally and from the model is presented in Figure 4.5b. The capacities plotted in this case are obtained from Figure 4.5a and correspond to the values when the cell is in its discharged state at the lower cut-off potential of 3.0 V. Again, the model-fitted curve agrees very well with the experimental curve.

Table 4.3: List of model parameters.

Parameter	Symbol	LMO	NMC
Rate constant for charge transfer on type n cathode particle (mol/[m^{2}s(mol m^{-3})$^{1.5}$])	k_n	3×10^{-11}[f]	3×10^{-11}[f]
Binary diffusion coefficient of Li in type n particle (m^2 s^{-1})	$\mathcal{D}_n$	1.0×10^{-16}[f]	1.1×10^{-16}[f]
Mass fraction of type n particle among total active materials	$\xi'_{n,m}$	0.3[Chapter 3]	0.22[f] (micron group) 0.48[f] (submicron group)

f: fitted in the current study to the experimental potential-capacity data

In the following sensitivity analysis, the rate constants of the two active materials will be discussed when they are decreased or increased by one order of magnitude, i.e., from 3×10^{-12} to 5×10^{-10}. Our values for these two parameters lie within the reported values [73, 99, 111]. From the knowledge of the binary diffusion coefficients for Li (Table 4.3) and the dependence of the equilibrium potential $U_{n,m}$ on $y_{n,m}$, both the NMC and LMO chemical diffusion coefficients can be calculated using Eqns. (4.4) and (4.5) as functions of the local lithium concentration within active particles. A similar approach has been reported previously for other chemistries [35, 83, 97, 112-115]. The resulting values of the diffusion coefficients presented in Figure 4.6 vary from ~10^{-16} to ~10^{-15} m^{2}s^{-1} and from ~10^{-17} to ~10^{-16} m^{2}s^{-1} for NMC and LMO, respectively, and are well within the range of those estimated previously for these active materials by characterizing single-component electrodes. For instance, values in the ranges 10^{-16} to 10^{-14} (model) [19] and 10^{-18} to 10^{-17} m^{2}s^{-1} (PITT) [23] were obtained for NMC and LMO,

respectively. However, other values, such as 3.9×10^{-21} to 2.4×10^{-17} for NMC (EIS) [21] and 10^{-17} to 10^{-12} (CV, PSCA, EIS and model) [10-16, 116] for LMO, were found depending on the particle size, crystal defects in the samples and the measurement techniques used.
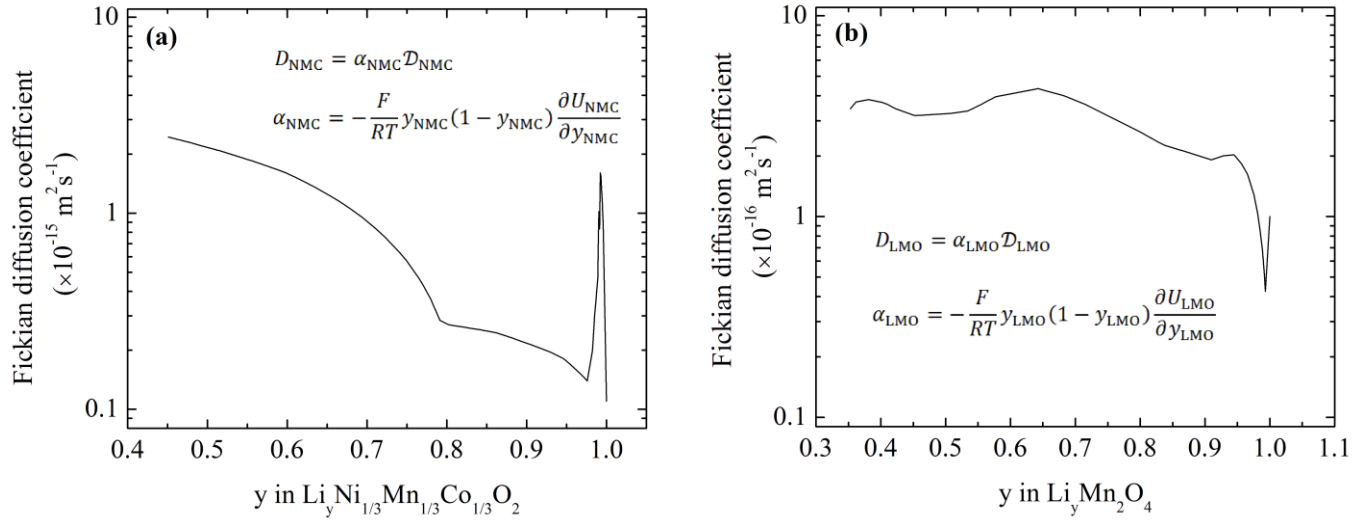
Figure 4.6: Calculated chemical diffusion coefficient of Li as a function of Li content during discharge of the single component (a) NMC and (b) LMO cathodes.

The differential-capacity curve is an intrinsic electrochemical signature for each active cathode material and so provides a good means for analyzing the contributions of each component to the electrode response over the course of lithiation or delithiation. In our previous section in chapter 3, the normalized differential capacity was used to successfully identify the active components in a blended cathode by matching the positions of three peaks for the same blended cathode, i.e., ~3.75V, ~4.00V and ~4.14V, with those obtained for single-component NMC and LMO cathodes (see Figure 3.2 of Chapter 3). The results showed that the first peak is associated with NMC, while the other two peaks are attributed to LMO. A comparison of the experimental and

simulated differential-capacity curves is presented in Figure 4.7. The determination of the differential-capacity curves essentially entails the numerical estimation of the tangents at many points along the potential-capacity curves. Consequently, the values so obtained are very sensitive to small changes and subtle details of the potential-capacity curves. A comparison of the experimental and computed curves in Figure 4.7 shows good agreement at all rates, most notably with regard to the peak positions. The good agreement between the measured and simulated curves gives confidence that the multi-particle model is able to accurately capture the contributions of NMC and LMO to the overall response at different rates.
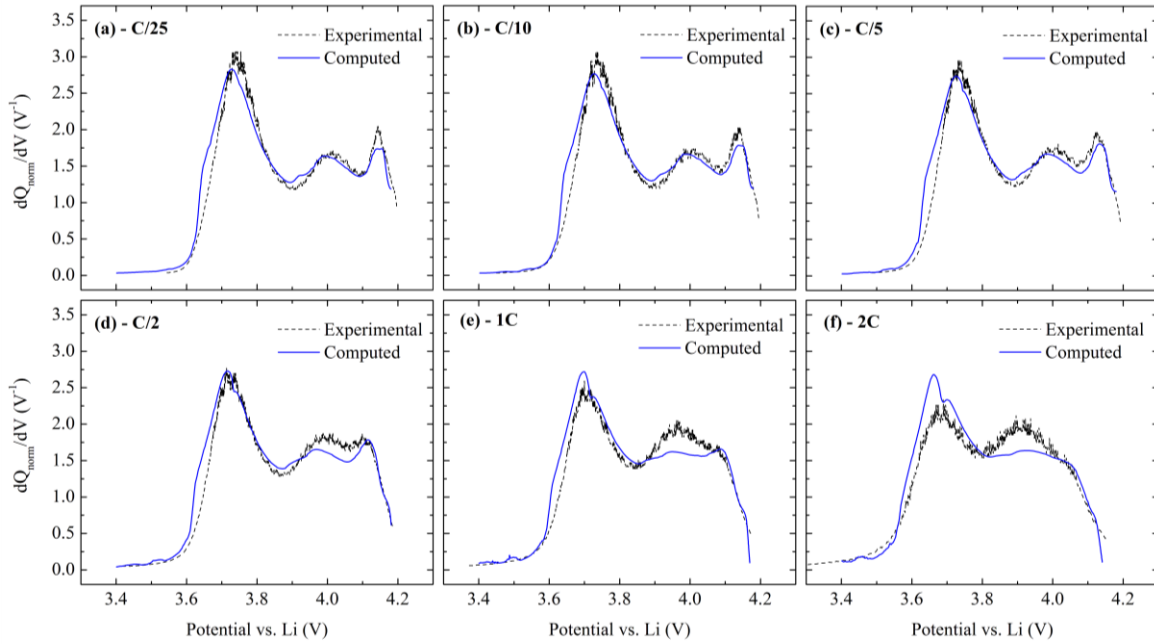
Figure 4.7: Experimental and computed differential-capacity curves of the NMC-LMO blended electrode at a C-rate of (a) C/25 (b) C/10 (c) C/5 (d) C/2 (e) 1C and (f) 2C.

The differential-capacity curves from C/25 to 2C exhibit either three (C/25, C/10, C/5 and C/2) or two (1C and 2C) peaks, reflecting that both NMC and LMO contribute to the discharge behavior at all rates. The peak positions in the differential-capacity curves continually shift toward lower potential as the C-rate increases. This trend is understandable given that the potential at any capacity during the discharge process would be expected to decrease (i.e., increase in overpotential) when the C-rate is raised (Figure 4.5a). In addition, the NMC signature peak appearing at the lowest potential decreases in magnitude, whereas the LMO signature peak at an intermediate potential increases in magnitude as the C-rate increases. At the same time, the other peak at high potential associated with LMO gradually shrinks and finally disappears altogether when the current reaches 2C.

The contributions of the total current and capacity of the blended cathode due to the LMO component at charge rates of C/25 and 2C over the course of the discharge, as computed according to the model, are presented in Figure 4.8a and 4.8b. Two maxima in the LMO contribution appear during the initial stages of discharge at low C-rate (Figure 4.8a). However, at high C-rate, only a single maximum in the current contribution of LMO is observed (Figure 4.8b), which coincides with the disappearance of one of the LMO differential-capacity peaks. The LMO component always contributes the higher proportion of the total current in the blended NMC-LMO cathode during the first half of discharge. The peak in the differential-capacity curves associated with LMO which occurs at higher potential (Figure 4.7) contributes more to the discharge current early in the overall cell discharge (Figure 4.8a and 4.8b) at lower rates (e.g., C/25) than at higher rates (e.g., 2C). As shown in Figure 4.8a and 4.8b, the LMO particles are

completely lithiated by the time the cell approaches the midpoint of the discharge process whereupon their contribution to the overall current sharply drops to zero.

Once the LMO capacity has been consumed, NMC begins to fully dominate the discharge current of the blended cathode. Throughout the second half of the discharge process, virtually all of the current involves the NMC particles. An inflection point is observed in the capacity contribution curves for NMC at both C/25 and 2C (Figure 4.8c and 4.8d) and coincides with the point where the LMO particles become largely spent.
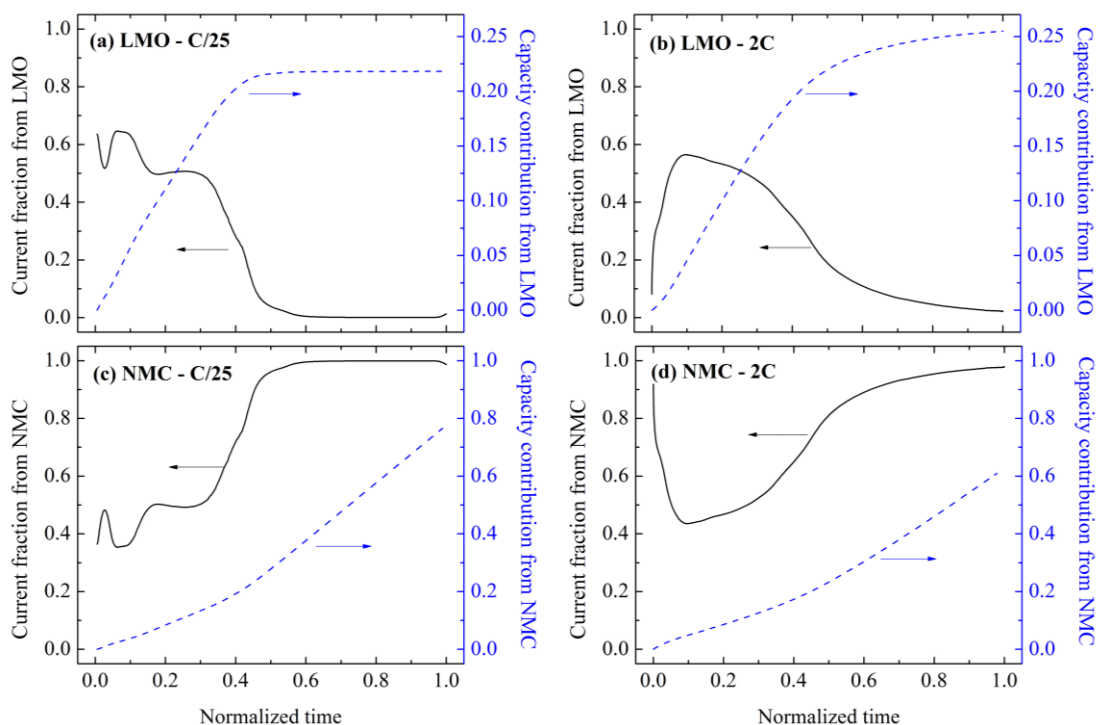
Figure 4.8: Variation in the total current and capacity of the blended cathode due to the LMO and NMC components with normalized time (i.e., with respect to the moment when simulations reach the lower cut-off potential of 3.0 V on discharge) over the course of a single discharge at rates of C/25 and 2C, i.e. (a) LMO-C/25 (b) LMO-2C (c) NMC-C/25 and (d) NMC-2C.

4.4.5 Sensitivity analysis

The sensitivity of the 5 fitted parameters reported in Table 4.3 and the effective electronic conductivity has been investigated by adjusting one parameter at the time while holding the others constant at their values listed in Table 4.2 and 4.3. The results are shown in Figure 4.9. The rate constants of the two active materials have almost no significant impact on the discharge curves at low C-rates (e.g., C/5); however, at high C-rates (e.g., 2C), the rate constant associated with NMC lithiation significantly affects the electrode potential and shifts the corresponding differential capacity peak towards lower potentials when it is decreased by one order of magnitude (Figure 4.9a). The rate constant of LMO lithiation affects the high-potential region of the potential-capacity curve and causes the associated peak in the differential capacity- potential curve to almost disappear when it is decreased by one order of magnitude (Figure 4.9b). The binary diffusion coefficient of NMC has a significant impact on the end-of-discharge capacity at both low and high C-rates; however, it does not affect the signature shape of the discharge curves as the differential-capacity curve remains almost unchanged regardless of the NMC binary diffusivity (Figure 4.9c). On the other hand, the binary diffusion coefficient of LMO has almost no impact on the end-of-discharge capacity regardless of the applied current but affects the high-potential differential-capacity peaks at 2C; the larger the diffusivity the greater the peaks intensities (Figure 4.9d). The end-of-discharge capacity is very sensitive to the size distribution of NMC particles (i.e., $\xi'_{NMC,2}$) both at low and at high applied currents (Figure 4.9e), while the differential-capacity curve is not affected by changes in the NMC particle-size distribution. Finally the effective electronic conductivity is not a sensitive parameter at least for the operating

76

currents of this study (Figure 4.9f), which is expected according to the dimensional analysis discussed earlier.

Overall, based on the sensitivity analyses of the 6 parameters, it is concluded that solid-state diffusion within NMC (i.e., both diffusion coefficient and particle-size distribution of the micron group) is the main limiting phenomenon during the discharge process. This is not surprising due to the fact that NMC contributes 70 wt% to the overall active material loading, one-third of which is in the form of large agglomerates (see Table 4.3).
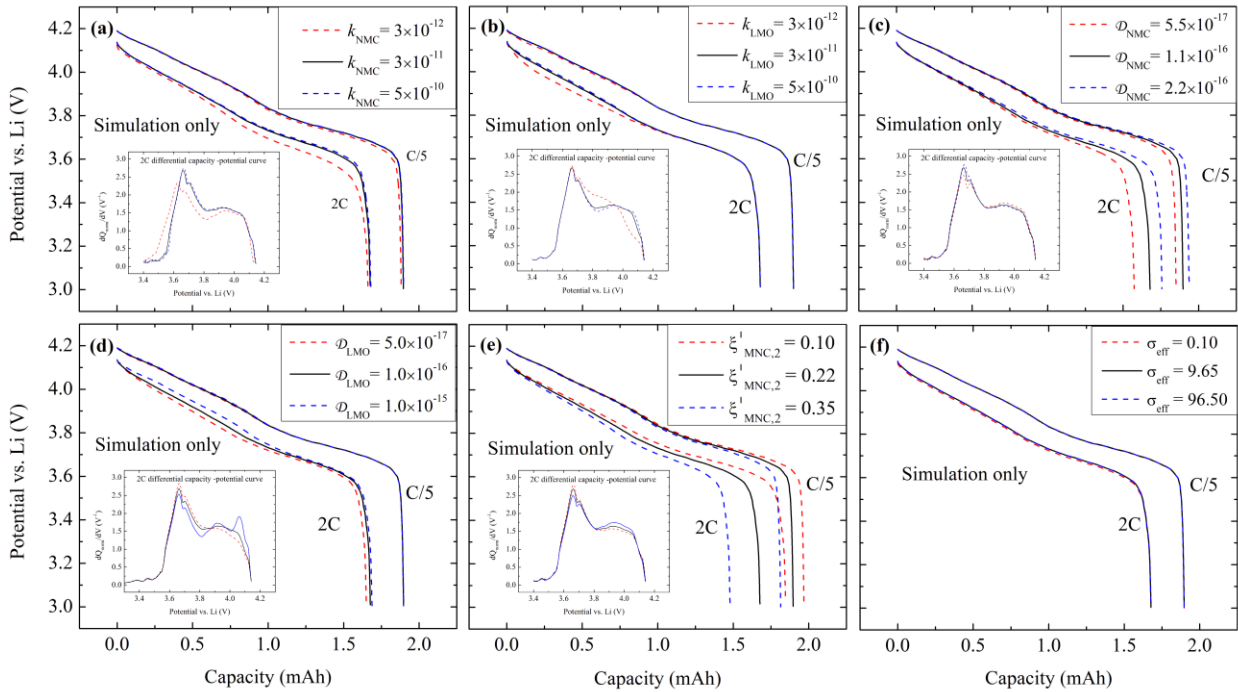
Figure 4.9: Multi-particle model sensitivity to (a) k_1 (mol $[m^2 s(mol \, m^{-3})^{1.5}]^{-1}$) (b) k_2(mol $[m^2 s(mol \, m^{-3})^{1.5}]^{-1}$) (c) $\mathcal{D}_1(m^2 s^{-1})$ (d) $\mathcal{D}_2$ $(m^2 s^{-1})$ (e) $\xi'_{NMC,2}$ and (f) σ_{eff} (S m^{-1}) at discharge rate of C/5 and 2C. 2C differential-capacity curves are shown in inset.

4.4.6 Particle-size effect

As discussed previously, the size of the NMC particles is best described in terms of two separate groups, the submicron group and the micron group, with distinct distributions. These two groups combine to yield the overall performance contribution due to NMC presented in Figure 4.8c and 4.8d. The breakdown of the contribution of NMC according to these two groups is plotted in Figure 4.10. The trends for the capacity contribution during discharge are similar for both groups; however, the submicron particles contribute much more to the current and capacity than do the micron particles. This result is not surprising since both diffusion and charge-transfer reaction limitations are smaller for the submicron particles than for the micron particles. Moreover, the cathode contains many more submicron NMC particles than micron particles (note their mass fractions in Table 4.3).
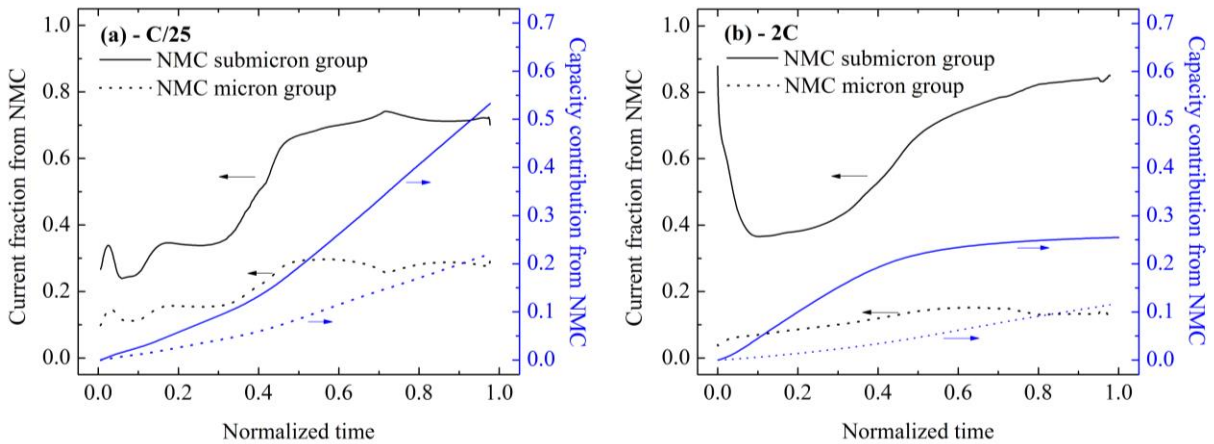
Figure 4.10: Variation of the fraction of the total current and capacity of the blended cathode due to the submicron and micron NMC groups with normalized time over the course of discharge at the rates of (a) C/25 and (b) 2C.

The utilization of active particles is defined as the ratio of the amount of lithium within the spherical particles [83] to the maximum amount based on c_n^{max} and can be calculated according to Eqn. 4.16:

$$\text{Utilization} = \frac{\int 4\pi r^2 c_{n,m}\, \mathrm{d}r}{c_n^{max}\, \frac{4\pi R_{n,m}^{3}}{3}} = 3 \int \left(\frac{c_{n,m}}{c_n^{max}}\right)\left(\frac{r}{R_{n,m}}\right)^2 \mathrm{d}\left(\frac{r}{R_{n,m}}\right)$$

$$= 3 \int y_{n,m} \left(r/R_{n,m}\right)^2 \mathrm{d}\left(r/R_{n,m}\right) \tag{4.16}$$

The value at the end of discharge is called the maximum utilization. A similar trend is evident upon examination of the effect of current on the maximum utilization of the LMO particles and the two groups of NMC particles as computed by the model and presented in Figure 4.11. The maximum utilization of the micron NMC particles drops from 0.95 to 0.65 with an increase in the discharge rate from C/25 to 2C. On the other hand, the maximum utilizations of both the LMO and submicron NMC particles remain above 0.97 at all C-rates, indicating that they contribute fully to the current and capacity until the lower cut-off potential is reached. The overall effect of the three classes of particles is that the total capacity of the blended cathode decreases as the discharge rate rises. Since the LMO and submicron NMC particles are considerably smaller than the micron NMC particles, these simulations once again emphasize that the size of NMC particles is a key factor affecting the total end-of-discharge capacity of the blended cathode.
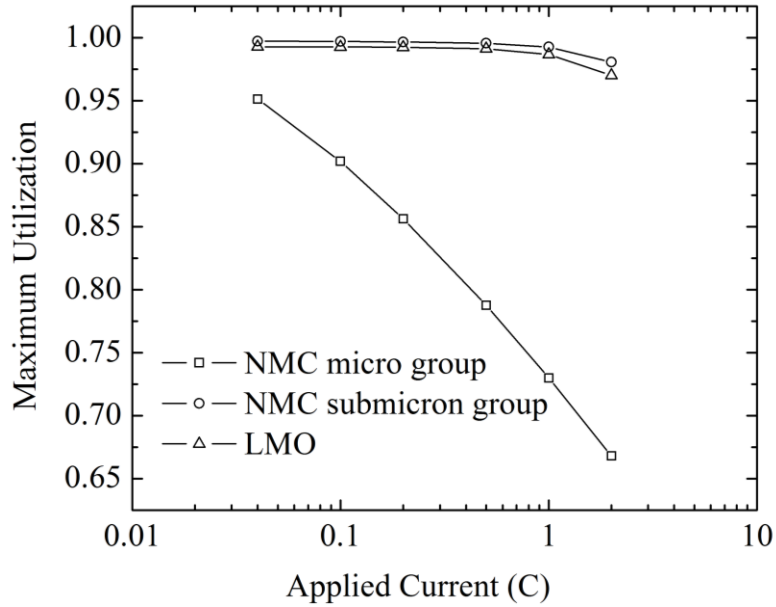
Figure 4.11: Effect of current on the maximum utilization of the LMO particles and the submicron and micron groups of NMC particles in the blended cathode.

To further investigate the effect of particle size, we use the model to compute the effect of current on the normalized end-of-discharge capacity of blended NMC: LMO cathodes with 70:30 wt% composition as determined at a potential of 3.0 V for the cases where the NMC particles are submicron only, micron only and submicron-micron mixtures obtained by end-of-discharge capacity as shows in Figure 4.5b (current case). As shown in Figure 4.12, if all NMC particles have the same submicron radius of 0.87μm, the cathode achieves the highest capacity at any C-rate due to its greater utilization. For example, at the highest C-rate of 2C, the capacity reaches a level approximately 15% higher than that attained if the NMC component is made up of a mixture of submicron-micron particles. However, if all NMC particles are in the micron group and have a radius of 4.65μm, the NMC utilization and the cathode capacity are dramatically lower; the capacity is 52% lower at a 2C charge rate than if all NMC particles are submicron.
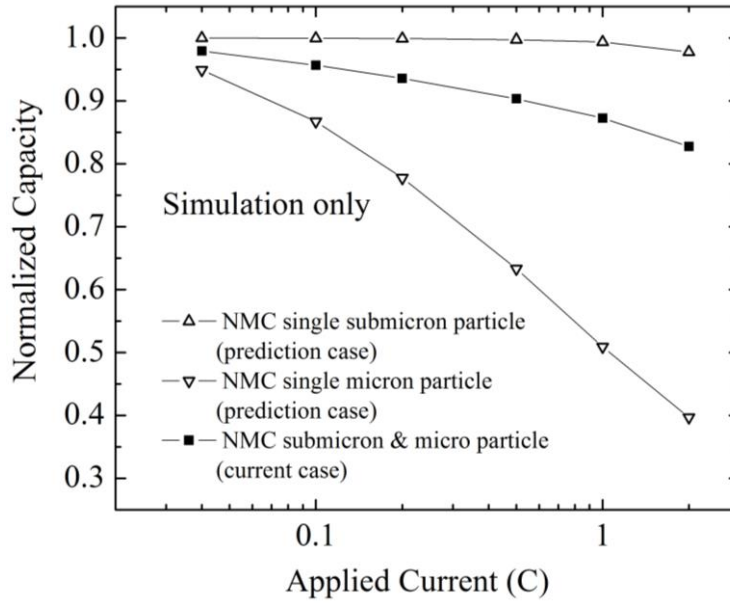
Figure 4.12: Effect of current on normalized capacity for electrodes composed of blended NMC and LMO with 70:30 wt% composition for the cases where the NMC particles are submicron only, micron only and 'blended' submicron-micron obtained by averaging according to the mass fraction of these two groups.

On the basis of the analysis above, it appears that reducing the amount of micron-sized particles and increasing the amount of submicron-sized particles in blended cathodes can effectively improve the utilization of NMC and further increase the cathode capacity, especially for discharge at high C-rates. During the material synthesis, a small and uniform primary-particle size is required to achieve a high material utilization. In addition, electrode manufacturing technology must be optimized to reduce active material particle agglomeration and clustering. Formation of secondary particles reduces ionic (i.e., through electrolyte) and electronic (i.e., through conductive matrix) access to the active sites. If the liquid-phase ionic percolation to the interior active sites in a porous secondary particle of a given size becomes less facile than the

solid-state diffusion in a hypothetical primary particle of the same size, then the latter dominates Li transport and the secondary particle behaves effectively as a large nonporous particle [93, 117-121]. Adequate fit of the model to the experimental data suggest that our assumption of nonporous secondary particles is in fact a plausible assumption that significantly reduces model complexity and computational cost. Future work could be to model the porous agglomerate to account for ionic and electronic losses across the porous secondary particles to further verify or reject our assumptions here. To be of practical value, such a complex model, however inclusive, requires accurate estimation of agglomerate parameters such as porosity and effective conductivity.

Chapter 5 Dynamics analysis for the blended cathode

The following section is based on the work 'Dynamics of a Blended Lithium-Ion Battery Electrode During Galvanostatic Intermittent Titration Technique' and 'Asymmetry in Dynamics of Charge/Discharge in a Blended Lithium-Ion Cathode' by Z. Mao et al. and the former is submitted to *Electrochimica Acta* and the latter is ready for submission. This thesis author specific contribution to this paper was to: develop the model, conduct the simulations and experiments, prepare all the graphics and results, and prepare the final manuscript and reviewer edits with direction from the project supervisors who were M. Fowler, Z. Chen and M. Pritzker. M. Farkhondeh offered advice on the modelling and the use of Galvanostatic Intermittent Titration Technique.

5.1 Introduction

Blended cathodes have been adopted within the growing electric vehicle market to further improve the electrode performance of lithium-ion batteries (LIB) for hybrid-electric vehicles (HEVs) and plug-in hybrid-electric vehicles (PHEVs) [74]. The blending of different crystalline structure materials such as layered-spinel mixtures $LiNi_xCo_yAl_{1-x-y}O_2$ -$LiMn_2O_4$ (NCA-LMO) [73, 80], $LiNi_xMn_yCo_{1-x-y}O_2$ -$LiMn_2O_4$ (NMC-LMO) [79]), layered-layered mixtures ($LiNi_xCo_yAl_{1-x-y}O_2$ - $LiCoO_2$ (NCA-LCO) [81]), layered-olivine mixtures ($LiCoO_2$-$LiFePO_4$ (LCO-LFP)[89]), spinel-olivine mixtures ($LiMn_2O_4$-$LiFePO_4$ (LMO-LFP) [90]) allows the best properties of the individual active materials to be combined to improve the energy or power density as well as the cycling and storage durability. If successful, the electrochemical

performance of blended cathodes would be expected to be superior to that of single material systems.

NMC-LMO blended systems for electric vehicle applications have been recently developed by several battery companies [74, 79]. Cathodes made of spinel LMO have a high operating potential and good rate capability while NMC cathodes have high capacity and good capacity retention. Therefore, a mixture of NMC and LMO yields an electrode with a balanced electrochemical performance in terms of specific capacity and working potential. However, LMO is plagued with fast capacity fade (poor cycle life) and low capacity retention after long-term storage at elevated temperatures. This behavior is mainly attributed to Mn dissolution and its reduction on the anode (e.g., graphite in a full LMO/graphite cell) [42, 46], which causes the interfacial contact resistance [42] and charge-transfer impedance at the interface between graphite and electrolyte [49] to rise and a coulombic imbalance to develop [50]. Fortunately, when LMO is mixed with NMC as a blended cathode, a synergistic interplay between the two materials is observed. The presence of NMC appears to suppress Mn dissolution and enable the blended cathode to exhibit cycling or storage performance that is often better than expected from a LMO electrode [50, 61-62].

The galvanostatic intermittent titration technique (GITT) is a very powerful electrochemical procedure that has been used to analyze the dynamics of electrode processes such as material phase formation, structural transitions or mass transport and estimate the corresponding parameters. A number of researchers have applied this method to study lithium-ion batteries. For example, Dees et al. [122] and Gowda et al. [123] investigated the polarization and relaxation behavior of lithium- and manganese-rich layered transition metal oxides to understand the

structural transitions that occur in the cathode. Gallagher et al. [124] used GITT to evaluate the rate constants for phase formation and consumption of lithiated graphite. Bach et al. [125] carried out GITT measurements to analyze the lithiation and delithiation mechanisms of a gold film serving as a lithium-ion battery anode. Birkl et al. [126] used GITT to determine the equilibrium potentials of NMC and graphite electrodes, while Wu et al. [19] estimated the lithium ion solid-state diffusion coefficient in an NMC electrode based on a physicochemical model. However, GITT analysis of a blended electrode to investigate the thermodynamics and dynamic processes during charge-discharge has still not been reported. This method is particularly well suited to investigate the effects of the different size fractions and chemical composition and the interaction between the active components of a blended electrode, as will be shown in this chapter.

Both the optimization of electrode design and fundamental analysis of the behavior of blended electrodes benefit from physics-based mathematical models which can simulate the electrode response to an electrochemical process. Moreover, these models are able to compute certain quantities that are not easily measured. However, only few mathematical models of blended cathode systems have been reported. Albertus et al. [73] presented a model to describe the influence of NCA-LMO blended cathode composition on the charge-discharge curves based on a distribution of contact resistances between the active material and the conductive matrix. Jung [79] developed a model of an NMC-LMO cathode and graphite-soft carbon anode to simulate and predict their performance.

In our previous section in chapter 4, we developed a pseudo-two-dimensional (P2D) multi-particle model of an NMC-LMO blended cathode that was able to accurately describe the effect

of the C-rate on the galvanostatic discharge and account for the effect of multiple particle sizes of the different active materials. In an earlier section (chapter 3), we showed that a simpler version of the model (i.e., no porous-electrode effects included) gave excellent fits to experimental potential-capacity and differential capacity-potential curves at low rates and could be used to accurately predict the composition of a blended cathode. In the current work, the multi-particle model is adapted to describe the potential response of the same NMC-LMO cathode to intermittent galvanostatic pulses in order to gain further insight into the kinetic and thermodynamic parameters of the system. In addition, the applicability of the multi-particle model to galvanostatic charge is examined. A particular focus of the GITT experiments in this study is to investigate the transport characteristics of intercalated species within the active materials under the conditions of a small-current or short-time electrochemical perturbation. On the basis of the model, it is possible to resolve the separate charge-discharge characteristics of the NMC and LMO components in the blended cathode during the relaxation period after a short discharge pulse. This analysis provides an explanation for some unique phenomena that occur within the blended cathode, such as the synergy between the two active materials.

Moreover, in the current chapter, the multi-particle model is used to examine the asymmetry between the galvanostatic charge and discharge processes in the NMC-LMO blended cathode operating at the different C-rates. Possible reasons for this asymmetry are analyzed using this multi-particle model.

5.2 Experimental

In this chapter, coin cells were fabricated from a fresh and unused commercial pouch cell containing blended NMC-LMO cathode sheets coated on both sides of an aluminum current collector. Only one of these cathode sheets was used to make the coin cells. The solvent N-methyl-2-pyrrolidone (NMP) was applied to the cathode sheet on one of the sides to dissolve away the binder and allow the remaining cathode material to be easily wiped away and discarded. Electrode discs with 0.712 cm^2 area were punched out of the NMC-LMO material remaining on the other side and then washed in dimethyl carbonate (DMC) to remove any salt deposited on their surface. Then, cathode|separator|Li coin cells were fabricated with a lithium foil as reference/counter electrode and Celgard 2500 as separator soaked in an electrolyte of 1 M LiPF$_6$ dissolved in a 1:1 (weight basis) EC/DMC solution. The entire process above was conducted in an argon-filled glove box.

These coin cells were subjected to a series of tests using a battery cycler (Neware CT-3008-5V10 mA-164-U) at the room temperature. In order to ensure that each cell had attained the same stable state at the start of the GITT experiment, it was subjected to 5 consecutive CCCC formation cycles between a lower cut-off potential of 3V and an upper potential of 4.2V. The specific experimental waveform of the cycling was described in our previous study (chapter 4). Following these 5 formation cycles, we subjected the coin cell to a GITT experiment. Each GITT experiment consisted of a sequence of 10 galvanostatic pulses at a given discharge current separated by a fixed relaxation period in which no current was applied. These pulses involved a discharge current of either 1C, C/2 or C/5 (corresponding to pulse widths of 6, 12 and 30 min, respectively) and an interval relaxation time of either 15 min or 2 h (1C rate corresponds to 1.38

mA of applied current). At each discharge current, GITT experiments were conducted at the two relaxation times in succession. A fresh coin cell was used for each of the three applied currents. This entire procedure was repeated a second time with a new set of fresh cells and found to yield very reproducible experimental data. Through a combination of each of these discharge currents and relaxation periods, six different GITT experiments were conducted. For example, the first GITT consisted of the following steps: i) charge at C/50 until a potential of 4.2 V was reached, ii) 2 h rest period, iii) discharge at 1C for 6 min, iv) 15 min rest period, v) repetition of steps iii) and iv) 9 times, vi) discharge at C/50 until a potential of 3.0V was reached and vii) 2 h rest period. The purpose of steps i) and vi) was to ensure the cell was fully lithiated at the start of the GITT experiment and fully delithiated at the end of each experiment. The applied current and duration time in step iii) and rest period in step iv) were changed for each GITT experiment, as discussed above. Moreover, the galvanostatic experiments on charging were carried out for applied currents: C/25, C/10, C/5, C/2, 1C and 2C, based on the experimental steps and coin-cell sets described in chapter 4.

5.3 Mathematical Model

To simulate the potential response of the NMC-LMO blended electrode to the intermittent galvanostatic pulses in the GITT experiments, the multi-particle mathematical model presented previously is implemented to describe the lithiation/delithiation dynamics at the particle and electrode scales [84, 96]. The defining feature of the multi-particle model lies in considering each of the two active electrode components NMC and LMO to have a non-uniform particle size distribution consistent with the actual physical and material characteristics (Figure 5.1). The model was verified in a previous study by successfully fitting it to experimental galvanostatic

discharge curves (chapter 4). The governing equations and corresponding boundary conditions at both the particle and electrode levels are shown in Table 5.1. The numerical values of the model parameters used are listed in Table 5.2. All equations and parameters were taken from chapter 5 without any change. The system of equations was solved using the COMSOL Mutiphysics 4.4 finite element software package.
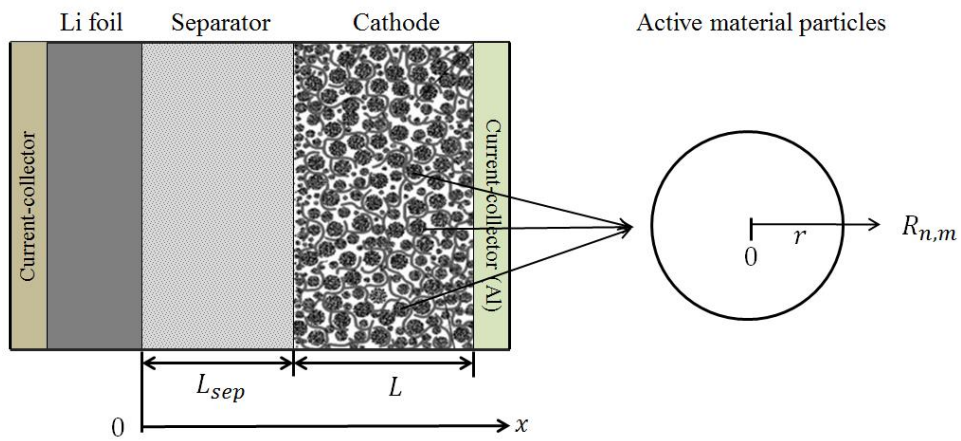
Figure 5.1: Schematic diagram showing the cell configuration used for the pseudo-two-dimensional multi-particle model of the NMC-LMO blended cathode.

Solid phase mass balance	Boundary conditions
$\dfrac{\partial c_{n,m}}{\partial t} = \dfrac{1}{r^2}\dfrac{\partial}{\partial r}\left(D_{n,m}r^2\dfrac{\partial c_{n,m}}{\partial r}\right)$	
$D_{n,m} = \alpha_{n,m}\mathcal{D}_n$	
$\alpha_{n,m} = -\dfrac{F}{RT}y_{n,m}(1-y_{n,m})\dfrac{\partial U_{n,m}}{\partial y_{n,m}}$	$\dfrac{\partial c_{n,m}}{\partial r} = 0$ at $r = 0$
$i_{n,m} = i_{n,m}^0\left[\exp\left(\dfrac{(1-\beta_n)F}{RT}\eta_{n,m}\right) - \exp\left(-\dfrac{\beta_n F}{RT}\eta_{n,m}\right)\right]$	$\dfrac{\partial c_{n,m}}{\partial r} = -\dfrac{i_{n,m}}{FD_{n,m}}$ at $r = R_{n,m}$
$i_{n,m}^0 = Fk_n(c_e)^{(1-\beta_n)}(c_{s,n,m})^{\beta_n}(c_n^{max} - c_{s,n,m})^{\beta_n}$	
$\eta_{n,m} = \Phi_1 - \Phi_2 - U_{n,m}(y_{n,m})$	
$y_{n,m} = \dfrac{c_{n,m}}{c_n^{max}}$	

Electrode-level equations

Solid phase charge balance	Boundary conditions
$\mathbf{i}_1 = -\sigma_{\text{eff}}\nabla\Phi_1$	
$\nabla\cdot\mathbf{i}_1 = -\xi\displaystyle\sum_{n=1}^{N}\sum_{m=1}^{M}\xi_{n,m}a_{n,m}i_{n,m}$	
$\displaystyle\sum_{n=1}^{N}\sum_{m=1}^{M}\xi_{n,m} = 1$	$\mathbf{i}_1 = 0$ at $x = L_{\text{sep}}$
	$\mathbf{i}_1 = I/A$ at $x = L_{\text{sep}} + L$
$\xi_{n,m} = \dfrac{\xi'_{n,m}/\rho_n}{\sum_{n=1}^{N}\left(\sum_{m=1}^{M}\xi'_{n,m}/\rho_n\right)}$	
$a_{n,m} = \dfrac{3}{R_{n,m}}$	
$E = \Phi_1|_{x=L_{\text{sep}}+L} - \Phi_{\text{f}}$	

Liquid phase charge balance	Boundary conditions
$\nabla\cdot\mathbf{i}_2 = 0$	$\Phi_2 = 0$ at $x = 0$
$\mathbf{i}_2 = -\kappa_{\text{eff,sep}}\nabla\Phi_2 + \dfrac{2\kappa_{\text{eff,sep}}RT(1-t_+^0)}{Fc_e}\left(1+\dfrac{d\ln f_\pm}{d\ln c_e}\right)\nabla c_e$	$\mathbf{i}_2|_{\text{sep}} = \mathbf{i}_2|_{\text{cat}}$ at $x = L_{\text{sep}}$
$\kappa_{\text{eff,sep}} = \kappa\varepsilon_{\text{sep}}^\gamma$	
$\nabla\cdot(\mathbf{i}_1 + \mathbf{i}_2) = 0$	$\mathbf{i}_2|_{\text{sep}} = \mathbf{i}_2|_{\text{cat}}$ at $x = L_{\text{sep}}$

$$\mathbf{i}_2 = -\kappa_{\text{eff,cat}}\nabla\Phi_2 + \frac{2\kappa_{\text{eff,cat}}RT(1-t_+^0)}{Fc_e}\left(1 + \frac{d\ln f_\pm}{d\ln c_e}\right)\nabla c_e \qquad \mathbf{i}_2 = 0 \text{ at } x = L_{\text{sep}} + L$$

$$\kappa_{\text{eff,cat}} = \kappa\varepsilon_{\text{cat}}^\gamma$$

<table>
<tr><td align="center">Electrolyte mass balance</td><td align="center">Boundary conditions</td></tr>
</table>

$$\varepsilon_{\text{sep}}\frac{\partial c_e}{\partial t} = \nabla\cdot\left(\varepsilon_{\text{sep}}D_{\text{eff,sep}}\nabla c_e\right) - \frac{\mathbf{i}_2\nabla t_+^0}{F} \qquad \varepsilon_{\text{sep}}\frac{\partial c_e}{\partial x} = -\frac{I(1-t_+^0)}{FD_{\text{eff,sep}}A} \text{ at } x = 0$$

$$D_{\text{eff,sep}} = D_e\varepsilon_{\text{sep}}^{\gamma-1} \qquad \frac{\partial c_e}{\partial x}\Big|_{\text{sep}} = \frac{\partial c_e}{\partial x}\Big|_{\text{cat}} \text{ at } x = L_{\text{sep}}$$

$$\varepsilon_{\text{cat}}\frac{\partial c_e}{\partial t} = \nabla\cdot\left(\varepsilon_{\text{cat}}D_{\text{eff,cat}}\nabla c_e\right) - \frac{\mathbf{i}_2\nabla t_+^0}{F} + \frac{(1-t_+^0)\xi\sum_{n=1}^N\sum_{m=1}^M\xi_{n,m}a_{n,m}i_{n,m}}{F} \qquad \frac{\partial c_e}{\partial x}\Big|_{\text{sep}} = \frac{\partial c_e}{\partial x}\Big|_{\text{cat}} \text{ at } x = L_{\text{sep}}$$

$$D_{\text{eff,cat}} = D_e\varepsilon_{\text{cat}}^{\gamma-1} \qquad \frac{\partial c_e}{\partial x} = 0 \text{ at } x = L_{\text{sep}} + L$$

$$D_e = \frac{c_{\text{T}}}{c_0}\left(1 + \frac{d\ln f_\pm}{d\ln c_e}\right)\mathcal{D}_e$$

<table>
<tr><td align="center">Lithium counter electrode kinetics</td></tr>
</table>

$$I = -Ai_f^0\left[\exp\left(\frac{(1-\beta_f)F}{RT}(\Phi_f - \Phi_2)\right) - \exp\left(-\frac{\beta_f F}{RT}(\Phi_f - \Phi_2)\right)\right]$$

<table>
<tr><td align="center">Equilibrium potential</td></tr>
</table>

$$U_{\text{NMC}}(y_{\text{NMC}}) = 6.51176 - 8y_{\text{NMC}} + 7.1086y_{\text{NMC}}^2 - 1.55y_{\text{NMC}}^3 - 0.459y_{\text{NMC}}^6 - 5.00034$$
$$\times 10^8 \exp(135.089y_{\text{NMC}}^2 - 118.089)$$

$$U_{\text{LMO}}(y_{\text{LMO}}) = 0.225 - 0.392y_{\text{LMO}} + 2.2\tanh[-1010(y_{\text{LMO}} - 0.994)] + 1.9\tanh[-21.4(y_{\text{LMO}} - 1.04)]$$
$$+ 0.181\,\text{sech}[23.4(y_{\text{LMO}} - 0.397)] - 0.175\text{sech}[24.2(y_{\text{LMO}} - 0.399)]$$
$$+ 0.0164\,\text{sech}[13.1(y_{\text{LMO}} - 0.567)] + 0.33\,\text{sech}[48.1(y_{\text{LMO}} - 1)]$$

Table 5.2: List of model parameters.

Parameter	Symbol	LMO	NMC
Cathode area (cm^2)	A	1.103/0.712[m]	
Electrode thickness (m)	L	5.7×10^{-5} [m]	
Cathode capacity (Ah)	Q	0.002 [m]	
Total active-material volume fraction	ξ	0.558 [Chapter 3]	
Radius of type n particle in size class m (m)	$R_{n,m}$	8.7×10^{-7} [m]	4.65×10^{-6} [m] (micron group) 4.35×10^{-7} [m] (submicron group)
Mass fraction of type n particle among total active materials	$\xi'_{n,m}$	0.3 [Chapter 3]	0.22 [Chapter 4] (micron group) 0.48 [Chapter 4] (submicron group)
Rate constant for charge transfer on type n cathode particle (mol/[m^{2}s(mol m^{-3})$^{1.5}$])	k_n	3×10^{-11} [Chapter 4]	3×10^{-11} [Chapter 4]
Binary diffusion coefficient of Li in type n particle (m^2 s^{-1})	$\mathcal{D}_n$	1.0×10^{-16} [Chapter 4]	1.1×10^{-16} [Chapter 4]
Capacity of type n particle (Ah kg^{-1})	q_n	100 [73]	151 [19]
Maximum lithium concentration in type n particle (mol m^{-3})	c_n^{max}	23339 [73]	49761 [19]

Description	Symbol		
Density of type n particle (kg m^{-3})	ρ_n	4220 [Chapter 3]	4770 [Chapter 3]
Charge-transfer coefficient for charge transfer on type n cathode particle	β_n	0.5 [Chapter 3]	0.5 [Chapter 4]
Electrode porosity	ε_{cat}	0.35 [Chapter 3]	
Initial electrolyte concentration (mol m^{-3})	c_e	1000 [m]	
Separator thickness (m)	L_{sep}	2.5×10^{-5} [Celgard]	
Lithium ions transference number	t_+^0	0.36 [Chapter 4]	
Bulk diffusion coefficient in the electrolyte (m^2 s^{-1})	$\mathcal{D}_e$	5.2×10^{-10} [83]	
Bulk ionic conductivity of the electrolyte (S m^{-1})	κ	1.3 [83]	
Charge-transfer coefficient for charge transfer on Li foil electrode	β_f	0.5 [Chapter 4]	
Separator porosity	ε_{sep}	0.55 [Celgard]	
Bruggeman exponent	γ	1.5 [Chapter 4]	
Effective electronic conductivity (S m^{-1})	σ_{eff}	10.10 [m]	
Exchange current density on Li foil electrode (A m^{-2})	i_f^0	20 [Chapter 4]	
Faraday constant (C mol^{-1})	F	96478	
Gas constant (J mol^{-1} K^{-1})	R	8.314	
Temperature (K)	T	298	

[m]: measured

[Celgard]: Celgard product data sheet

5.4 Results and Discussions

5.4.1 Comparison of model simulations to experimental discharge GITT responses
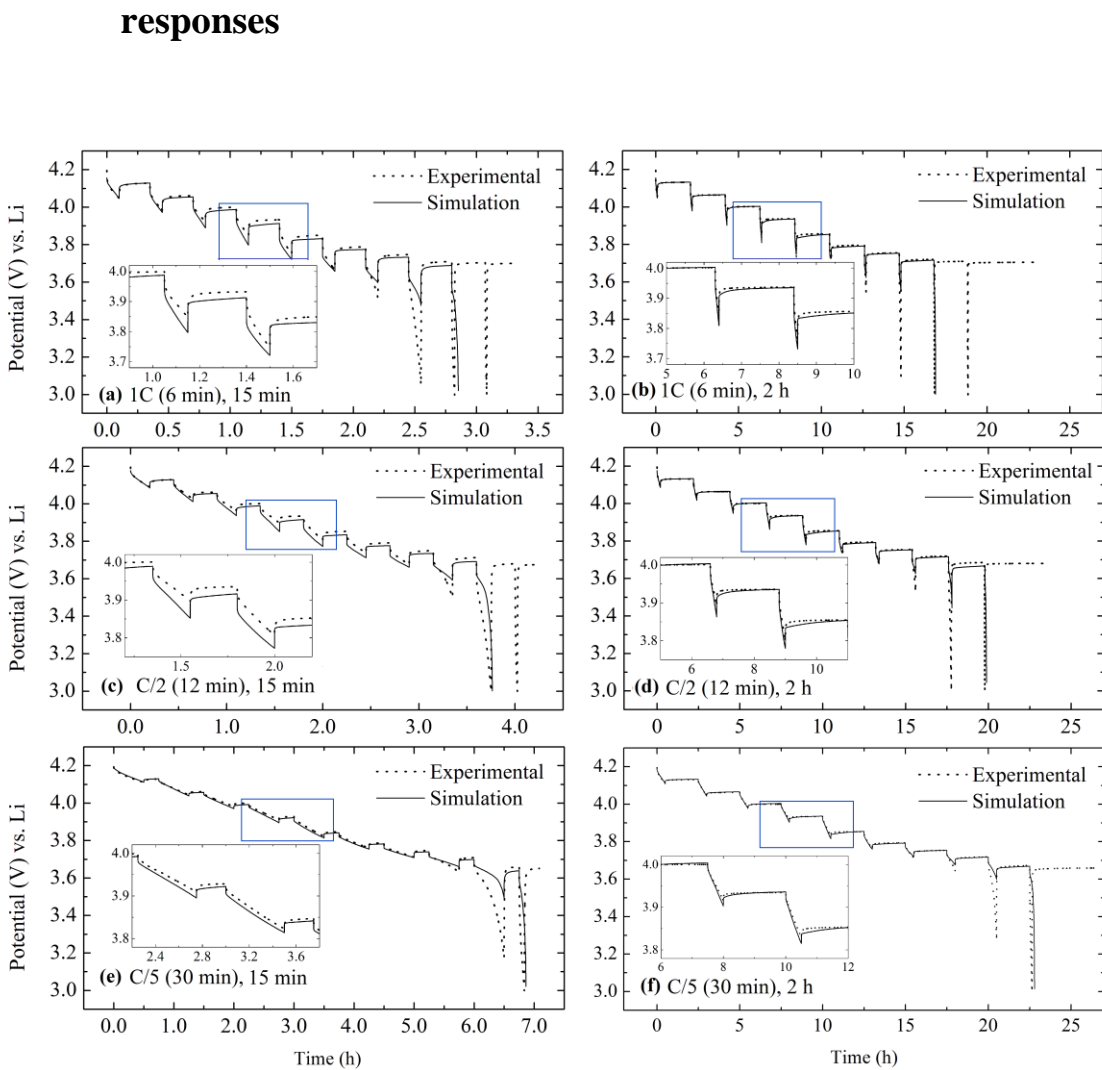
Figure 5.2: Comparison of the experimental and simulated responses to the GITT pulses consisting of the following discharge currents and rest intervals: (a) 1 C (6 min), 15 min (b) 1 C (6 min), 2 h (c) C/2 (12 min), 15 min (d) C/2 (12 min), 2 h (e) C/5 (30 min), 15 min rest (f) C/5 (30 min), 2 h.

As shown by the experimental and simulated responses in Figure 5.2, the multi-particle model gives excellent predictions of the GITT curves in an NMC-LMO blended cathode over a wide range of discharge rates (1C, C/2 and C/5), pulse durations (6 min, 12 min and 30 min) and interval relaxation periods (15 min and 2 h). At the higher C-rates of 1C and C/2 and a relaxation period of 15 min (Figure 5.2a and 5.2c), the simulated potential evolution during each of the middle four or five discharge pulses is slightly steeper than that actually measured. However, in the case of the smaller current of C/5 (Figure 5.2e), the simulated potential remains very close to the experimental value over the majority of the GITT experiment. Moreover, the potential drop which becomes progressively smaller with each successive pulse is accurately tracked by the model. A comparison of the responses in Figure 5.2a, 5.2c, 5.2e to Figures 5.2b, 5.2d, 5.2f enables the effect of the length of the relaxation period (15 min to 2 hours) following each current pulse to be discerned for both the simulated and experimental responses. This analysis shows that the model becomes more accurate when the relaxation time after the discharge pulse is extended from 15 min to 2 h. This suggests that the model is more effective for those experiments with a long enough relaxation period for the system to return more closely to its equilibrium state.

It should be acknowledged that the model does not capture the observed behavior as well during the last two or three pulses in each of the experiments. When the cell is almost fully discharged, its measured potential tends to drop very rapidly, making it difficult for the simulations to closely track it. Also, in several cases, the simulation terminated early since the potential reached the lower cut-off value of 3.0 V (Figure 5.2a, 5.2b and 5.2c). On the basis of the cases shown in Figure 5.2, the model is most accurate for GITT discharge at lower rates (i.e., C/5, 30 min

discharge time) with longer relaxation periods (i.e., 2 h) (Figure 5.2f). Consequently, we restrict ourselves to these conditions in the subsequent analysis of the model to explore other aspects of the dynamics of the blended electrode during intermittent operation.

The multi-particle model permits the contributions of the two active materials (LMO and NMC) to the internal dynamics of the blended cathode to be determined over the ten C/5 discharge pulses of the GITT experiment shown in Figure 5.3, each of which is followed by 2 h relaxation. The LMO component contributes a higher proportion of the overall current than NMC during the first three pulses. Also, the LMO contribution over the first five pulses or the first half of the GITT process (Figure 5.3a) is similar to that obtained in our previous galvanostatic discharge experiment (chapter 4). When the operation of the cell is shifted into the relaxation phase after the discharge pulses, the currents due to both NMC and LMO do not immediately decrease to zero. In fact, the currents have not yet reached zero by the end of each of the 2 h relaxation periods that follow the first five pulses (Figure 5.3b). Obviously, the current generated by LMO is always opposite in sign and exactly cancelled by the current generated by NMC during the relaxation periods. In order to examine the dynamics of this process in more detail, the responses of two current pulses marked PULSE 1 and PULSE 2 in Figure 5.3a (magnified in Figure 5.4) are examined. PULSE 1 shows the response during the 1st pulse applied during the GITT experiment, whereas PULSE 2 corresponds to the 5th pulse in the sequence of ten. Throughout the 30 min of discharge during PULSE 1, more current flows through LMO than through NMC (Figure 5.4a). Once the current is turned off at the start of the relaxation period, the NMC current changes instantaneously in the negative direction and then becomes positive again relatively soon afterward (Figure 5.4a, 5.4b). LMO continues to be discharged (i.e., positive current), albeit

at a decreasing rate, over the time period marked by points A and B, while NMC is now being charged (i.e., negative current). This signifies that lithium is being transferred from NMC to LMO within the cathode over this relatively short time period. The preferential discharge of LMO over that of NMC is consistent with the finding above that most of the discharge current during the first few pulses flows through LMO. This trend continues until point B is reached, whereupon the LMO and NMC currents both pass through zero and a crossover occurs. At this crossover point, the electrode is not stabilized although the current flowing through component is zero. Thereafter, NMC is discharged and LMO is charged over the remainder of the relaxation period. Over this last portion of the relaxation period, the magnitudes of both currents first rise to a maximum and then gradually decrease back toward zero.
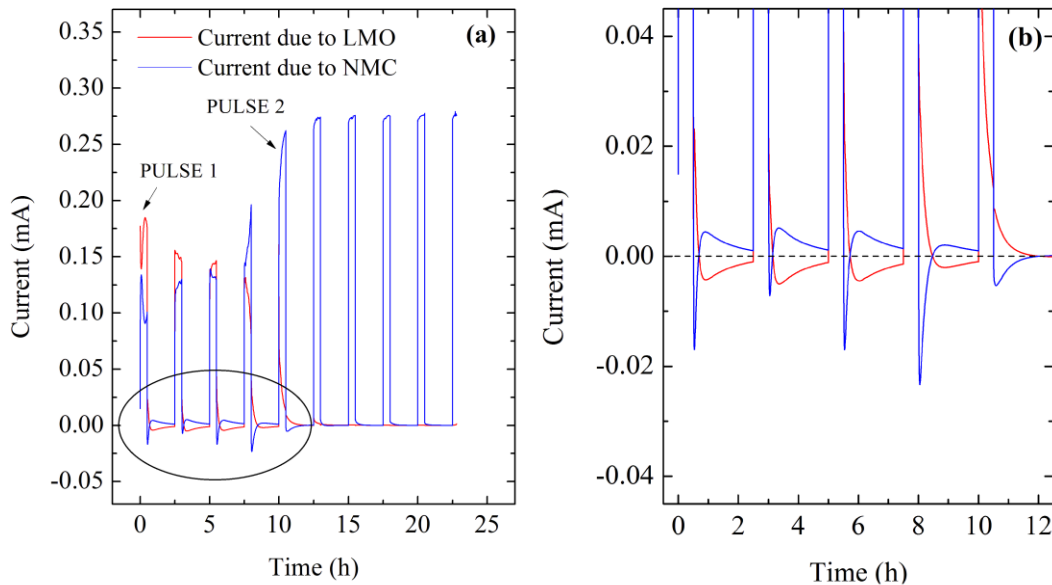
Figure 5.3: (a) Variation of the LMO and NMC currents with time over the course of the ten GITT discharge pulses conducted at C/5 (30 min) followed by 2 h relaxation. The circled region in (a) is shown at higher resolution in (b).

Since PULSE 2 occurs midway through the GITT, LMO has reached close to a fully lithiated state, whereas NMC has not (Figure 4.8 in chapter 4) when this pulse begins. Not surprisingly, the LMO current is much lower than the NMC current during the 30 min discharge period of PULSE 2, as shown in Figure 5.4c. The subsequent charge-discharge behavior during the segments DE and EF of the relaxation period (Figure 5.4d) follows the same trend as that during the segments AB and BC, respectively, that follow PULSE 1 (Figure 5.4b), i.e., first discharge and then charge of LMO and the opposite for NMC. The main difference between the electrode dynamics during the relaxation periods of PULSE 1 and PULSE 2 is the change of current and the relative length of time in which LMO and NMC are discharged and charged, which is associated with the degree of lithiation of LMO and NMC. Since LMO is much more fully lithiated by the time PULSE 2 starts, the change in discharge current is relatively small and the first charge-discharge period DE takes more time than the corresponding segment AB in PULSE 1.
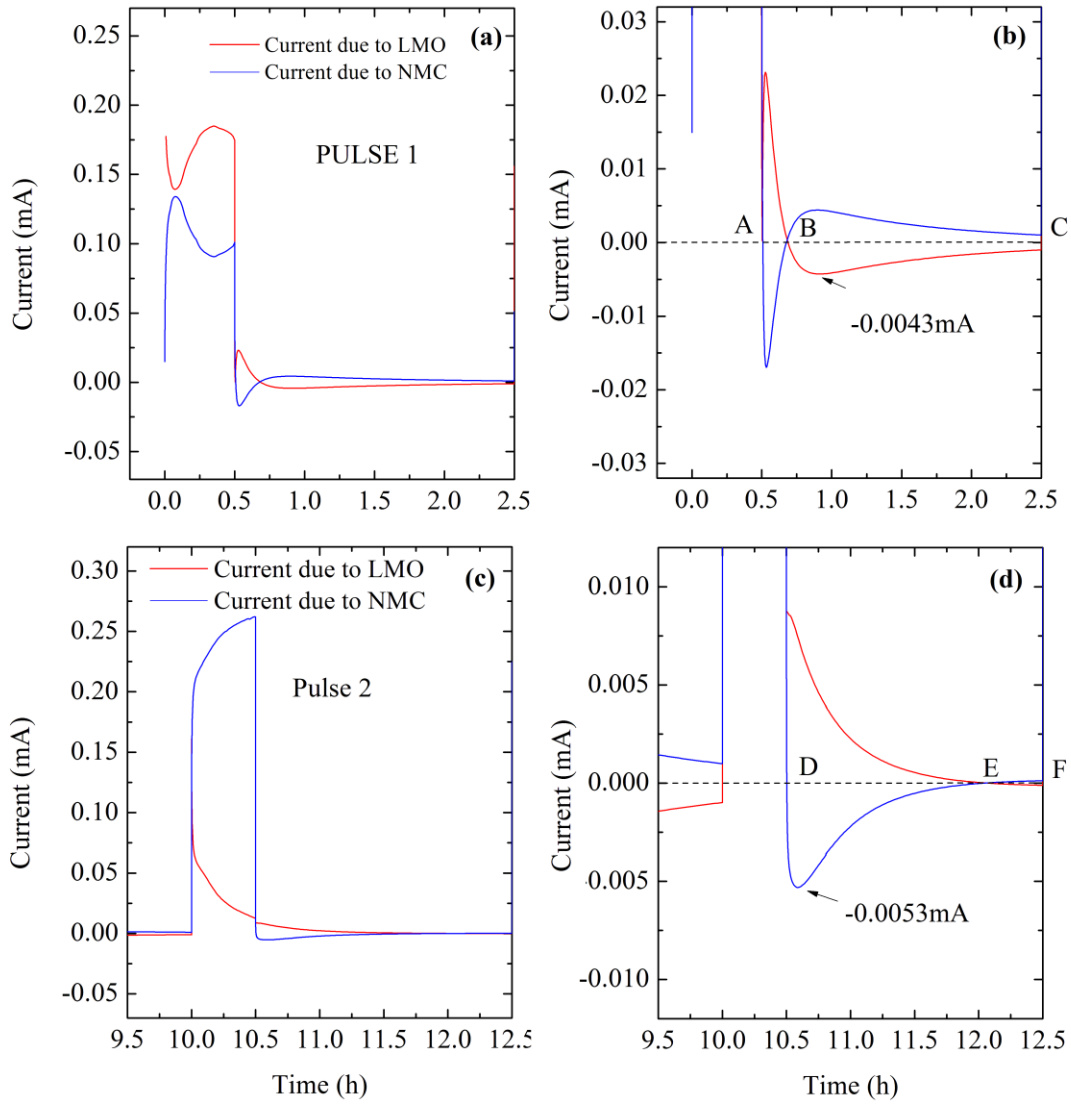
Figure 5.4: (a) Variation of the LMO and NMC currents with time for (a) PULSE 1 and (c) PULSE 2. The circled regions in (a) and (c) are shown at higher resolution in (b) and (d), respectively.

As found in our previous section in chapter 4, the particle sizes of the NMC component in this commercial blended cathode can best be described in terms of two separate particle size

99

distributions (PSDs) − a submicron group with d_{50} of 0.87 µm and a micron group with d_{50} of 9.29 µm. Therefore, the overall current due to NMC can be broken down into contributions from these two size groups. Figure 5.5 presents the breakdown of the current contributed from these two groups over the course of the same GITT experiment shown in Figure 5.3 and 5.4.

Figure 5.5a shows that the current due to the NMC submicron particles far exceeds that of the NMC micron particles throughout all 30 min of each discharge pulse during the GITT experiment. During each of the following 2h relaxation periods, the submicron particles are always charging while the micron particles are discharging, albeit at ever diminishing rates with each pulse. This behaviour is clearly evident during PULSE 1 and 2 (Figure 5.5b and 5c). In the absence of an external current, the losses associated with reaction kinetics at the surface and species transport within the active particles diminish. The electrode dynamics which is controlled by an external current during the on-time is now determined by the deviation of the active particle equilibirum potentials $U_{n,m}(y_{s,nm})$ from a "common potential" throughout the electrode during the relaxation period. The smaller "over-lithiated" NMC submicron particles with a lower surface equilibrium potential give away a fraction of their content to the larger "under-lithiated"micron-sized NMC particles with a higher equilibirum potential to compensate the lithiation lag during the on-time. Since the two particles have the same chemical nature, they must have identical Li concentrations at their surfaces in order to reach a common equilibirum potential. On the other hand, the concentration gradient within each particle is expected to disappear during the relaxation period depending on its initial value, particle size and solid-state chemical diffusion coefficient. As a result, the relaxation dynamics at the particle level involves two distinct mechanisms simultaneously: i) intra-particle relaxation of the concentration gradient

100

toward a flatter profile over time and ii) inter-particle exchange of lithium to reach a common

equilibrium potential at the surfaces of the two types of NMC particles. Given enough relaxation

time, the final concentration of Li is expected to be identical in the submicron- and micron-sized

NMC particles. Similar effects should operate between NMC and LMO particles except for the

fact that the lithium contents of the two types of active materials are not identical at equilibrium

state but determined in accordance with the individual equilibirum potential curve of each

material.
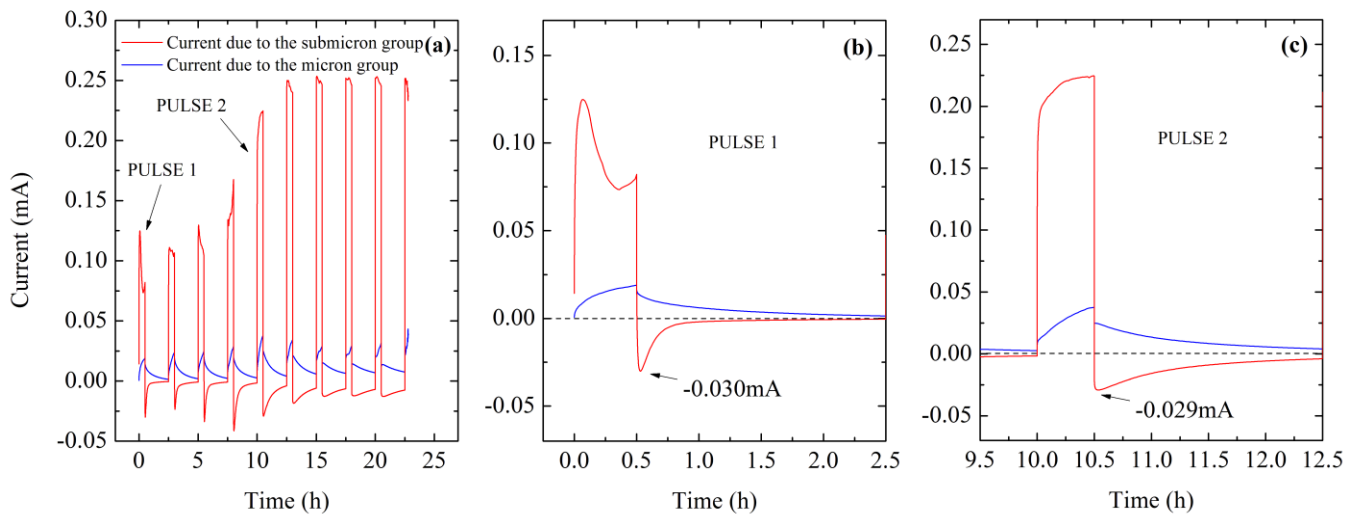
Figure 5.5: (a) Current contributions of the NMC submicron and micron groups over the course

of the same GITT experiment presented in Figure 5.3 and 4. Magnified views of current

contributions during PULSE 1 and PULSE 2 are shown in (b) and (c), respectively.

The variation of lithium stoichiometry at the surface of each particle group over the ten pulses in

the blended cathode simulated by the model is presented in Figure 5.6a. The responses during

PULSE 1 and PULSE 2 are shown at a higher resolution in Figure 5.6c and 5.6d, respectively,

including the same segments AB, BC, DE and EF defined in Figure 5.4b and 5.4d. The maximum lithium concentration is always reached on the surfaces of both LMO and NMC submicron particles by the end of each discharge pulse. However, over the subsequent relaxation period, the surface concentration decreases gradually until the beginning of the next discharge pulse. The relaxation of the surface concentration is smaller (less than 10% for LMO and 5% for NMC comparing concentrations at the beginning and end of relaxation), indicating the relatively weak driving forces in effect for both inter- and intra-particle relaxation. On the other hand, the lithium concentration remains almost constant at the surface of the NMC micron particles during the first few relaxation periods, but then eventually begins to rise during the later relaxation periods. In addition, the lithium stoichiometry at the surface of the LMO particles reaches close to 1.0 after 5 or 6 discharge pulses which is close to the midpoint of the entire GITT experiment. Interestingly, the lithium stoichiometry at the surface also reaches close to 1.0 midway through the continuous galvanostatic discharge of the blended cathode at the same rate of C/5 (Figure 5.6b). The electrode dynamics in the first half of the GITT and continuous discharge experiments is mostly dominated by LMO lithiation. As a result, LMO becomes fully lithiated prior to and faster than NMC due to thermodynamic reasons (i.e., a higher equilibrium potential of LMO compared to NMC, as seen in Figure 3.3 in chapter 3. During the second half of the GITT experiment, however, NMC submicron and micron particles carry most of the Li flux during the current pulse and exchange matter mostly with each other (i.e., little interaction with LMO) during relaxation (Figure 5.6a and 5.6d). Unlike the first half of the GITT experiment, NMC particles do not completely reach an equilibrium state (i.e., identical surface concentration) in the second half of the experiment although the deviation from a final equilibrium state is very small

102

(i.e., only less than 3%). Overall, analysis of the surface concentrations confirms that the lithium lost from the surfaces of the LMO and NMC submicron particles either diffuses into the interior of these particles or to the NMC micron particles, which is consistent with the results shown in Figure 5.5.
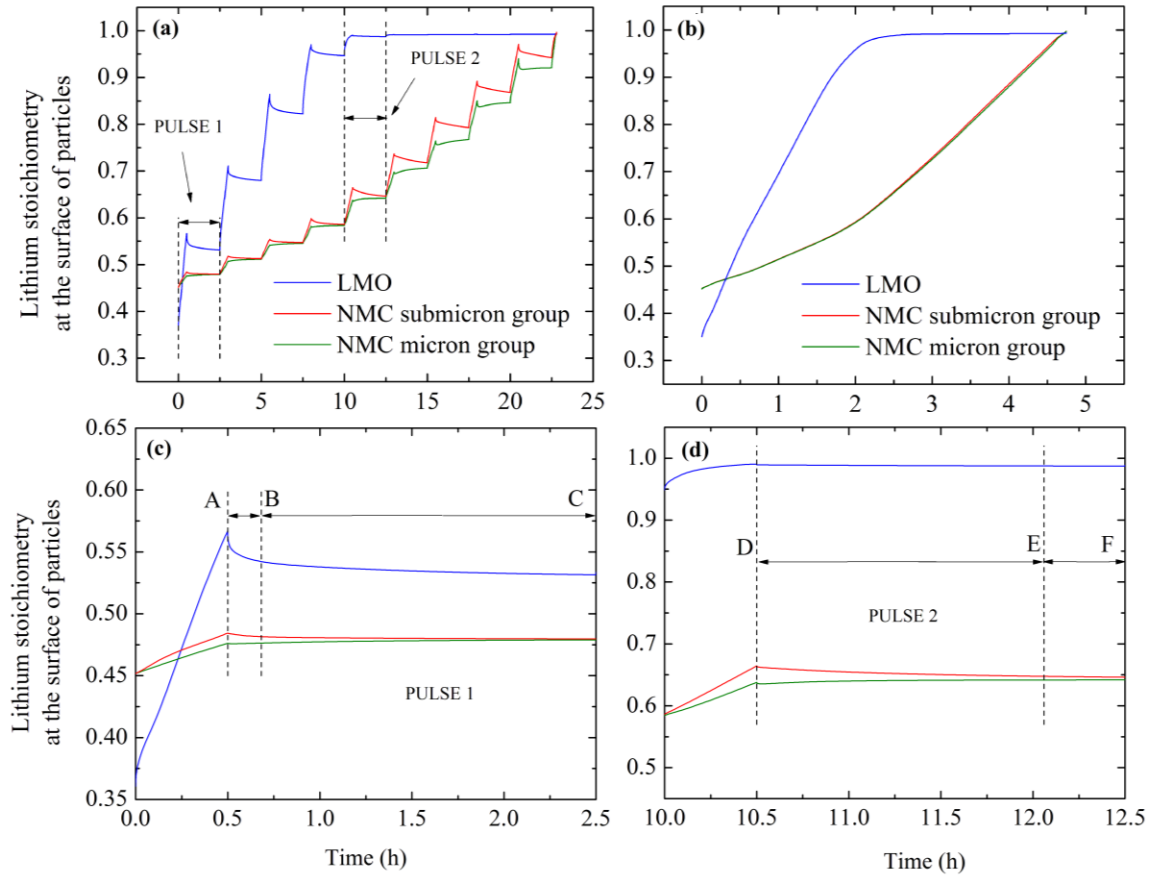
Figure 5.6: Simulated variation of the lithium stoichiometry at the surfaces of particles (a) over the course of the GITT experiment and (b) during galvanostatic discharge at the rate of C/5 in the NMC-LMO blended cathode. PULSEs 1 and 2 in (a) are shown at higher resolution in (c) and (d), respectively, including the segments defined in Figure 5.4b and 4d.

Figure 5.7 shows a comparison between continuous and intermittent galvanostatic discharge data both at C/5. No significant difference in the end-capacity of the electrode is observed between the two operating conditions. In other words, solid-state diffusion is relatively fast (more specifically, diffusion of Li in NMC particles) and the relaxation steps in the GITT experiment, which permit redistribution of matter within each and among all of the active particles, have little or no impact on diffusion barriers towards the end of discharge. This is in line with the surface concentrations shown in Figure 5.6a and 5.6b all having reached close to unity at the end of discharge under both operating conditions. It should be noted that NMC particles mainly determine the end of the discharge process since LMO particles are already fully lithiated midway through discharge.
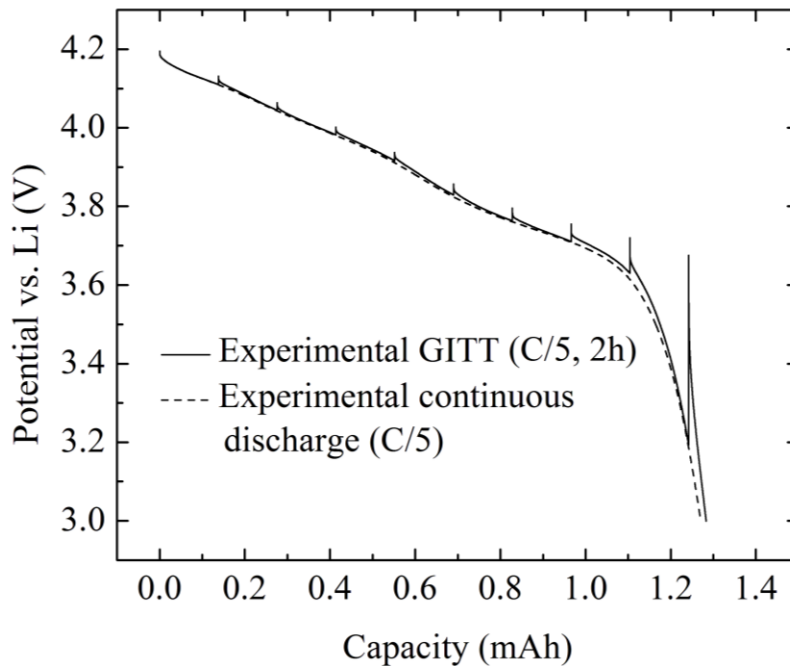
Figure 5.7: Comparison of the experimental GITT (C/5, 2 h) and continuous discharge data at the same rate of C/5.

A schematic diagram describing the flow of lithium between the LMO and NMC submicron and micron particles during the relaxation period can be developed by combining the results from these simulations (Figure 5.8). Figure 5.8a shows the lithium flows into the NMC micron particles from LMO and NMC submicron particles as the former are discharging and the latter are charging. This is consistent with the variation of surface lithium concentration during each of the relaxation periods in Figure 5.6a, the current contributions of the blended cathode components in Figure 5.5 and the behavior observed during periods BC in Figure 5.4a and EF in Figure 5.4b. Based on the currents during periods AB in Figure 5.4a and DE in Figure 5.4b, another mode of internal charge-discharge dynamics is observed during the initial portions of the relaxation period of the first few GITT pulses and is shown in Figure 5.8b, i.e., lithium flows into LMO and NMC micron particles from NMC submicron particles. However, despite this change in mode of internal electrode dynamics during the relaxation period, the surface lithium stoichiometry on the LMO and NMC micron particles decreases monotonically throughout this period (Figure 5.6). This is possible due to the rapid internal diffusion of lithium within the particles which prevents any build-up on their surfaces.

The multi-particle model reveals that the different active materials and size groups in the NMC-LMO blended cathode interact strongly during operation. More specifically, lithium can flow between the LMO and NMC particles, which may influence their surface stoichiometries when the test cell is at open-circuit. Equilibrium may not be attained in time due to the differences in lithiation/delithiation kinetics of the two components. Another factor may be the different diffusion rates within the different sized NMC particles. However, no direct experimental

evidence currently confirming this internal charge-discharge phenomenon predicted by the model has been reported in the literature, to the best of our knowledge.

As previously shown, Mn dissolution from LMO is the primary reason for its capacity loss and the formation of a secondary Li-rich, low-capacity phase at the surface of LMO particles [50, 127-129]. Furthermore, the synergistic interplay between LMO and NMC has been experimentally confirmed [50, 61-62], i.e., the presence of NMC lowers the LMO fade rate in NMC-LMO blended cathodes compared with that of single-component LMO electrodes.

The simulations indicate that the interaction between the electrode components has a balancing effect on the lithium concentration at the surfaces of LMO and NMC particles and tends to prevent the accumulation of excess lithium on the surface of LMO particles. This has the important effect of lowering the likelihood of the irreversible generation of a secondary Li-rich phase that could be the cause of LMO fade. These results can also form the basis of a future experimental study of the mechanistic interplay between LMO and NMC in these blended cathodes.
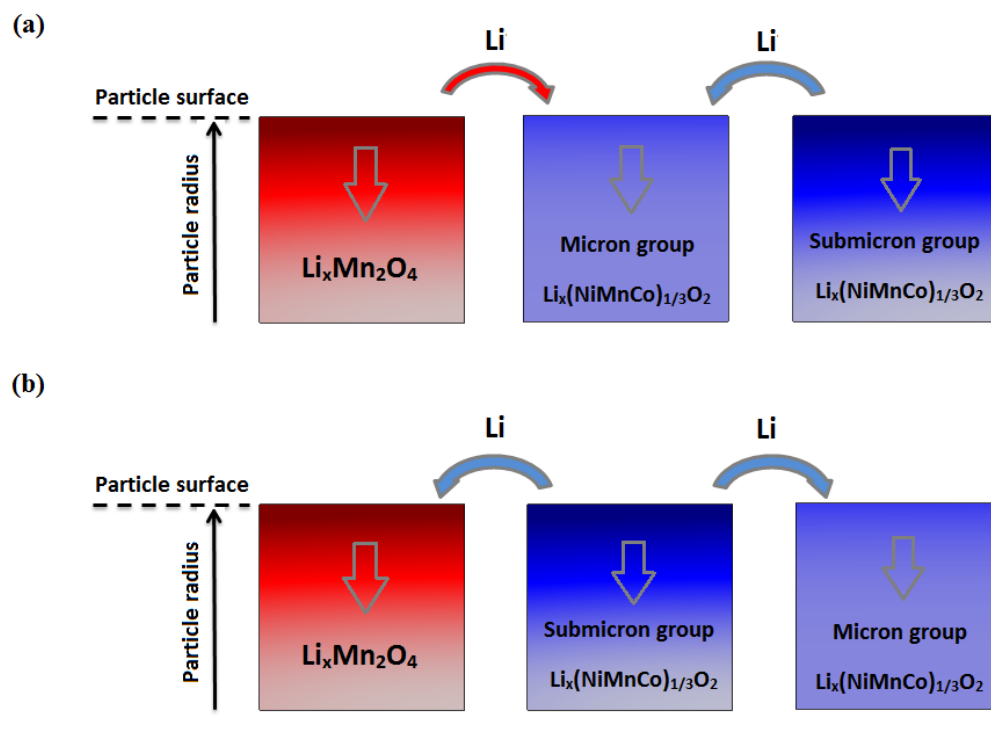
Figure 5.8: Schematic diagram showing the flow of lithium between particles during the BC and EF in Figure 5.4b and 5.6c, and AB and DE in Figure 5.4d and 5.6d, of the relaxation period of GITT experiment, corresponding with: (a) from LMO and NMC submicron particles to NMC micron particles and (b) from NMC submicron particles to LMO and NMC micron particles, separately.

5.4.2 Fitting of model to galvanostatic charge experiments

The multi-particle model and parameters listed in Table 5.2 were found previously to accurately describe the behavior of the blended NMC-LMO electrode during galvanostatic discharge and during galvanostatic intermittent titration technique experiments (GITT). It would be useful to evaluate the accuracy of the model during charge to further analyze the performance of the

blended electrode presented later in this chapter. Accordingly, its validity has been assessed by computing potential-capacity curves without adjustment of any model parameters and comparing them to the curves obtained from galvanostatic charge experiments. As shown in Figure 5.9, good agreement is achieved for the two low C-rates of C/25 and C/10. However, more significant deviations are observed in the remaining curves shown in the figure. Furthermore, the discrepancy appears to grow as the C-rate increases. This indicates that the multi-particle model with the parameter values listed in Table 5.2 is not sufficiently accurate to simulate charging at all C-rates.
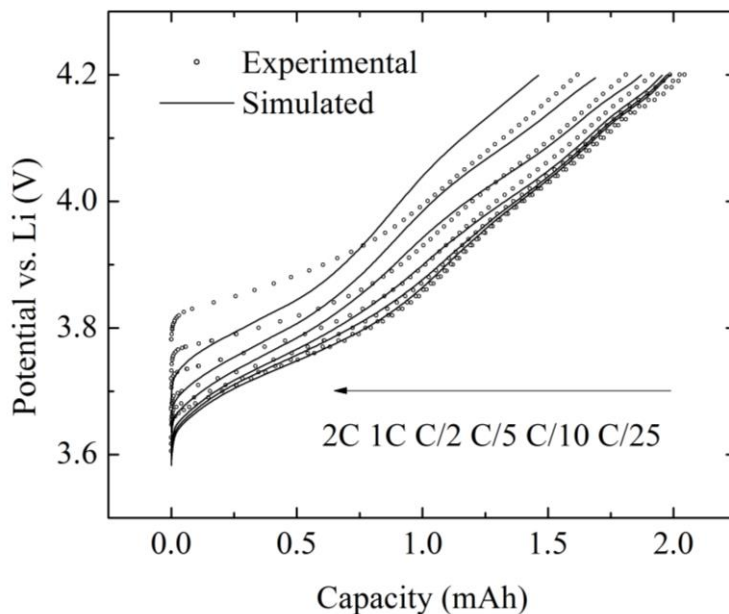
Figure 5.9: Comparison of the experimental potential-capacity curves during charging of a blended cathode to those obtained using the multi-particle model with the parameters in Table 5.2.

Differential capacity curves are usually used to describe the electrochemical signatures of active materials and to evaluate the contribution of each component in a blended cathode. The simulated differential capacity curves during charging are compared with experimental data in Figure 5.10. As discussed in our chapter 3, the peak at ~3.75 V is associated with NMC, while the other two peaks at ~ 4.00 V and ~ 4.14 V are attributed to LMO. Despite discrepancies (e.g., peak positions) between the model and experiment especially at high rates, the characteristic shape of the simulated curves exhibit some similarities with that of the experimental ones. For example, the peak at the highest potential associated with LMO disappears as the charging rate increases, whereas the other LMO peak continues to contribute to the charge capacity.

Table 5.3: List of model parameters.

Parameter	Symbol	LMO	NMC
Rate constant for charge transfer on type n cathode particle (mol/[m^{2}s(mol m^{-3})$^{1.5}$])	k_n	3×10^{-12f}	8×10^{-13f}
Binary diffusion coefficient of Li in type n particle (m^2 s^{-1})	$\mathcal{D}_n$	2.5×10^{-15f}	5×10^{-15f}
Charge-transfer coefficient for charge transfer on type n cathode particle	β_n	0.45^f	0.34^f

f: fitted in the current study to the experimental potential-capacity data
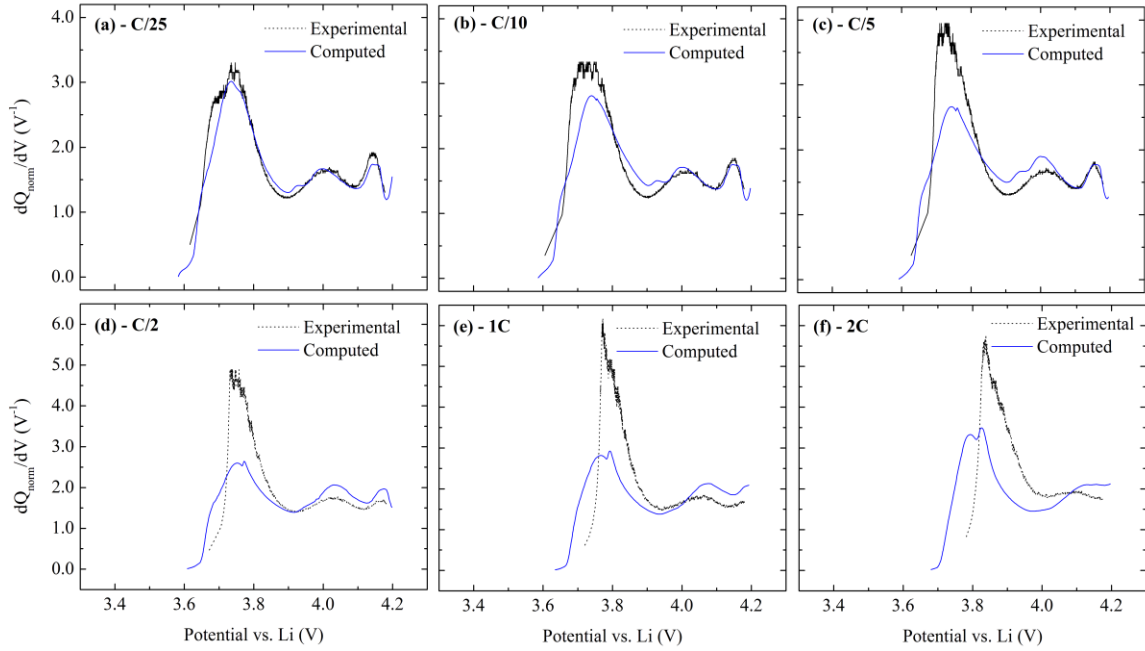
Figure 5.10: Experimental and computed differential capacity curves obtained during charging of NMC-LMO blended electrodes at a C-rate of (a) C/25 (b) C/10 (c) C/5 (d) C/2 (e) 1C and (f) 2C. Model parameters are listed in Table 5.2.

In order to satisfactorily fit the model to all of the potential-capacity curves over the wide range of applied currents from C/25 to 2C, we adjusted the values of 6 parameters. i.e., the rate constants k_n, solid-state binary diffusion coefficients $\mathcal{D}_n$ and charge-transfer coefficients β_n of LMO and NMC. (Note that these parameters are considered to be the same for the sub-micron and micron groups of LMO particles, as was the case in our earlier application of the model to the galvanostatic discharge and GITT data. As shown below, the parameters are adjusted to reflect the respective current contribution of each of the various particles within the blended cathode. The parameter values that give the best fit are listed in Table 5.3, while the fitted

110

potential-capacity curves are presented in Figure 5.11. The match between the simulated and

experimental galvanostatic charging curves has now been considerably improved. The

adjustment of model parameters for charge simulations may be due to the assumption that the

micron-sized NMC particles are nonporous. Given the aforementioned assumption is valid, one

order of magnitude increase in binary diffusion coefficients of the two components may imply

that the solid-state diffusion in the active materials is controlling more strongly on discharge

(i.e., high Li concentration) than on charge (i.e., low Li concentration). It should be noted that

attempts were made to fit the model to both charge and discharge curves simultaneously using a

single set of parameters but the fits were not satisfactory.
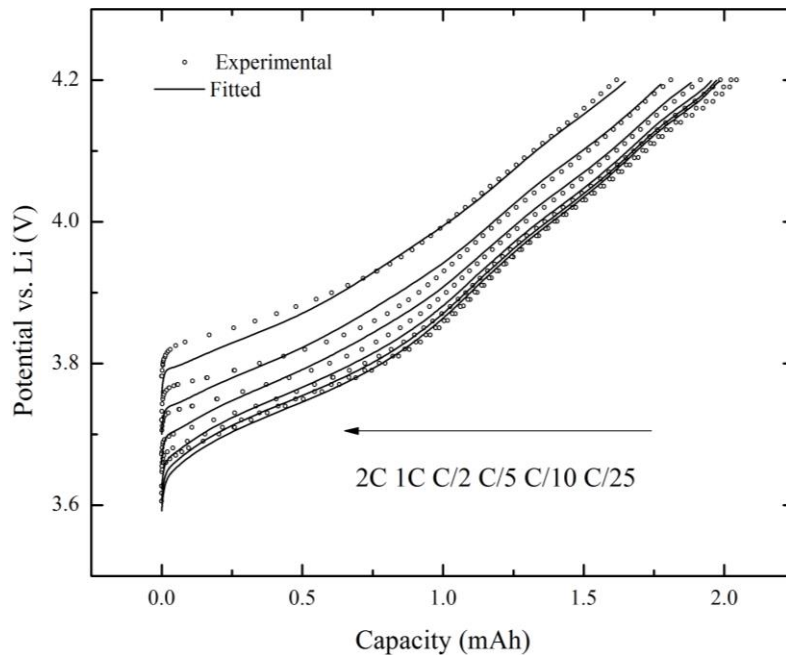
Figure 5.11: Comparison of the experimental and model-fitted potential-capacity curves using

the parameters in Table 5.2 and Table 5.3 for charge of a blended cathode.

111

A comparison of the experimental and computed differential capacity curves in Figure 5.12 also shows an improved match at all charging rates, including the positions of the NMC and LMO peaks. The agreement is particularly good at low C-rates, although less so at higher currents. Note that the computed curves have been obtained using the adjusted parameters given in Table 5.3 and correspond to the simulated potential-capacity curves in Figure 5.11.
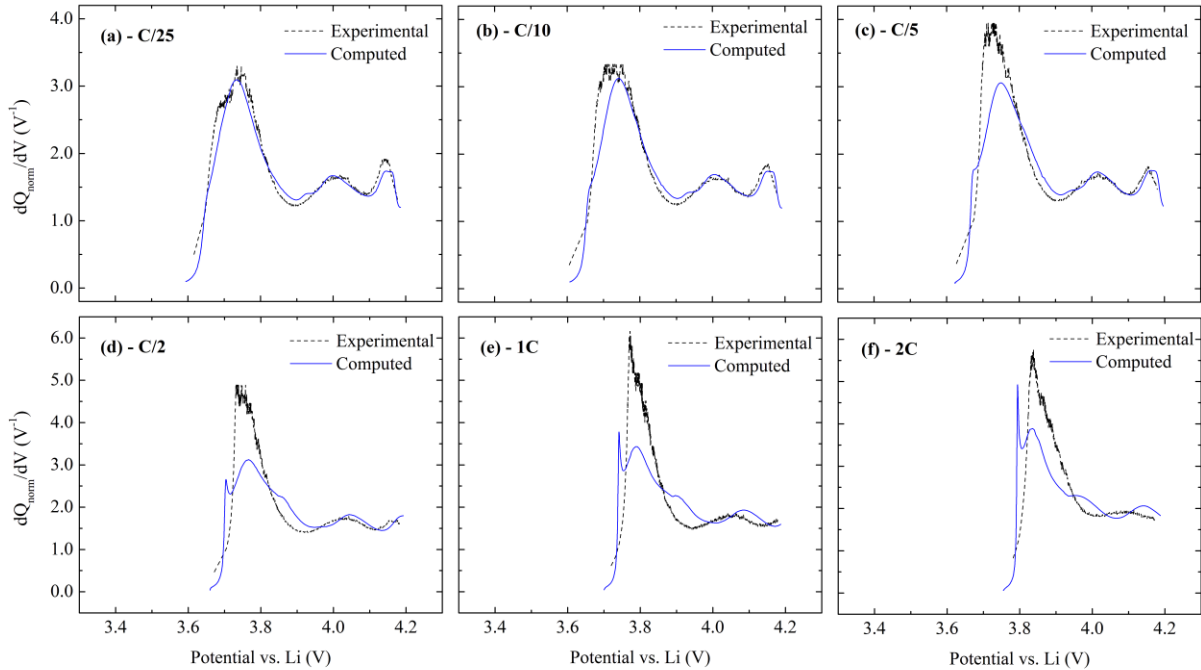

Figure 5.12: Experimental and computed differential capacity-potential curves obtained during charge of NMC-LMO blended electrodes at a C-rate of (a) C/25 (b) C/10 (c) C/5 (d) C/2 (e) 1C and (f) 2C. Model parameters are listed in Table 5.3.

Figure 5.13a and 13b show the contributions of LMO to the total current (black line) and capacity (blue line) of the blended cathode over the course of charging at C/25 and 2C, calculated according to the simulations before (dash line) and after (solid line) adjusting the six

model parameters. LMO begins to delithiate only after about half of the charge time has elapsed and stays active until the end of the charging process. At C/25 (Figure 5.13a), LMO contributes to the current non-monotonically in two stages: in three stages: i) negligible during the first stage AB, ii) sharp increase before leveling off to a plateau at ~ 50% of total current during the second stage BC and iii) continued rise by a smaller extent until the electrode is completely delithiated during the third stage CD. These three stages of delithiation dynamics correspond well to the three differential capacity peaks shown in Figure 5.13. The NMC peak in the differential capacity-potential curves coincides with the first stage, while the two peaks at higher potential correspond to the second and third stages.

At a charge rate of 2C (Figure 5.13b), however, the last delithiation stage vanishes completely in line with the disappearance of the second LMO peak close to the upper cut-off potential. Both simulation sets (solid and dashed lines) follow the same trend at low and high C-rates. They overlap at C/25 but differ more significantly at 2C. The best-fit simulation i.e., after adjusting the model parameters, shows a lower capacity contribution from LMO at 2C compared with that obtained using the original discharge-fitted parameters. Needless to say, the NMC delithiation complements LMO shown in Figure 5.13c and 5.13d. The contribution of NMC to the current and capacity fully dominates the process at both C-rates during the first stage of electrode charging, but then begins to diminish approximately halfway through the process although it is still significant by the end of the process.
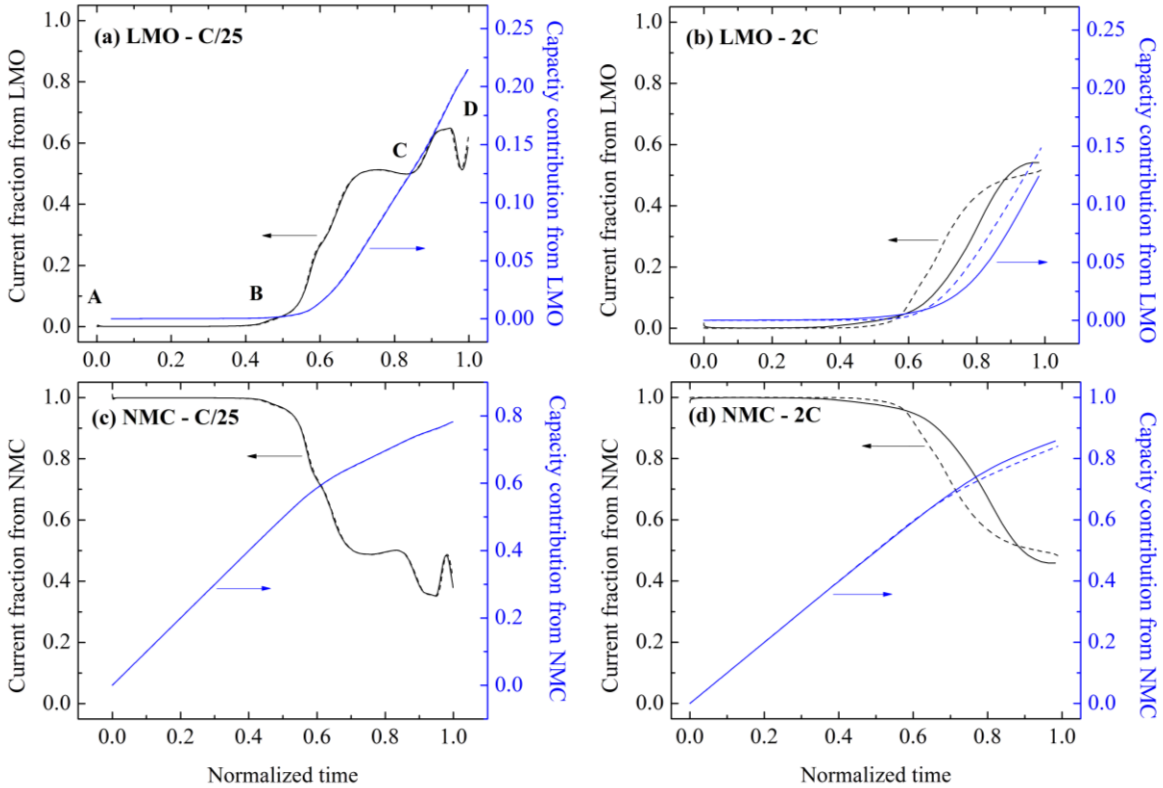
Figure 5.13: Variation of the current (black line) and capacity (blue line) contributions to the blended cathode charging due to LMO (a, b) and NMC (c, d) with normalized time over the course of a single charge at C/25 (a, c) and 2C (b, d). Calculations are based on simulations before (dashed line) and after (solid line) adjusting the model parameters (Table 5.2 and Table 5.3, respectively).

Figure 5.14 compares the experimental end-of-charge and end-of-discharge capacities of the blended electrode measured as functions of C-rate. The electrode performs better on charge than on discharge except at 2C. Moreover, the rate capability on charge is more strongly dependent on applied current compared to the discharge rate capability: the achievable charging capacity drops by a larger amount than does the discharge capacity upon increasing the C-rate. Further evidence

of this charge/discharge asymmetry is presented in Figure 5.15 which shows a comparison of the experimental differential capacity curves during charge and discharge. At the low currents of C/25 and C/10, the curves and peak positions for charge and discharge match quite well. The peak positions during both charge and discharge begin to shift when the current is raised to C/5. This is consistent with the previously observed rise in the electrode potential during the charge process and the reduction in the electrode potential during the discharge process when the C-rate is increased. An interesting observation from the experimental data shown in Figure 5.15 is that during discharge the intensity of the peak at ~3.75V (associated with NMC) decreases while that of peaks at ~4.00V and ~4.10V (associated with LMO) increase as the current is raised from C/25 to 2C. The opposite trend is observed during charging, i.e., the former grows, while the latter diminish. Moreover, unlike the discharge process where the two distinct LMO peaks obtained at low rates (C/25, C/10 and C/5) gradually merge into one broad peak as higher rates (C/2, 1C and 2C) are applied, the LMO peak at ~4.10V shifts to higher values and eventually disappears (i.e., it falls beyond the upper cut-off potential) during charge as the C-rate increases.

In summary, the contributions of the blended electrode components differ depending on whether the electrode is being charged or discharged. This trend is observed more clearly when the areas under the differential capacity peaks associated with each component are calculated to determine the contributions of LMO and NMC to the total end-of-charge/discharge capacities at the various applied currents. The computed contribution of each component to the end-of-charge/discharge capacities obtained with both sets of model parameters is plotted as a function of applied current in Figure 5.16.
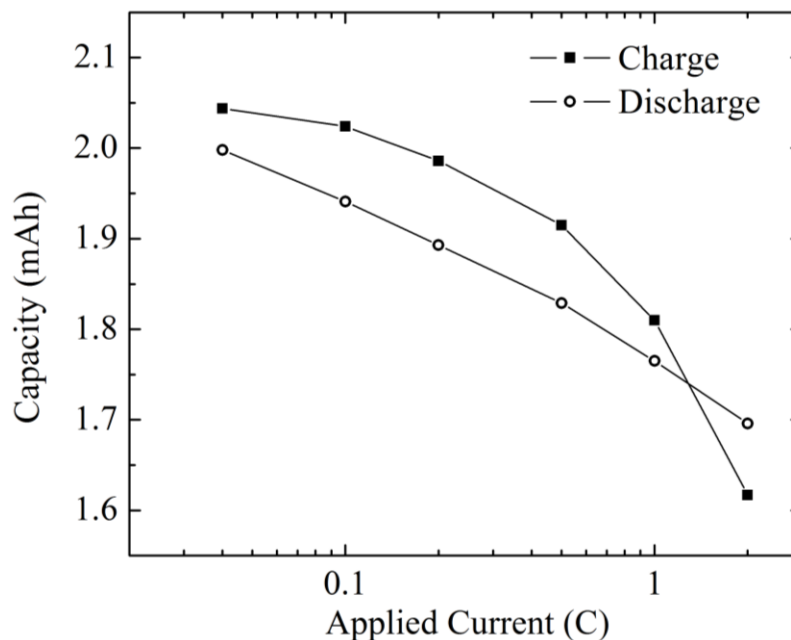
Figure 5.14: Comparison of the experimental rate capabilities of the NMC-LMO blended electrode during charge and discharge.

At the low rate of C/25, the contribution of LMO relative to the total capacity at the end of charge is very close (~0.22) to that at the end of discharge for both sets of charge simulations. The relative contribution of LMO to the electrode capacity during discharge increases if the current is raised, whereas it decreases if the current during charge is raised. Furthermore, the contribution is more strongly dependent on the charge current than on discharge current (Figure 5.16a) closely resembling the overall charge and discharge rate capability of the electrode shown in Figure 5.14. The best-fit charge simulations demonstrate an even greater dependence of the component contribution on the charge current. The effect of current on the contribution of LMO is complemented by that acting on NMC which show the opposite trends (Figure 5.16b). Altogether, the charge/discharge asymmetry of the blended electrode seen in Figure 5.14 is

116

explained by the asymmetry in the contribution of each component to the electrode capacity and

its dependency during charge and discharge which is especially pronounced towards high C-rates.
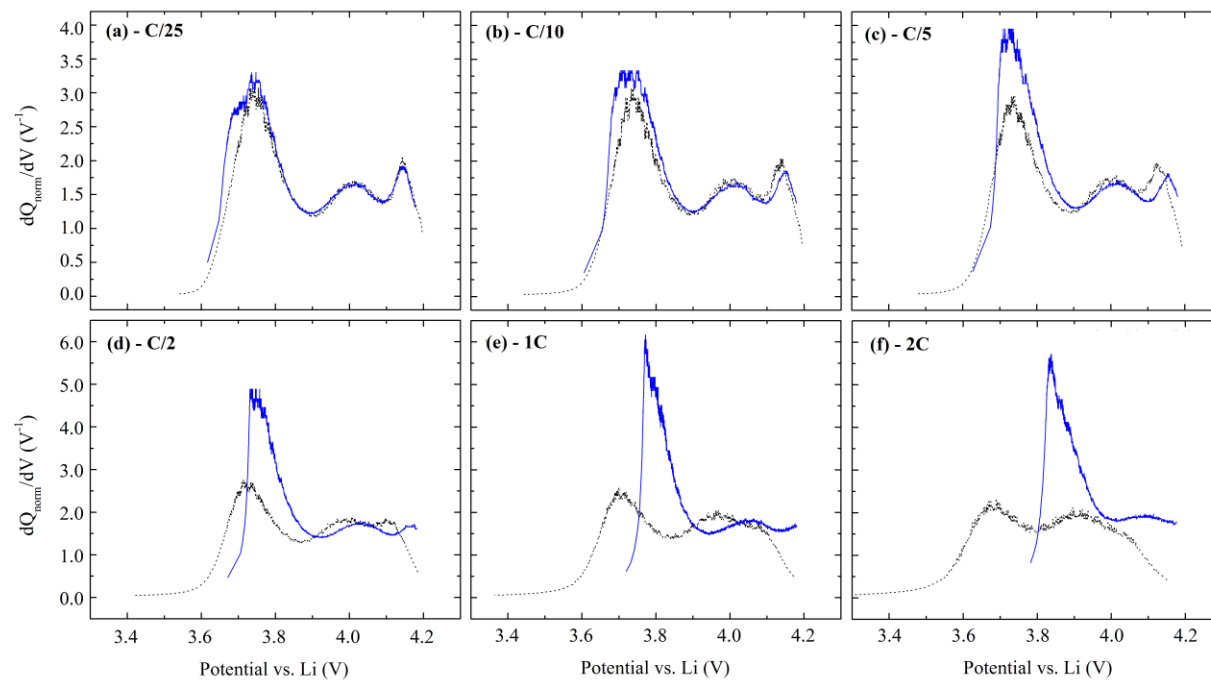
Figure 5.15: Comparison of experimental differential capacity profiles on charge (blue solid line) and discharge (black dotted line) at rates of (a) C/25 (b) C/10 (c) C/5 (d) C/2 (e) 1C (f) 2C.
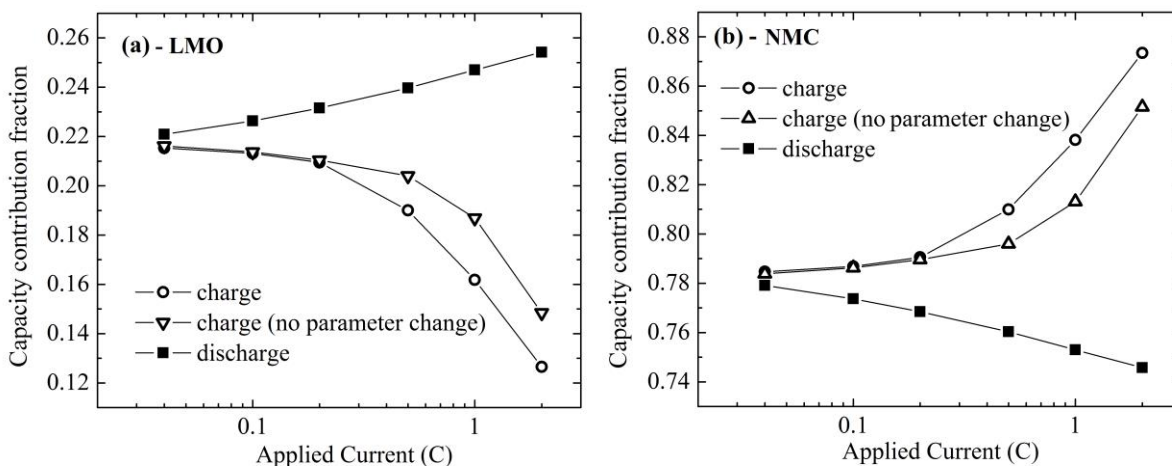
Figure 5.16: The effect of current on the relative contribution of (a) LMO and (b) NMC to the total end-of-charge/discharge capacities of the blended cathode. The curves are generated using the model before (triangles) and after (circles) adjusting the parameters for charge simulations (Table 5.2 and Table 5.3, respectively).

The charge/discharge asymmetry is attributed mainly to the: i) difference in the equilibrium potentials of the two active components at any given Li stoichiometry, ii) difference in the "characteristic shape" of the equilibrium potential functions, iii) composition of the blended electrode and iv) differences in the solid-state diffusion and kinetics limitations of the two components. LMO tends to be preferentially lithiated first while NMC is lithiated last during electrode discharge because LMO has a higher equilibrium potential compared to NMC for a wide range of Li stoichiometry (Figure 3.3). Indeed, LMO is almost fully lithiated while NMC is the sole controlling component near the end of a discharge cycle. (Figure 3.3).

Figure 5.17 shows the equilibrium potential curves of pure NMC, pure LMO and the blended electrode as functions of composition approximated by C/25 discharge curves. Since the discharge rate is so low, the potentials closely approximate the equilibrium potentials of pure NMC, pure LMO and the blended electrode, as discussed in chapter 3. As shown in Figure 5.17, at an overall normalized capacity of 0.8, for example, no more LMO can be lithiated during discharge whereas the constant potential tie line at the overall capacity of 0.2 indicates that NMC still has a considerable Li content of ~ 0.12 to be removed during charging. Although the process is dominated by NMC at the beginning of the charge process, it never becomes fully delithiated before LMO does. In contrast to the discharge process, both NMC and LMO are actively involved in the charge process until the upper cut-off potential is reached.

In other words, if the equilibrium potential of NMC and LMO were symmetric with respect to the blended electrode equilibrium potential over the potential range of 3.0 – 4.2V, one would expect NMC and LMO particles to undergo the process in the exact opposite order during electrode charge, i.e., complete delithiation of NMC first followed by that of LMO during the remainder of the process. Such symmetry would depend on the characteristic shape of the individual equilibrium potentialscurves and on the composition of the electrode.

In the practical case of the blended electrode studied here, a strong dissimilarity between the shapes of the equilibrium potential curves of the two components exists (Figure 5.17) which leads to different internal dynamics of the electrode during charge than during discharge.

In general, diffusion limitations become significant toward the end of a charge and discharge. Thus, whereas Li diffusion in NMC is controlling at the end of discharge, diffusion in both LMO

and NMC is limiting at the end of charge according to the above thermodynamic consideration. Therefore, the secondary cause of the charge/discharge asymmetry is dynamic and associated with the differences in the solid-state diffusion within and charge-transfer kinetics at the surface of the two cathode components. As discussed previously, the parameter values that enable the model to closely match the discharge potential-capacity curves fail to do so when the model predictions are compared to the experimental galvanostatic charge data. Moreover, the asymmetric contribution of LMO and NMC to the total capacity at the end charge and discharge, although predicted, is overestimated by the model using the original set of parameter values (Figure 5.16). The adjustment of the parameters such as the solid-state diffusion coefficients and reaction rate constants (Table 5.3) significantly improves the fit of the model to the experimental charge data including the end-of-charge capacities. This confirms the role that the solid-state diffusion and reaction kinetics and their differences between the two components play in the blended electrode charge/discharge asymmetry.
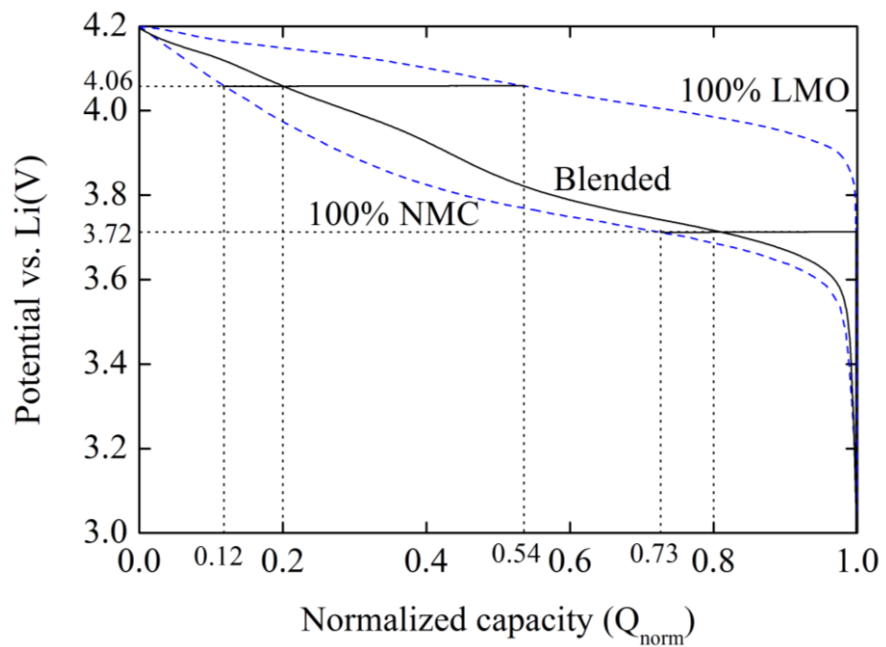
Figure 5.17: Experimental discharge profile (solid line) of the blended cathode at C/25 and simulated discharge profiles (dashed lines) of pure NMC and LMO cathodes at C/25 (based on Figure 3.3 in chapter 3).

Chapter 6 Calendar aging study

The following section is based on the work '*Calendar Aging Study and Compression Effect Analysis of Commercial NMC-LMO/graphite Blended Lithium-ion Battery*' by Z. Mao et al. and is ready for submission. This thesis author specific contribution to this paper was to: apply the model, conduct the simulations and experiments, prepare all the graphics and results, and prepare the final manuscript and reviewer edits with direction from the project supervisors who were M. Fowler, Z. Chen and M. Pritzker.

6.1 Introduction

After undergoing several generations of development as energy storage devices, lithium-ion batteries (LIB) are now widely used in consumer electronic products and are being further broadened for use in the automotive industry. The introduction of commercial LIBs consisting of $LiNi_xMn_yCo_{1-x-y}O_2$ - $LiMn_2O_4$ (NMC-LMO) blended cathodes and graphite anodes has been so successful that they now dominate the burgeoning market of automotive LIBs due to their superior performance. In order to continue optimizing the design of these batteries, a number of experimental and modeling studies on the operating behavior, life cycle, degradation mechanism, etc., of blended cathodes have been conducted. For instance, several research groups have studied the cycling [130-132] and calendar aging [133-134] of commercial 18650 cylindrical graphite/NMC-LMO batteries and concluded that the loss of cycleable lithium, decomposition of the electrolyte and loss of active materials are the most significant aging processes that are strongly affected by the discharge/charge rate, temperature and state of charge (SOC).

In addition, based on aging experiments and analyses, mechanistic and semi-empirical models have been proposed to simulate the capacity fade or resistance increase of NMC-LMO batteries and ultimately predict their useful operating lifetimes [134-136]. Jung [79] developed a mathematical model for a graphite-soft carbon/NMC-LMO full cell for the purpose of designing new electrodes and predicting the performance for different cathode compositions. In our previous work (chapter 3 and 4), we developed a model-based approach to identify the unknown composition of a blended cathode and presented a multi-particle model to describe the electrochemical performance at different charge-discharge C-rates that accounts for the effects of particle size distribution, solid-state diffusivities and electronic conductivities in a commercial NMC-LMO (70:30 wt%) blended cathode.

In this chapter, storage experiments at various temperatures and SOC conditions are conducted to characterize the calendar life of commercial 15Ah pouch cells containing NMC-LMO/graphite active materials. This involves the combined post-mortem analyses and use of an OCV-model for the fastest-degraded cell under the most severe aging conditions to shed more insight into the mechanisms for capacity fade. Finally, a non-destructive pressure-loading test was carried out and found to dramatically improve the capacity of the aged cell. Through loading a pressure, the gas generated by side reaction has been redistributed and then the connection between each component has been tightened, leading to a good ionic and electronic transfer and further more contribution of effective active materials during charge and discharge. The pressure loading is a simple and effective operation for the aged cell; it is firstly proposed here and its application can make the life of aged cell longer.

6.2 Experimental

6.2.1 Calendar life test

The calendar life study was conducted on eight commercial lithium ion pouch cells. Each pouch cell was comprised of an NMC-LMO blended cathode and graphite anode with a nominal capacity of 15Ah for application in a plug-in hybrid electrical vehicle (PHEV). Each cell was tested under one of four possible storage conditions so that duplicate experiments were conducted for each condition. The conditions include testing cells with initial SOCs of 0% and 100% by storing them at temperatures of 35°C and 58°C, i.e., 0% SOC at 35°C, 0% SOC at 58°C, 100% SOC at 35°C and 100% SOC at 58°C.

Prior to storage, each pouch cell with initial 50% SOC was characterized in terms of its capacity, rate capability and resistance and then disposed to 0% or 100% SOC using a MACCOR 4200 series battery test system. The capacity and rate capability were determined by subjecting a cell to a constant-current constant-voltage (CC-CV) waveform consisting of the following steps: i) discharge at a specified C-rate until a potential of 2.8 V is reached, ii) discharge under a constant voltage of 2.8 V until a current of C/20 is reached, iii) 10-min rest, iv) charge at the same C-rate until a potential of 4.15 V is reached, v) charge at a constant voltage of 4.15 V until a current of C/20 is reached and vi) 10-min rest. It should be noted that a 1 C-rate corresponds to a current of 15 A. The capacities at C/25 and 1C were measured by applying the charge-discharge cycle described above at a rate of C/25 followed by a sequence of three of these cycles at a rate of 1C. The 1C-capacity was obtained from the average obtained over these three cycles. The rate

124

capabilities at various C-rates were determined by applying cycles operating at the following currents: C/5, C/2, 1C and 2C.

In order to determine the direct current inner resistance (DCIR), we used the two-tier DC load method. This involved discharge of a fully charged cell for a 10 s duration at C/5 followed immediately by further discharge at a higher rate by stepping up to 2C for another 10 s. At the end of this second step, the current was immediately reduced back to C/5 and this procedure was repeated for a total of five cycles. The value of the R_{DCIR} over each C/5-2C discharge sequence was calculated according to Eq.6.1,

$$R_{DCIR} = \frac{U_{C/5} - U_{2C}}{I_{C/5} - I_{2C}},$$

(6.1)

where $U_{C/5}$ U_{2C} are the potentials at the moments of the pulse end at C/5 ($I_{C/5}$) and the pulse beginning at 2C (I_{2C}), respectively. The value reported in this study was the average over the 5 DCIR measurements obtained for each sample.

After these baseline measurements, the following procedure was adopted to ensure that a cell was either fully discharged or fully charged. Discharge to 0% SOC was achieved by applying step i) above at a rate of 1C followed by step ii). Cells were charged to 100% SOC by applying iv) at 1C followed by step v). After checking that the cell potentials were holding at the correct values for complete discharge or charge, two of the 0% SOC cells and two of the 100% SOC cells were put into an oven operating at 35˚C, while the remaining four cells were placed in an oven at 58˚C. The cells were maintained at open-circuit in both ovens. In order to monitor the change in the performance of these cells upon aging, they were characterized at 30 day intervals. After removal from the ovens, the cells were allowed to cool to room temperature and stabilize

for at least 4 hours and their potentials were measured before their capacities, rate capabilities and DCIR values were determined. These quantities were measured exactly as described above for the cells prior to aging with the exception of capacity. In this case, the capacity at C/25 was not determined and only the value of 1 C was determined. As before, the capacity reported here was the average of three measurements obtained from consecutive charge-discharge cycles at 1 C. After the periodical tests, the cells were addressed into the initial SOC, i.e., 0% and 100% as the procedure described at the beginning of this paragraph and placed back in the ovens again.

6.2.2 Coin cell experiments

Experiments were conducted on half-cell coin electrodes taken from fully charged pouch cells that had been aged for 280 days at 58°C. For comparison, similar half-cell tests were done on coin cells fabricated from fresh unused fully charged pouch cells. Before disassembling the pouch cells, we ensured that they were fully discharged. Each of these cells consisted of sixteen double-side-coated rectangular cathode sheets (18.9cm×14.15cm) and seventeen anode sheets (19.2cm×14.5cm). The components of the coin cells were fabricated from a cathode sheet and anode sheet removed from the middle portions of fresh and aged cells. Before this was done, the coating on one side of the cathode sheet was removed using N-methyl-2-pyrrolidone (NMP) solvent. Circular samples (0.712 cm2 area) were then punched from the one-side coating cathode and anode sheets. In order to remove any lithium salt that had deposited, the circular samples were rinsed in dimethyl carbonate (DMC) several times. Two types of coin cells were fabricated – cathode half-cell coin cells and anode half-cell coin cells. The washed circular samples punched from the cathode sheet of the pouch cell and Li foil comprised the electrodes of the

126

cathode half-cells. The anode half-cells consisted of the washed circular samples punched from the anode sheet of the pouch cell and Li foil. In each case, the components were assembled into an electrode/separator/Li coin cell using Celgard 2500 separator and 1M LiPF6 in 1:1 EC/DMC solution. The same procedure was used to fabricate the coin cells from the fresh and aged cathode and anode sheets. In order to ensure the repeatability of measurements, at least two coin cells were mode from each cathode and anode and tested. The entire process of disassembling the pouch cells and fabricating the coin cells was conducted in an argon-filled glove box.

A series of galvanostatic experiments was carried out on both the anode and cathode half-cell coin cells using the Neware CT-3008-5V 10mA-164-U battery test system. Prior to these experiments, each cell was subjected to five formation cycles, as described in our previous studies (chapter 3 and 4), conducted at a current of 1 mA (~0.69 C for a cathode half-cell and ~0.60 C for a anode half-cell) to ensure that it had attained a stable electrochemical state. The specific galvanostatic experiments for the cathode half-cells consisted of rate capability tests conducted in the sequence C/10, C/5, C/2, 1C and 2C over the potential window from 3.0 V to 4.2 V and charge-discharge tests at C/25 over the potential window from 3.0 V to 4.4 V. A 1 C-rate corresponded to 1.44 mA applied current in the case of the cathode half-cells. A similar testing profile was used for the anode half-cells. The upper and lower cutoff potentials were 1.5 V and 0.005 V for all the rate capability experiments from C/25 to 2C. A 1 C-rate corresponded to an applied current of 1.66 mA for the anode half-cells.

6.2.3 Pressure loading experiments
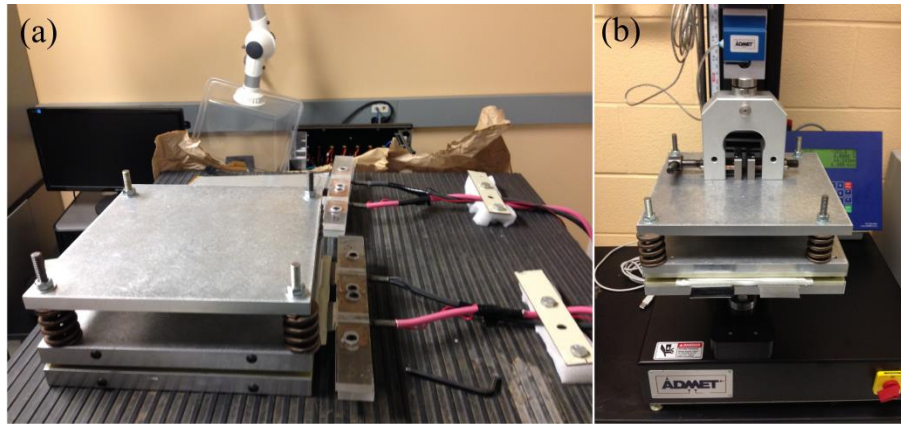
Figure 6.1: (a) Pressure set-up and (b) supporting instrument.

A set-up consisting of three copper-tin plates, two plastic plates (23.5cm×24cm) and four springs was designed and constructed to study the effect of applied pressure on the performance of an initially fully charged pouch cells aged at 58˚C (Figure 6.1a). The two plastic plates directly stick with two copper-tin plates as two entire copper-tin-plastic ones separately. Then, the aged cell was placed between the two plates and in direct contact with the plastic interface, and then a pressure of 4 psi (~ 763 N) was applied to this stack by tightening the four screws and monitoring the testing force sensor (ADMET L22LRYA61) mounted on the supporting instrument (Figure 6.1b). Through this way, when to load a pressure on the top of set-up, the force can uniformly transfer towards the bottom via the four springs. Therefore, the pressure of the testing force sensor can represent the force at the each spot throughout the set-up and the cell. At this pressure of 4psi, the cell was charged and discharged at the rate of C/25 to measure the capacity using the MACCOR 4200 battery test system. Then, following the order shown in Figure 6.2, the pressure on the pouch cell was adjusted and corresponding the capacity at C/25

was measured. The way of force loading is the same with the above description but the pressure value.

Pressure-path	Pressure (Psi)
Step 1:	4.0
Step 2:	4.5
Step 3:	5.0
Step 4:	4.5
Step 5:	4.0
Step 6:	3.0
Step 7:	2.0
Step 8:	1.0
Step 9:	0

Figure 6.2: Pressure-path capacity test profile.

6.3 Results and Discussions

6.3.1 Capacity Degradation During Aging

The change in the capacities remaining in the pouch cells as measured at the four discharge rates of C/5, C/2, 1C and 2C during the course of the four aging experiments is presented in Figure 6.3. Interestingly, regardless of the discharge rate, the capacities of the cells that were initially fully discharged increased during the early stages of aging before decreasing thereafter (Figure 6.3a and b). The initial rise in capacity before beginning to drop that is evident for these pouch

cells has been reported previously [137-138], although no cause for the initial increase in capacity was offered. Furthermore, this initial rise was much more pronounced at the lowest discharge rate of C/5 than at the higher currents. In fact, the capacity measured at C/5 reached ~101.8% after 60 days of storage at the low temperature of 35°C (Figure 6.3a), while it reached the same level after only 30 days of storage at the higher temperature of 58°C (Figure 6.3b). Further examination of Figures 6.3a and b shows that decline in capacity that occurred after the initial rise was not severe if the pouch cell was completely discharged at the outset. When the pouch cell was stored at 35°C, its capacity still remained above 100% even after 330 days of aging. When it was stored at 58°C, the remaining capacities were still as high as 97-99% of their initial level even after 300 days of aging.
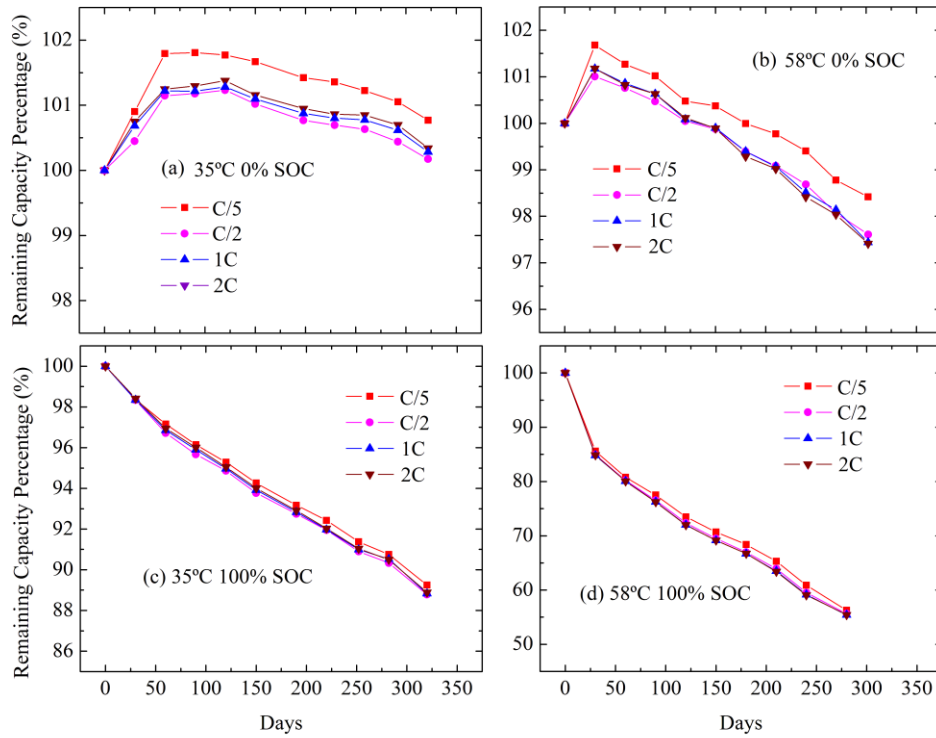
Figure 6.3: Effect of storage temperature and initial SOC (a) 35˚C, 0% SOC (b) 58˚C, 0% SOC (c) 35˚C, 100% SOC and (d) 58˚C, 100% SOC on percent capacity remaining in pouch cells, measured at discharge rates of C/5, C/2, 1C and 2C during the course of aging.
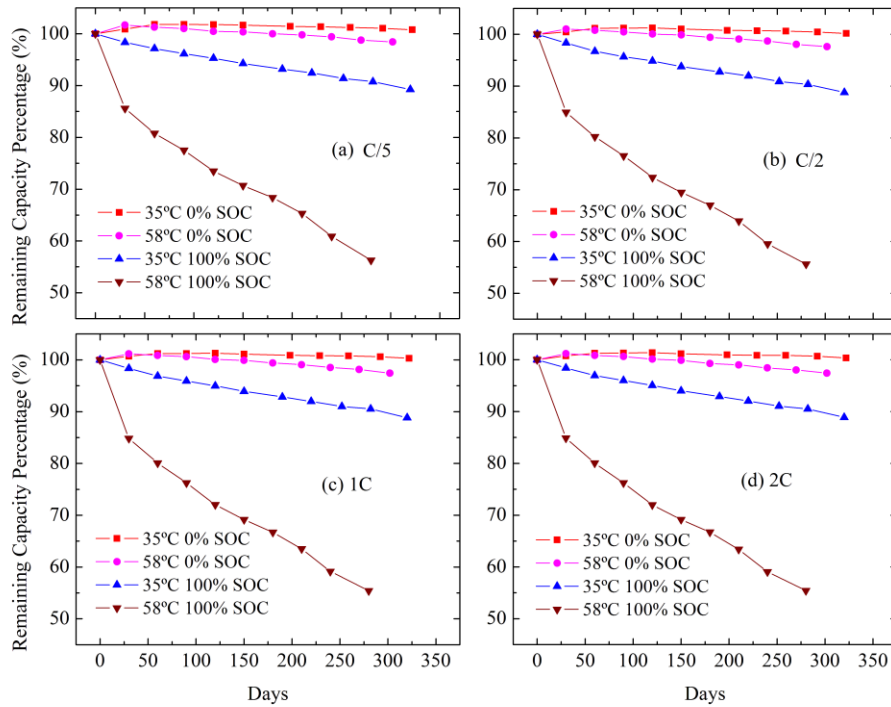
Figure 6.4: Percent capacity remaining in pouch cells measured at discharge rate of (a) C/5 (b) C/2 (c) 1C and (d) 2C over the course of aging depending on the following initial SOC and storage temperatures: 0% SOC at 35˚C, 0% SOC at 58˚C, 100% SOC at 35˚C and 100% SOC at 58˚C.

The aging of fully charged pouch cells, on the other hand, was found to be significantly different than that of fully discharged cells (Figures 6.3c and 6.3d). Firstly, no rise in capacity at the outset of storage was observed. Secondly, the degradation in capacity was much more severe and storage temperature was found to have a much larger effect when fully charged pouch cells were aged. In fact, the remaining capacity decreased almost linearly with time at the two storage temperatures. After 280 days, more than 88% capacity still remained in the cells stored at 35˚C (Figure 6.3c), while less than 60% capacity was left in the cells stored at 58˚C (Figure 6.3d).

This also indicated that the storage temperature had a much stronger effect on aging of the fully charged cells than fully discharged cells. On the other hand, the results in Figure 6.3 reveal that the measured capacity after aging at both temperatures is not strongly affected by the discharge rate regardless of the initial SOC of the pouch cells. The effects of initial SOC and storage temperature are clearly evident if the data presented in Figure 6.3 are reorganized so that the remaining capacities measured at a particular discharge rate are plotted together as shown in in Figure 6.4. At each of the C-rates, the capacity of the cells with 100% SOC that were stored at 58˚C always degraded most rapidly, whereas those with 0% SOC aged at 35˚C degraded most slowly.

Figure 6.5 presents the waveforms for the input current during galvanostatic pulse discharge experiments and the corresponding output potentials from both a fresh unaged fully charged pouch cell and an initially fully charged cell that has been aged by storing it at 58˚C for 280 days. Several differences in the responses of the two cells can be observed. The potential of the aged cell always remained well below that of the fresh cell at comparable stages in any pulse. In addition, the difference between the highest and lowest potential over the course of a pulse was always much larger in the case of the aged cell. Finally, the aged cell exhibited a considerably larger drop in potential on going from one pulse to the next. Analysis of the potential output using Eq.6.1 revealed that the DCIR of the fully charged pouch cell increased from 2.4 mΩ before storage to 6.2 mΩ after 280 days storage at 58˚C.
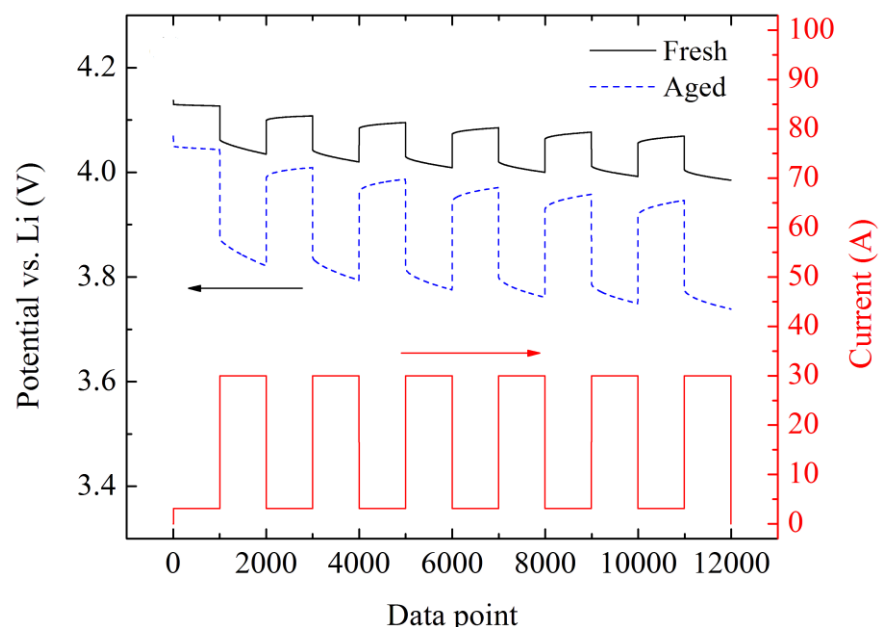
Figure 6.5: Comparison of galvanostatic pulse discharge curves before and after storage of initially fully charged pouch cells for 280 days at 58°C.

The discharge and charge potential-capacity curves (constant current part) of fully charged pouch cells before and after 280 days of storage at 58°C are compared in Figure 6. These data show that only about 55% of the available capacity of the aged cell was actually used when the lower cut-off potential of 2.8 V was reached regardless of the C-rate (Figure 6a). On the other hand, the capacity attained by the end of charge to a potential of 4.15 V exhibited a stronger dependence on the C-rate. It decreased considerably as the C-rate increased from C/5 to 2C, but reached only about 55% of the available capacity when charged at a current of C/5 and as low as about 37% when charged at a rate of 2C.

134
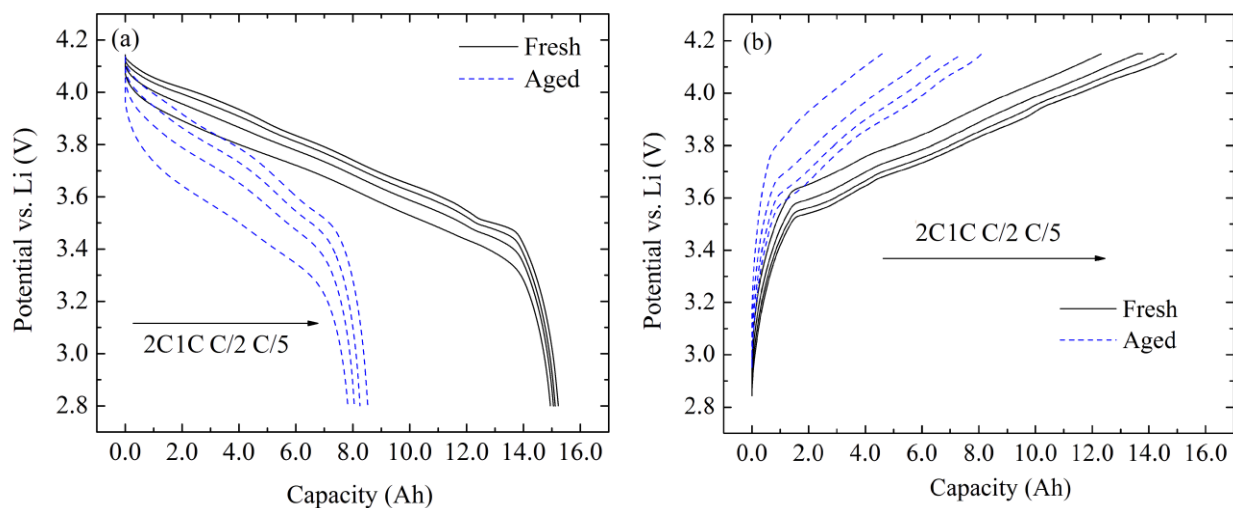
Figure 6.6: Comparison of (a) discharge and (b) charge potential-capacity curves before and after 280 days calendar aging under 58℃-100% SOC states.

6.3.2 Aging mechanisms analysis

In order to investigate the mechanisms of capacity loss for calendar aging, the unused and aged fully charged pouch cells after 280 days of storage at 58℃ were disassembled and the four types of electrode‖separator‖Li coin cells, i.e., fresh, aged cathodes and anodes, were fabricated, as described in the Experimental section. A comparison of the discharge potential-capacity curves and end-of-discharge capacities of the cathode half-cells measured at rates of C/10, C/5, C/2, 1C and 2C are shown in Figure 6.7a and 6.7b, respectively. These data show that aging led to a small capacity decrease and potential plateau reduction of the cathode at all currents. As our previous study in chapter 3, the cathode was comprised of a blend of NMC and LMO active materials. A normalized differential-capacity curve has been drawn to determine the loss due to each component by examining the intensity of the signature peaks for the two components

135

(~3.75V for NMC, ~4.00V and ~4.14V for LMO) in Figure 6.8. However, these results reveal that aging did not lead to any significant difference in the intensity of the peaks at any of the currents, although it did cause a small shift in the peak positions toward lower potential which tended to grow as the current rose. This shift was consistent with a decrease in the potential plateau in the potential-capacity curves during discharge (Figure 6.7a).
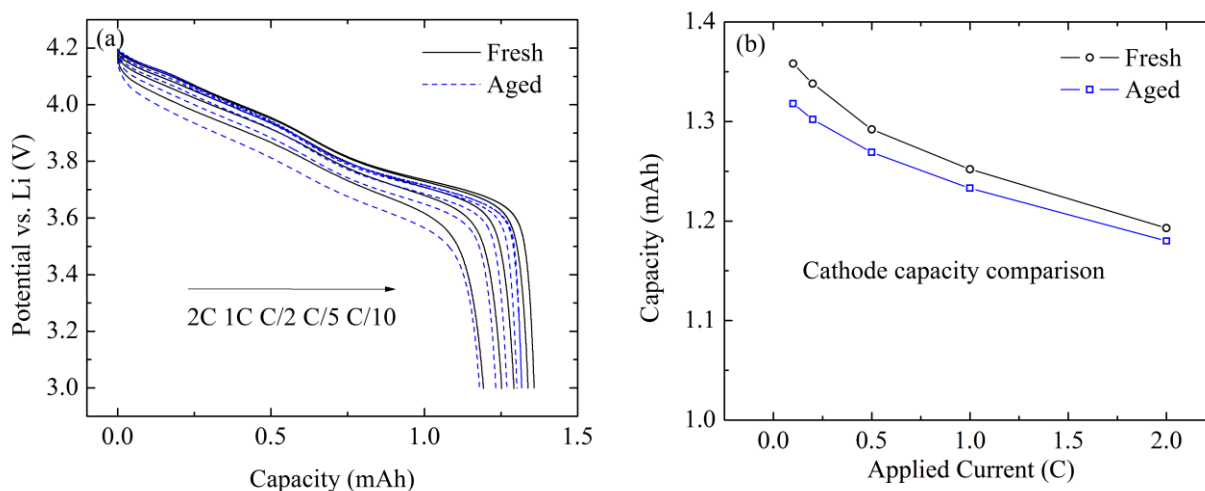
Figure 6.7: Comparison of (a) potential-capacity curves and (b) end-of-discharge capacity-current curves for discharge of cathode coin half-cells fabricated from fresh and aged (stored for 280 days at 58℃) fully charged pouch cells.
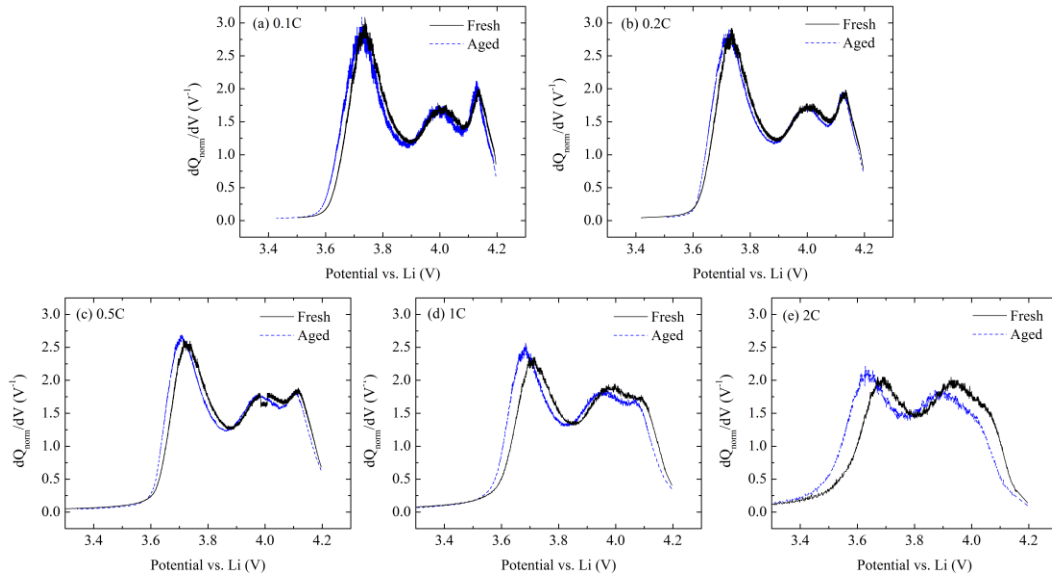
Figure 6.8: Differential-capacity curves of fresh and aged cathodes obtained at a C-rate of (a) C/25 (b) C/10 (c) C/5 (d) C/2 (e) 1C and (f) 2C.
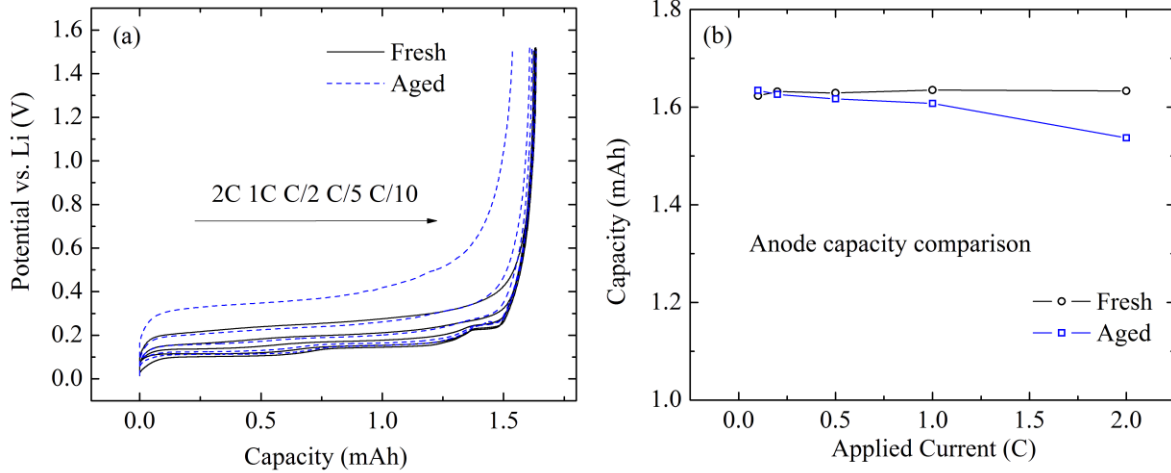
Figure 6.9: Comparison of (a) potential-capacity curves and (b) end-of-charge capacity-current curves for charge of anode coin half-cells fabricated from fresh and aged (stored for 280 days at 58℃) fully charged pouch cells.

A comparison of charge potential-capacity curves and end-of-charge capacity of anode coin half-cells fabricated from fresh and aged (stored for 280 days at 58℃) fully charged pouch cells rates are presented for a range of currents from C/10 to 2C in Figure 6.9a and 6.9b, respectively. For the pouch cell, I am using discharge curve where cathode keeps to discharge while anode is to charge. A relatively small loss in capacity was observed in the aged anode coin half-cell at all rates although it tended to grow with the C-rate. On the other hand, aging had very little effect on the potential-capacity curves of the anode coin half-cells (Figure 6.9a). A summary of the percent capacity losses in the aged pouch cells and cathode and anode coin half-cells at the rates of C/5, C/2, 1C and 2C is provided in Table 6.1. The most noteworthy aspect of these results is not that aging led to capacity losses in all cases, but that the losses for the entire pouch cells were so much larger than that of the coin cells made from the pouch cell active material components. For example, capacity fades of 2.69% and 0.37% were measured for the cathode and anode coin half-cells at C/5, respectively, whereas a 43.9% loss was observed in the entire pouch cell from which the coin cells were fabricated. This huge difference indicates that most of the capacity loss of the pouch cell during aging did not originate from the degradation of the cathode and anode active materials themselves. It should be recalled that each coin cell consisted of a cathode or anode removed from an aged pouch cell combined with lithium metal foil as the other electrode and fresh electrolyte of 1M LiPF6 dissolved in 1:1 EC/DMC. The use of fresh electrolyte enabled the source of lithium for this cell to be replenished. The dramatic improvement in utilization of the active material in the coin cells compared with that in the original aged pouch cell cells regardless of the C-rate suggests that the degradation in the capacity of the pouch cells is caused by the loss of cycleable lithium.

This loss of cycleable lithium can be attributed predominantly to the formation and growth of passivation layers on the surface of graphite during calendar aging. Figure 6.10a shows SEM images of a portion of a fresh fully discharged graphite anode and a portion of a fully discharged graphite anode aged at 58°C for 280 days. The image of the aged sample clearly shows the build-up of a layer or product on the graphite anode. Elemental composition of the marked portion of the surface of the aged anode (Figure 6.10b) by EDX analysis reveals that it contained F and P with atomic percentages of 6.81% and 1.5%, respectively comparing with only 0.9% F in the fresh anode (Table 6.2). The presence of F and P is important since these elements could only originate from the electrolyte. A more detailed discussion of the formation and composition of the passivation layer can be found in Refs. [139-143]. Generally, it is formed by the decomposition of electrolyte that can impede the charge and ionic transfer resistance, leading to the increase of inner resistance of the anode in the aged pouch cell, as observed previously (Figure 6.5), and decrease of anode capacity at high C-rate, i.e., 2C (Figure 6.9b).
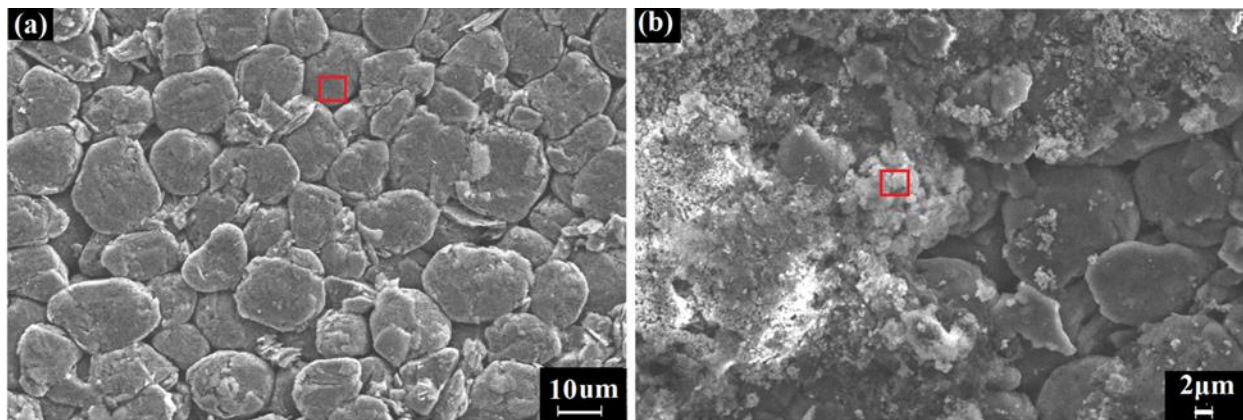
Figure 6.10: SEM image of the anode surface in (a) fresh and the (b) aged cell.

Table 6.1: Summary of percent capacity losses measured at C-rates of C/5, C/2, 1C and 2C for fully charged cells stored at 58℃ for 280 days.

Rate	C/5	C/2	1C	2C
Total capacity loss in aged pouch cell	43.9%	45.4%	46.5%	47.7%
Cathode capacity loss in coin cell	2.69%	1.78%	1.52%	1.09%
Anode capacity loss in coin cell	0.37%	0.74%	1.69%	5.88%
Aging mechanism	Cycleable lithium limiting			

Table 6.2: Elemental composition of the marked area in Figure 6.10b obtained from EDX analysis.

		C	O	F	Al	P
atomic %	Fresh	93.9	5.2	0.9	-	-
	Aged	29.2	58.0	6.8	4.5	1.5

Differential voltage (dV/dQ vs.Q) measurement [144] and the OCV fitting [81] are useful tools to analyze the reasons for the loss in capacity of the pouch cells by matching their differential voltage vs. capacity and potential vs.capacity curves to those of half-cell coin cells. In these analysis, the potential of the pouch cell U_{pouch} is a function of its capacity Q_{pouch} and can be calculated using the potentials of the cathode coin half-cells $U_{cat}(\alpha_{cat}Q_{spe\ cat} - v_{cat})$ and

anode half-cells $U_{an}(\alpha_{an}Q_{spe\ an} - v_{an})$ by correcting for the separate capacity as shown below in Eq. 6.2 and Eq. 6.3:

$$\frac{dU_{pouch}}{dQ_{pouch}}(Q_{pouch}) = \frac{1}{\alpha_{cat}}\frac{dU_{cat}}{dQ_{spe\ cat}} - \frac{1}{\alpha_{an}}\frac{dU_{an}}{dQ_{spe\ an}} \qquad (6.2)$$

$$U_{pouch}(Q_{pouch}) = U_{cat}(\alpha_{cat}Q_{spe\ cat} - v_{cat}) - U_{an}(\alpha_{an}Q_{spe\ an} - v_{an}) \qquad (6.3)$$

where $Q_{spe\ cat}$ and $Q_{spe\ an}$ are the specific areal capacities of the cathode and anode half-cells, respectively, which can be determined from separate experiments on each type of coin half-cell. α_{cat} and α_{an} are the scaling factors for the cathode and anode to estimate the amount of active material in the anode and cathode of a pouch cell. v_{cat} and v_{an} are slippages or capacity-axis factors to adjust the corresponding capacities of half-cells with that of pouch cell so that satisfy each pair of points match well on the potential-curves under the specific voltage window. In this chapter, the pouch cell is comprised of 16 cathode (18.9cm×14.15cm) and 17 anode (19.2cm×14.5cm) sheets with the double coating and the traditional design of the anode excessing cathode in terms of area and capacity is adopted. Therefore, the factors α_{cat} and α_{an} are assumed are the same and estimated to be 18.9 cm x 14.15 cm x 16 x 2 = 8558 cm^2 =A because cathode with the small area and low capacity can represent the actual capacity of the fresh pouch cell. Then, 1.0A in cm^2 denotes 1.0 multiply A, showing that all area materials has been used. For the aged cell, a number less than 1 would be fitted and multiplied by the total area A to express the capacity change as the new scaling factors. Since the model is valid under equilibrium conditions, it is applied only to measurements obtained at a low current of C/25.

Table 6.3 shows the values of all parameters measured or fitted using the differential voltage and OCV analysis.

Table 6.3: List of parameters

Parameter	Symbol	Value			
		Fresh	**30days**	**120days**	**280days**
Capacity of pouch cell (Ah)	Q_{pouch}	14.97^m	12.67^m	10.67^m	8.10^m
Specific capacity of cathode (Ah cm^{-2})	$Q_{spe\ cat}$		0.00209^m		
Specific capacity of anode (Ah cm^{-2})	$Q_{spe\ an}$		0.00222^m		
Scaling factor of cathode/anode (cm^{-2})	α_{an}	$1.0\ A^{\,m}$	$0.9\ A^{\,f}$	$0.85\ A^{\,f}$	$0.685\ A^{\,f}$
Capacity-axis factor of cathode (Ah)	v_{cat}	$1.5^{\,f}$	$2.0^{\,f}$	$3.0^{\,f}$	$3.2^{\,f}$
Capacity-axis factor of anode (Ah)	v_{an}	$0.12^{\,f}$	$0.18^{\,f}$	$0.2^{\,f}$	$0.18^{\,f}$

^{m}: measured

^{f}: fitted

The results of discharge differential capacity curves and OCV fitting for the fresh and aged pouch cell are shown in Figure 6.11 and Figure 6.12, respectively.
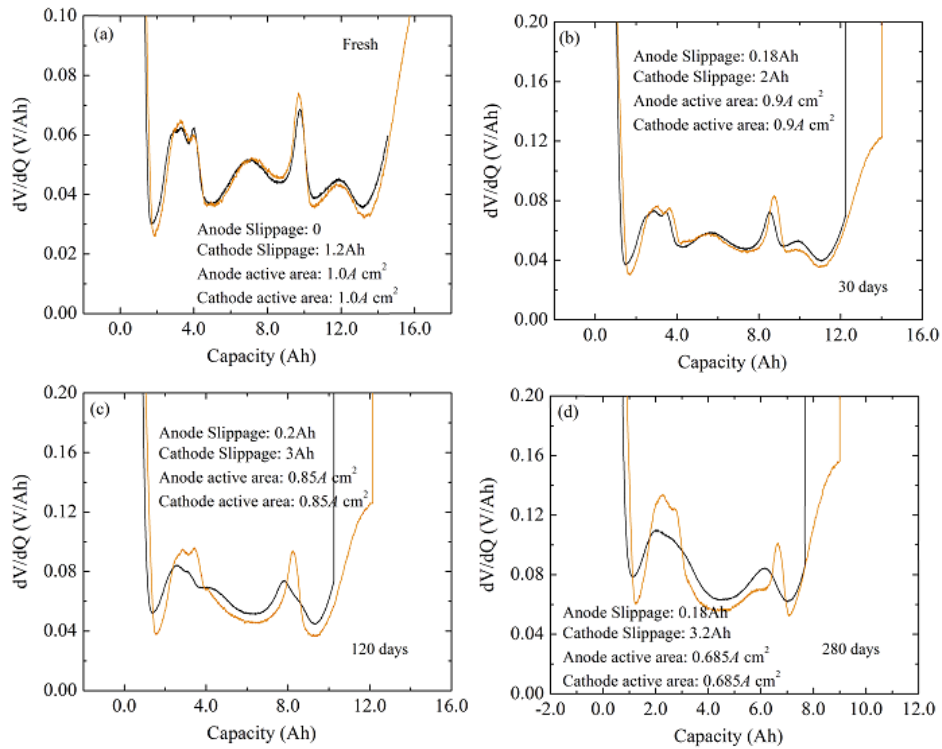
Figure 6.11: dV/dQ analysis (black line: Experimental, yellow line: Calculation based on Eq.2) for the aged pouch cell after (a) 0 days (b) 30 days (c) 120 days and (d) 280 days under 58℃ 100% SOC condition.

Figure 6.11 shows differential capacity analysis based on Eq. 6.2. The fit of calculated data to the measure data is much better for the small number of storage days, but it is still acceptable for the large storage days. Using the fitting parameters, voltages vs. capacity curves between the measured and calculated at various aging days are all marched very well (Figure 6.12). Note that there is a continue decrease in both active materials areas, and an increase in cathode slippage. These charges can be described in Figure 6.13.
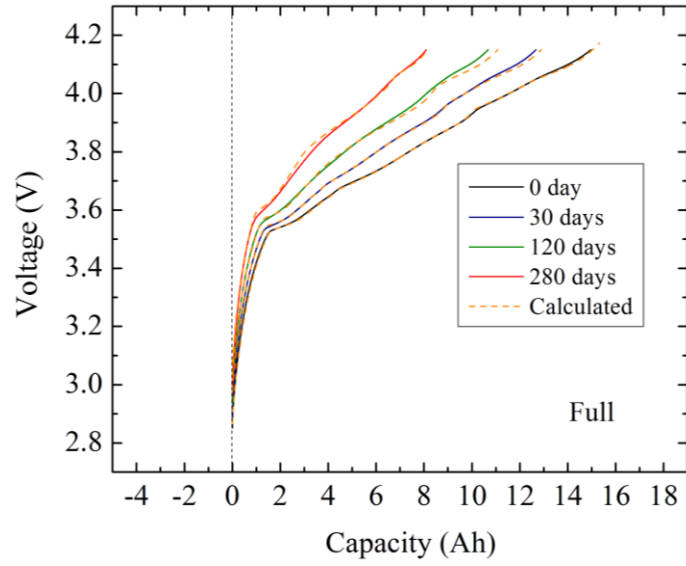
Figure 6.12: Comparison of experimental and calculated voltage-capacity curves fitted according to the differential voltage analysis for the aged pouch cell under 58℃ 100%SOC condition.
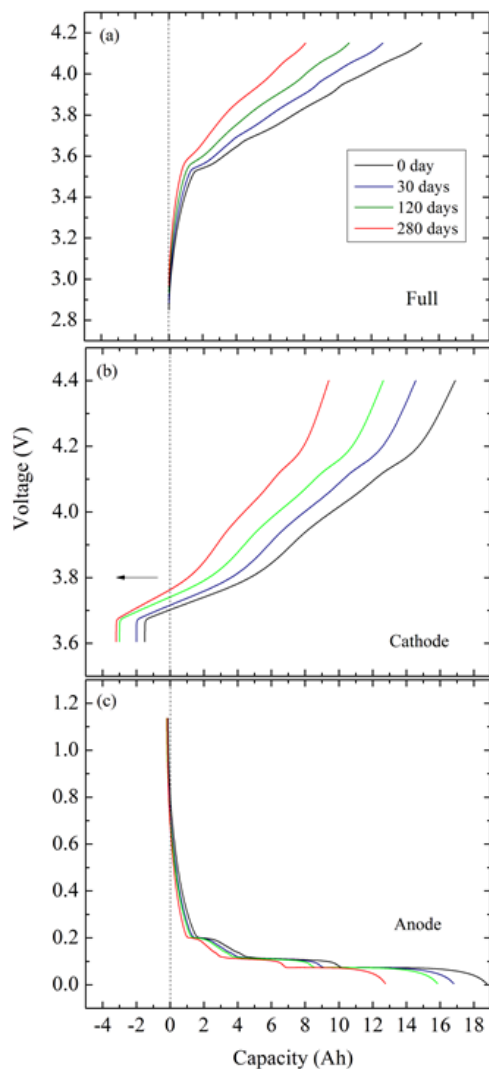
Figure 6.13: (a) Calculated voltage versus relative capacity for the aged pouch cell. (b) Cathode and (c) anode voltage vs. capacity as determined by the differential capacity analysis program.

Figure 6.13 shows the voltage vs. capacity graphs for the pouch cell (Figure 6.13a) as well as the cathode (Figure 6.13b) and anode (Figure 6.13c) half cells for the same cathode and anode electrodes. Q=0 denotes the fully discharge state of the pouch cell at each test. Through the

differential voltage analysis, the voltage vs. capacity curves for the cathode and anode have been scaled and slipped by the appropriate slippage and active areas. The active areas of electrode materials changes cause a shrinking or expansion of capacity range of reference voltage vs. capacity curves (cathode and anode). With the aging time going on, the scaling factor α decreases, which indicates the active materials cannot be utilized owing to the cycleable active lithium limiting as the above analyzed., even though they were not damaged based on the analysis of Figure 6.7 to Figure 6.9, For all tests, anode is almost fully emptied of Lithium and cathode is not completely filled at 0% SOC according to a tiny anode slippage. However, the cathode kept to slip to the higher absolute capacity, which can only occur if electrolyte oxidation is occurring [144]. Therefore, the electrolyte oxidation at cathode is a major side reaction to consume cycleable lithium for the high SOC storage cells.

6.3.3 Compression effect

When a commercial pouch cell is usually first manufactured, the space inside is filled with electrolyte and contains no gas, while the sealing package has a smooth surface. This was the condition of the fresh cells when we first observed them prior to storage. However, once the storage period began, gas bubbles could be clearly observed in all of the pouch cells. The amount of bubbles gradually increased as the cells were stored for longer and longer time. Moreover, more gas appeared to be generated when the storage temperature was raised from 38˚C to 58˚C. Thus, the largest amount of gas appeared in the fully charged cell stored for 280 days at 58℃ and caused the package surface to wrinkle when held between the fingers. Based on previous research, the composition of the gas is considered to include CO_2 CO and C_2H_4, which are the

products of side reactions. Agubra et al. [145] investigated electrolyte decomposition in lithium-ion batteries and the formation of thick films on the surface of the graphite particles, leading to the loss of cycleable lithium and the generation of CO_2 and C_2H_4. Belharouak et al. [146] also indicated that CO_2 and CO was produced by the decomposition of ethylene carbonate (EC) in the electrolyte and furthermore that the amount generated rose as the temperature was raised from 30°C to 60°C. In addition, Broussely et al. [143] concluded that side reactions, including electrolyte oxidation on highly charged cathode surfaces during storage at elevated temperature, could cause the cell impedance to increase, CO_2 to evolve and battery life to be reduced.

In order to investigate the effect of gas pressure on the performance of cell, we conducted non-destructive tests involving the force-loading of fully charged pouch cells aged at 58°C for 280 days according to the procedure described in the Experimental section. On the basis of charge and discharge curves obtained at C/25, the capacity was found to increase by almost 21% from 8.21 Ah when no pressure was applied to 9.92 Ah when 4 psi force was applied (Figure 6.14). However, no capacity change had been observed for the fresh cell in terms of C/5 C/2 1C to 3C between with and without 4 psi pressure. The large capacity rise demonstrated that the utilization of active materials in the aged pouch cell could be dramatically enhanced by the simple application of a non-destructive force. Furthermore, this improvement in utilization was evident in two ways: i) the available SOC windows or stoichiometries of both the cathode and anode materials broadened and ii) the percentage of the available amount of active material increased. However, once the capacity was normalized using self-capacity. the two pairs of charge-discharge curves corresponding to the two test cases were found to overlap almost entirely, as shown in Figures 15a and 15b. This demonstrated that the form of charge-discharge curves had

almost no change, i.e., relationship between potential and SOC window did not change and that

the improvement of capacity under force loading could be attributed only to an increase in the

amount of available active material.
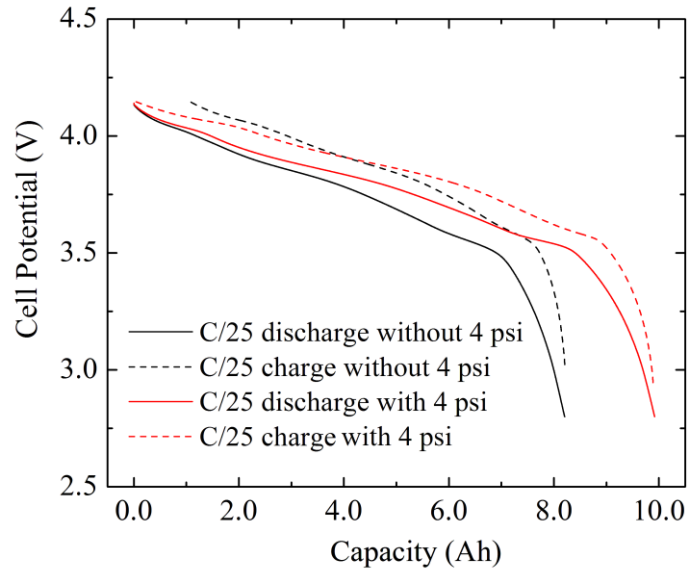
Figure 6.14: Comparison of charge-discharge curves obtained at the rate of C/25 with and

without the application of 4 psi pressure on a pouch cell previously aged by storage for 280 days
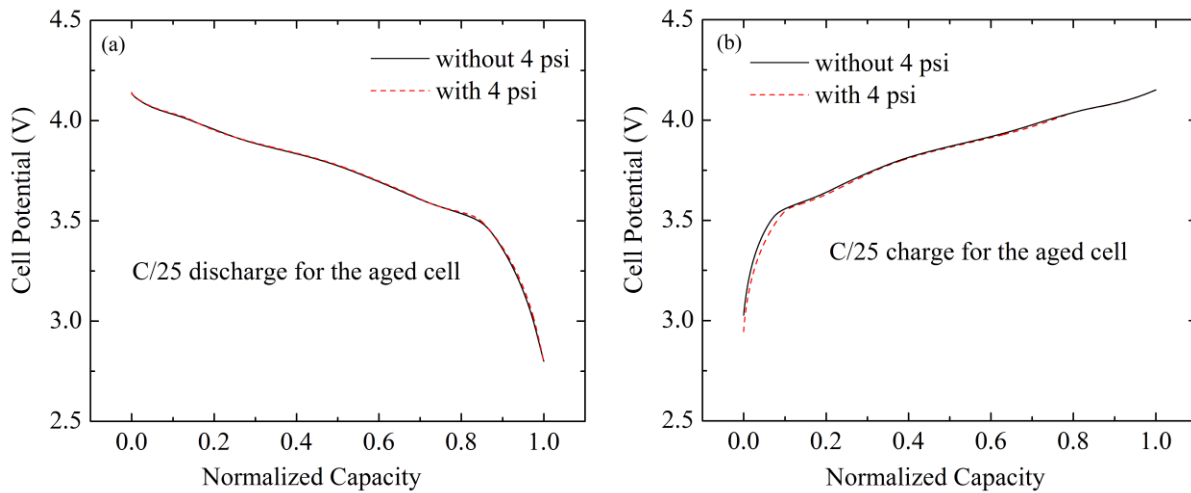
at 58˚C.

Figure 6.15: Comparison of potential-normalized capacity curves obtained during (a) discharge and (b) charge at a rate of C/25 with and without the application of 4 psi pressure on a pouch cell previously aged by storage for 280 days at 58°C.

Through differential voltage analysis and OCV comparison of the pair of discharge performance, the fitted results showed that the scaling factors increased to 0.70A, compared to the value of 0.60A when no pressure was applied, reflecting an increase in the available active material area.

As described in the Experimental section, we also conducted an experiment in which the pressure was adjusted in 9 steps and the discharge capacity at C/25 was measured after each step. A comparison of the potential-capacity curves and the capacity at the end-of-discharge measured at each pressure is presented in Figures 6.16a and 6.16b, respectively. When the load is first increased from 0 to 4.0 psi pressure, the measured capacity of the pouch cell jumped from 8.2 Ah to 9.9 Ah. Over the subsequent 5 steps, the capacity more gradually increased to 10.5 Ah although the pressure was increased first but then decreased. Over the last 4 steps, the discharge

149

capacity decreased as the force-loading pressure was reduced, especially after the last stage when the pressure was dropped from 1.0 psi to 0 psi. In fact, the measured capacity returned to its original value of ~8.2-8.5 Ah when the pressure was decreased back to 0 psi at which the experiment was started. This suggests that no permanent change in the discharge capacity was observed when the pressure on the aged pouch cell was turned off. At the same time, this experiment confirmed that the capacity could be significantly improved by the application of a pressure to the cell, even a level as small as 1 psi. It is noted that the capacity measurement under various pressures has been adopted here first time.
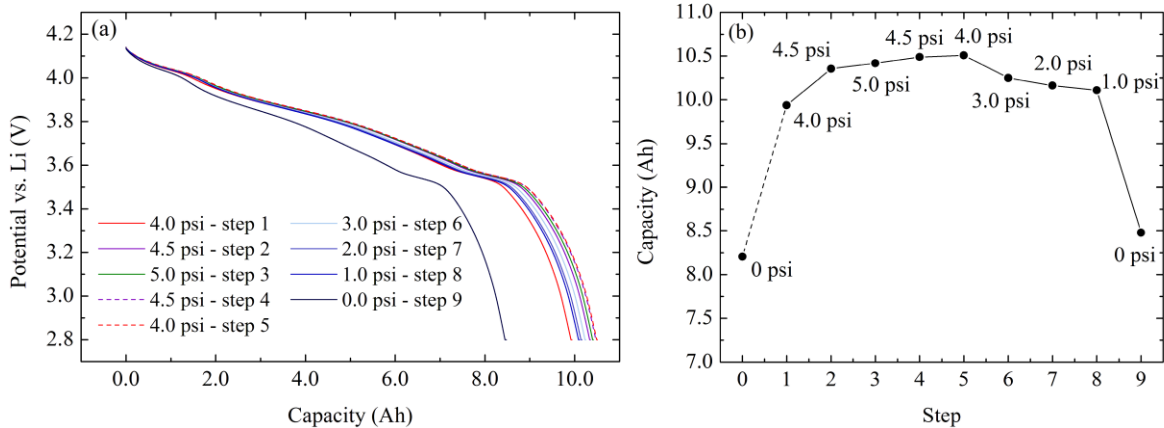
Figure 6.16: (a) Discharge potential-capacity curves and (b) capacity at the end of discharge measured at C/25 at each pressure applied in the sequence of 9 steps on the fully charged pouch cell aged for 280 days at 58°C.

This effect of pressure is illustrated in the schematic diagram of the cross-section of an aged pouch cell in Figure 6.17. Figure 6.17a corresponding to the situation when no pressure is applied shows gas bubbles distributed throughout the cell, including the separators and

150

electrodes, interfaces between electrodes and separators and between the Jelly Roll (J/R) and

sealing package bag. This distribution of gas bubbles could block some of the connections, such

as at electrolyte/active material interfaces, and cause the resistance to ionic and electronic

transfer to rise, utilization of active materials to decrease and the pouch cell capacity to be

lowered. The DCIR curves in Figure 18 showed that an improved pulse voltage curves for the

same cell under 4 psi pressure, comparing with that without pressure. Once pressure is applied to

the pouch cell, most gas bubbles inside the cell would be squeezed out into the outer region at

the interface between the J/R and sealing package bag where they would have little effect on the

operation of the cell (Figure 6.17b). Therefore, no matter how much force is loaded on the pouch

cell, it should be sufficient to displace the gas from key contact points and increase the measured

capacity of the pouch cell. In addition, a high force load may improve the connections between

the various cell components and cell operation.
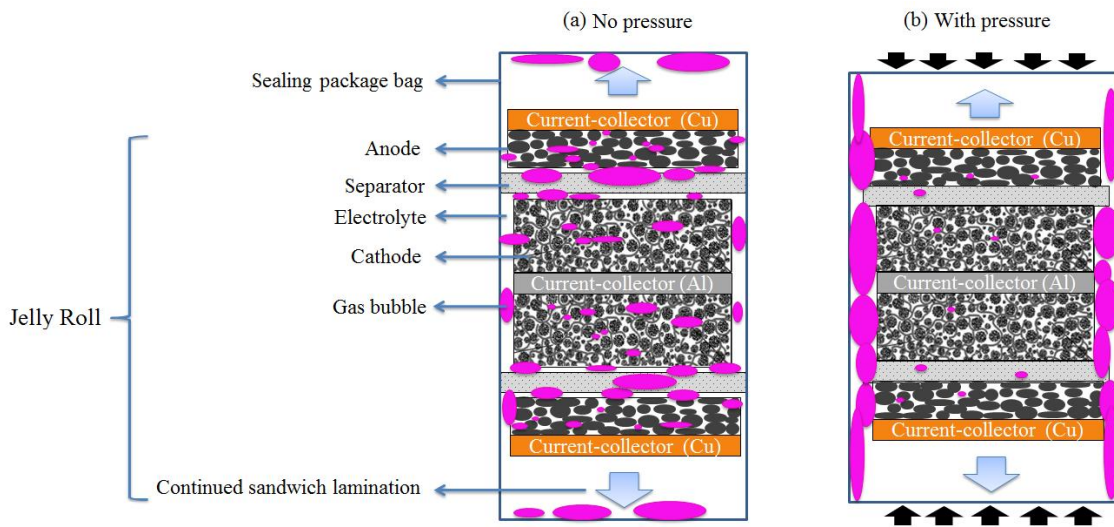
Figure 6.17: Schematic diagram of the cross section of the aged pouch cell (a) without force-

loading and (b) with force-loading.

151
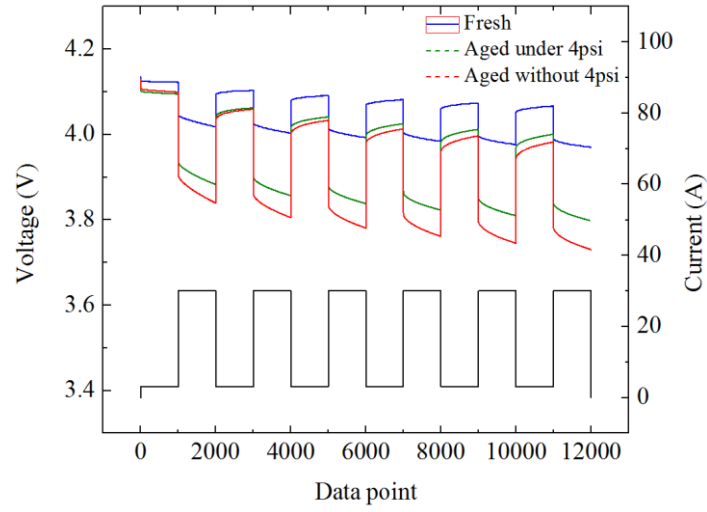
Figure 6.18: Comparison of galvanostatic pulse discharge curves between with and without 4 psi pressure for 280 days at 58˚C.

Chapter 7 Conclusions and suggestions for future work

7.1 Conclusions and Summary

In this work an effective method for composition estimation of blended cathodes of Li-ion cells is proposed and validated for a NMC-LMO blended cathode. The method consists of two main steps. In the first step, SEM/EDX analysis and the differential capacity signature of an electrode sample are used to identify the active materials. A physics-based model is then used to simulate the electrode discharge at a very low current (e.g. C/25) and compare to the experimental discharge profile in order to estimate the electrode composition. The model prediction is found to be in excellent agreement with the composition obtained from an independent, non-electrochemical experimental technique, i.e., powder X-ray diffraction of the identified commercial compounds.

For the identified commercial NMC-LMO blended cathode, a mathematical model has been implemented to describe its performance. The model features particles with different sizes and chemical composition. More specifically, the electrode is loaded with two different active materials NMC and LMO. Since NMC forms agglomerates, it is sub-divided into 2 classes of particles, i.e., primary particles and secondary particles. The secondary particles are considered to be large non-porous NMC agglomerates. Particle size distributions (PSDs) for the LMO particles, NMC primary and NMC secondary particles were obtained from SEM micrographs with the resulting d_{50}s used in the model. Expressions describing the dependence of the equilibrium potentials of NMC and LMO on the lithium concentration were fitted assuming that they can be obtained from the average of the potentials measured during charge and discharge at

the low rate of C/25. The effective electronic conductivity of the active materials was measured using a 4-point probe setup and its impact on the electrode potential estimated by dimensional analysis of Ohm's law. The model also features variable solid-state diffusivity and treats the transport of intercalated species across active material particles in a thermodynamically consistent manner. The model has been shown to accurately capture the galvanostatic discharge data as well as the differential-capacity curves obtained from a blended NMC (70 wt%): LMO (30 wt%) cathode at various C-rates. This indicates that the assumption of nonporous secondary particles is reasonable at least over the operating condition of interest in this study, i.e., up to 2C applied current. This significantly simplifies the model and relaxes the need for characterizing the actual porous particles.

Adopting the multi-particle mathematical model, six sets of discharge Galvanostatic Intermittent Titration Technique (GITT) curves with varying pulse currents and relaxation periods have been simulated in a NMC-LMO blended lithium-ion electrode. The simulation results show that the model is applicable for all cases and more accurate for the case of small current pulse discharge rate with a longer relaxation time. An analysis of the current contribution and surface lithium stoichiometry of each component reveals that a complex interaction between the two active materials NMC and LMO and between micron and submicron NMC particles occurs during electrode operation. It has a balancing effect on the lithium concentration at the surfaces of LMO and NMC particles. The present analysis suggests that such interaction arises mainly from thermodynamic factors where the potentials of the two components are driven away from (or toward) a common equilibrium potential during discharge or rest periods.

In addition, the multi-particle mathematical model has been used to analyze the charge/discharge asymmetry observed in the rate capability of an NMC-LMO blended cathode. A comparative study of the differential capacity curves on charge and discharge at different currents levels shows that the asymmetry in the contribution of each component (i.e., LMO or NMC) during charge and discharge at medium to high C-rates is at the heart of electrode charge/discharge asymmetry. It is observed that the capacity contribution of LMO (relative to the total end-of-charge or -discharge capacity at a given rate) increases during discharge when the current is raised, but decreases during charge for a similar change in C-rate. Based on the model and experiment analysis presented in this paper, the observed asymmetry is attributed to a combination of the following factors: i) difference in the equilibrium potentials of the two components as functions of stoichiometry, ii) composition of the blended electrode, iii) solid-state diffusion and kinetics limitations which differ for the two components. The first and the second factors together cause an asymmetry in the availability of intercalation sites in the two components toward the end of charge and discharge, while the third factor lead to a difference in the dynamic performance of the electrode during charge and discharge.

At the last part of this work, , the calendar life of a commercial pouch cell consisting of a NMC-LMO blended cathode and graphite anode and the degradation of an aged cell have been investigated through a series of pouch cell tests, coin cell tests and OCV modeldifferential voltage analysis. In addition, the effect of pressure on an aged pouch cell has been studied. The calendar life of pouch cells was assessed under the following four conditions depending on its SOC and storage temperature: 0% SOC at 35℃, 0% SOC at 58℃, 100% SOC at 35℃ and 100% SOC at 58℃. The conditions at the lower storage temperature and SOC are considered to

be moderate for the cells, while storage at the higher temperature and SOC are sufficient to accelerate the degradation of the capacity at all four rates of C/5, C/2, 1C and 2C. Not surprisingly, the fully charged pouch cell aged at 58℃ exhibited the most rapid degradation so that the percent capacity remaining after 280 days of storage dropped to 55% and the DCIR increased to 6.2 mΩ from the level of 2.4 mΩ measured prior to aging. The research on a degradation mechanism for the aged pouch cell showed that the loss of cycleable lithium leading to the formation of a passivation layer on the surface of the graphite anode and generation of gas is the predominant reason for the capacity loss. The simulation results of the OCV model revealed that about 40% of the active material was not used in the aged pouch cell. The study on the effect of pressure on the aged pouch cell showed that a large increase in capacity could be achieved if a force was loaded on the aged cell. It is most likely that this loading changed the distribution of gas bubbles inside the pouch cell by squeezing the gas from locations where it could hinder the transfer of species to the outer regions where it has little effect on cell operation and performance. Therefore, the utilization of active materials can be enhanced. The fitting of the differential voltage analysis to the experimental data indicated that the amount of active material could be improved by 10% compared with that utilized in the absence of an applied pressure.

This work can be used for analysis of blended cathode Li-ion battery degradation studies as well as the development of cathode blends for specific applications and duty cycles.

7.2 Recommendations

For the current and future work, several suggestions and recommendations are proposed as the following shows:

1. In the materials aspect, the phase transition mechanisms and the interactions between species in the lattice of each component should be further investigated to develop a more detailed understanding. Specifically, some significant experimental phenomona such as the interplay between active materials in a blended electrode should be studied in depth, so as to develop a practial-based physical model which is described by combined materials science, engineering theory and their interdisciplinary science.

2. Then, a multi-scale mathematical model, concerning ionic and electronic transfers in the single particle, in the porous cluster, and in the electrode level can be developed. Although the model would be much complicated, compared to the presented multi-particle model, it can depict a coherent picture for the entire electrochemcial reaction process and provide a distinct understanding for the rate-limitation factors under the varying operation conditions.

3. In terms of life study, a cycle life of the commercial blended pouch cell, considering capacity-power fade mechanisms under different accelerated factors, i.e. SOC window, C-rate and operating temperture, could be investigated using some experimental analysis approaches in the future work. This will be a significant supplement for the entire combined-calendar life study.

4. A mathematical model to describe life degradation and predict life of the 15Ah commercial blended-cathode pouch cell could be developed. It will be useful tool to evaluate the avalible life,

adaptive control strategies to perserve life and develop new cell-designed technologies with a superior performance.

References

[1]   Ngô, C., & Natowitz, J. (2016). Our energy future: resources, alternatives and the
       environment. John Wiley & Sons.

[2]   Höök, M., & Tang, X. (2013). Depletion of fossil fuels and anthropogenic climate
       change—A review. *Energy Policy, 52*, 797-809.

[3]   Armand, M., & Tarascon, J. M. (2008). Building better batteries. *Nature, 451(7179),* 652-
       657.

[4]   Gonzalez, C. (2015). Lithium-ion power for data storage and servers. Retrieved April 8,
       2015, from http://www.datacenterjournal.com/lithiumion-power-data-storage-servers/.

[5]   Chang, J., Huang, X., Zhou, G., Cui, S., Hallac, P. B., Jiang, J., ... & Chen, J. (2014).
       Multilayered Si nanoparticle/reduced graphene oxide hybrid as a high-performance
       lithium-ion battery anode. *Advanced Materials*, 26(5), 758-764.

[6]   Bizeray, A. (2013). Electric Vehicles - Using physics-based battery models for an
       improved estimation of state of charge. Retrieved June 2, 2013, from
       http://epg.eng.ox.ac.uk/content/electric-vehicles-using-physics-based-battery-models-
       improved-estimation-state-charge.

[7]   Farkhondeh, M. (2012). Model-assisted performance analysis of commercial LiFePO$_4$-
       based Li-ion batteries including thermal effects and aging. Waterloo, ON: University of
       Waterloo. Retrieved December, 2012 from comprehensive examination.

[8]   Tarascon, J. M., & Armand, M. (2001). Issues and challenges facing rechargeable lithium batteries. *Nature, 414(6861),* 359-367.

[9]   Cheng, F., Wang, H., Zhu, Z., Wang, Y., Zhang, T., Tao, Z., & Chen, J. (2011). Porous $LiMn_2O_4$ nanorods with durable high-rate capability for rechargeable Li-ion batteries. *Energy & Environmental Science, 4(9),* 3668-3675.

[10]   Cao, F., & Prakash, J. (2002). A comparative electrochemical study of $LiMn_2O_4$ spinel thin-film and porous laminate. *Electrochimica Acta, 47(10),* 1607-1613.

[11]   Totir, D. A., Cahan, B. D., & Scherson, D. A. (1999). Electrochemical characterization of lithiated transition metal oxide cathode particles in the absence of carbon, binders and other additives. *Electrochimica Acta, 45(1)*, 161-166.

[12]   Dokko, K., Nishizawa, M., Mohamedi, M., Umeda, M., Uchida, I., Akimoto, J., ... & Mizuta, S. (2001). Electrochemical studies of Li-Ion extraction and insertion of $LiMn_2 O_4$ single crystal. *Electrochemical and Solid-State Letters, 4(9)*, A151-A153.

[13]   Nishizawa, M., Uchiyama, T., Dokko, K., Yamada, K., Matsue, T., & Uchida, I. (1998). Electrochemical studies of spinel $LiMn_2O_4$ films prepared by electrostatic spray deposition. *Bulletin of the Chemical Society of Japan, 71(8),* 2011-2015.

[14]   Mohamedi, M., Takahashi, D., Uchiyama, T., Itoh, T., Nishizawa, M., & Uchida, I. (2001). Explicit analysis of impedance spectra related to thin films of spinel $LiMn_2O_4$. *Journal of Power Sources, 93(1),* 93-103.

[15] Mohamedi, M., Takahashi, D., Itoh, T., Umeda, M., & Uchida, I. (2002). ESD fabricated thin films of spinel LiMn$_2$O$_4$ for lithium microbatteries: I. effects of thickness. *Journal of The Electrochemical Society, 149(1),* A19-A25.

[16] Deiss, E., Häringer, D., Novak, P., & Haas, O. (2001). Modeling of the charge–discharge dynamics of lithium manganese oxide electrodes for lithium-ion batteries. *Electrochimica Acta, 46(26),* 4185-4196.

[17] Nishizawa, M., Ise, T., Koshika, H., Itoh, T., & Uchida, I. (2000). Electrochemical In-Situ conductivity measurements for thin film of Li$_{1-x}$Mn$_2$O$_4$ spinel. *Chemistry of Materials, 12(5),* 1367-1371.

[18] Yamamura, S., Koshika, H., Nishizawa, M., Matsue, T., & Uchida, I. (1998). In situ conductivity measurements of LiMn$_2$O$_4$ thin films during lithium insertion/extraction by using interdigitated microarray electrodes. *Journal of Solid State Electrochemistry, 2(4),* 211-215.

[19] Wu, S. L., Zhang, W., Song, X., Shukla, A. K., Liu, G., Battaglia, V., & Srinivasan, V. (2012). High rate capability of Li (Ni$_{1/3}$Mn$_{1/3}$Co$_{1/3}$)O$_2$ electrode for Li-ion batteries. *Journal of The Electrochemical Society, 159(4),* A438-A444.

[20] Kabi, S., & Ghosh, A. (2010). Polaron conduction in Lix [Ni$_{1/3}$Mn$_{1/3}$Co$_{1/3}$] O$_{2-\delta}$ (x= 1, 0.9 and δ= 0, 0.05) cathodes. *Journal of Applied Physics, 107(10),* 103715.

[21] Wang, L., Zhao, J. S., He, X. M., Gao, J., Li, J. J., Wan, C. R., & Jiang, C. Y. (2012). Electrochemical impedance spectroscopy (EIS) study of $LiNi_{1/3}Co_{1/3}Mn_{1/3}O_2$ for Li-ion batteries. *Int. J. Electrochem. Sci, 7(1),* 345-353.

[22] Barker, J., Pynenburg, R., Koksbang, R., & Saidi, M. Y. (1996). An electrochemical investigation into the lithium insertion properties of Li_xCoO_2. *Electrochimica Acta, 41(15),* 2481-2488.

[23] Aurbach, D., Levi, M. D., Levi, E., Teller, H., Markovsky, B., Salitra, G., & Heider, L. (1998). Common electroanalytical behavior of Li intercalation processes into graphite and transition metal oxides. *Journal of The Electrochemical Society, 145(9),* 3024-3034.

[24] Levi, M. D., Salitra, G., Markovsky, B., Teller, H., Aurbach, D., Heider, U., & Heider, L. (1999). Solid‐State Electrochemical kinetics of Li-ion Intercalation into $Li_{1-x}CoO_2$: simultaneous application of electroanalytical techniques SSCV, PITT, and EIS. *Journal of The Electrochemical Society, 146(4),* 1279-1289.

[25] Striebel, K. A., Deng, C. Z., Wen, S. J., & Cairns, E. J. (1996). Electrochemical behavior of $LiMn_2O_4$ and $LiCoO_2$ thin films produced with pulsed laser deposition. *Journal of the Electrochemical Society, 143(6),* 1821-1827.

[26] Cao, Q., Zhang, H. P., Wang, G. J., Xia, Q., Wu, Y. P., & Wu, H. Q. (2007). A novel carbon-coated $LiCoO_2$ as cathode material for lithium ion battery. *Electrochemistry Communications, 9(5),* 1228-1232.

[27] Levasseur, S., Menetrier, M., Suard, E., & Delmas, C. (2000). Evidence for structural defects in non-stoichiometric HT-LiCoO$_2$: electrochemical, electronic properties and 7 Li NMR studies. *Solid State Ionics, 128(1),* 11-24.

[28] Ménétrier, M., Saadoune, I., Levasseur, S., & Delmas, C. (1999). The insulator-metal transition upon lithium deintercalation from LiCoO$_2$: electronic properties and 7Li NMR study. *Journal of Materials Chemistry, 9(5),* 1135-1140.

[29] Imanishi, N., Fujiyoshi, M., Takeda, Y., Yamamoto, O., & Tabuchi, M. (1999). Preparation and 7 Li-NMR study of chemically delithiated Li$_{1-x}$CoO$_2$ (0< x< 0.5). *Solid State Ionics, 118(1),* 121-128.

[30] Morgan, D., Van der Ven, A., & Ceder, G. (2004). Li conductivity in Li$_x$MPO$_4$ (M= Mn, Fe, Co, Ni) olivine materials. *Electrochemical and Solid-state Letters, 7(2),* A30-A32.

[31] Franger, S. F. L. C., Le Cras, F., Bourbon, C., & Rouault, H. (2002). LiFePO$_4$ synthesis routes for enhanced electrochemical performance. *Electrochemical and Solid-State Letters, 5(10),* A231-A233.

[32] Prosini, P. P., Lisi, M., Zane, D., & Pasquali, M. (2002). Determination of the chemical diffusion coefficient of lithium in LiFePO$_4$. *Solid State Ionics, 148(1),* 45-51.

[33] Denis, Y. W., Fietzek, C., Weydanz, W., Donoue, K., Inoue, T., Kurokawa, H., & Fujitani, S. (2007). Study of LiFePO$_4$ by cyclic voltammetry. *Journal of the Electrochemical Society, 154(4),* A253-A257.

[34]   Safari, M., & Delacourt, C. (2011). Mathematical modeling of lithium iron phosphate electrode: galvanostatic charge/discharge and path dependence. *Journal of The Electrochemical Society, 158(2),* A63-A73.

[35]   Farkhondeh, M., & Delacourt, C. (2011). Mathematical modeling of commercial $LiFePO_4$ electrodes based on variable solid-state diffusivity. *Journal of The Electrochemical Society, 159(2),* A177-A192.

[36]   Zaghib, K., Mauger, A., Goodenough, J. B., Gendron, F., & Julien, C. M. (2007). Electronic, optical, and magnetic properties of $LiFePO_4$: small magnetic polaron effects. *Chemistry of Materials, 19(15),* 3740-3747.

[37]   Herle, P. S., Ellis, B., Coombs, N., & Nazar, L. F. (2004). Nano-network electronic conduction in iron and nickel olivine phosphates. *Nature Materials, 3(3),* 147-152

[38]   Delacourt, C., Wurm, C., Laffont, L., Leriche, J. B., & Masquelier, C. (2006). Electrochemical and electrical properties of Nb-and/or C-containing $LiFePO_4$ composites. *Solid State Ionics, 177(3),* 333-341.

[39]   Xu, B., Qian, D., Wang, Z., & Meng, Y. S. (2012). Recent progress in cathode materials research for advanced lithium ion batteries. *Materials Science and Engineering: R: Reports, 73(5),* 51-65.

[40]   Y. Yao. (2008). A study of electro materials for lithium-ion batteries. Wollongong, Australie: University of Wollongong. Retrieved November 13, 2008 from http://ro.uow.edu.au/theses/88/.

[41] Thackeray, M. M., David, W. I. F., Bruce, P. G., & Goodenough, J. B. (1983). Lithium insertion into manganese spinels. *Materials Research Bulletin, 18(4),* 461-472..

[42] Jang, D. H., Shin, Y. J., & Oh, S. M. (1996). Dissolution of Spinel Oxides and Capacity Losses in 4 V Li/Li$_x$Mn$_2$O$_4$ Cells. *Journal of The Electrochemical Society, 143(7),* 2204-2211.

[43] Jang, D. H., & Oh, S. M. (1997). Electrolyte Effects on Spinel Dissolution and Cathodic Capacity Losses in 4 V Li/Li$_x$Mn$_2$O$_4$ Rechargeable Cells. *Journal of The Electrochemical Society, 144(10),* 3342-3348.

[44] Jang, D. H., & Oh, S. (1998). Effects of carbon additives on spinel dissolution and capacity losses in 4V Li/Li$_x$Mn$_2$O$_4$ rechargeable cells. *Electrochimica Acta, 43(9),* 1023-1029.

[45] Aurbach, D., Talyosef Y., Markovsky B., Markevich, E., Zinigrad, E., Asraf L., Gnanaraj J. S. & Kim H. J. (2004). Design of electrolyte solutions for Li and Li-ion batteries: a review. *Electrochimica Acta,, 50(2),* 247-254.

[46] Vetter, J., Novák, P., Wagner, M. R., Veit, C., Möller, K. C., Besenhard, J. O., ... & Hammouche, A. (2005). Ageing mechanisms in lithium-ion batteries. *Journal of Power Sources, 147(1),* 269-281.

[47] Benedek, R., & Thackeray, M. M. (2006). Reaction energy for LiMn$_2$O$_4$ spinel dissolution in acid. *Electrochemical and Solid-state Letters, 9(6),* A265-A267.

[48]   Dai, Y., Cai, L., & White, R. E. (2013). Capacity fade model for spinel $LiMn_2O_4$

   electrode. *Journal of The Electrochemical Society, 160(1),* A182-A190.

[49]   Amine, K., Liu, J., Kang, S., Belharouak, I., Hyung, Y., Vissers, D., & Henriksen, G.

   (2004). Improved lithium manganese oxide spinel/graphite Li-ion cells for high-power

   applications. *Journal of Power Sources, 129(1),* 14-19.

[50]   Smith, A. J., Smith, S. R., Byrne, T., Burns, J. C., & Dahn, J. R. (2012). Synergies in

   blended $LiMn_2O_4$ and Li $[Ni_{1/3}Mn_{1/3}Co_{1/3}]$ O_2 positive electrodes. *Journal of The*

   Electrochemical Society, 159(10), A1696-A1701.

[51]   Lancashire, R. J. (2014). The Jahn-Teller Theorem. Kingston, Jamaica: University of the

   West Indies. Retrieved September 10, 2014 from

   http://wwwchem.uwimona.edu.jm/courses/JahnTeller.html.

[52]   Thackeray, M. M., Shao‑Horn, Y., Kahaian, A. J., Kepler, K. D., Skinner, E., Vaughey,

   J. T., & Hackney, S. A. (1998). Structural Fatigue in Spinel Electrodes in High Voltage

   (4 V) $Li/Li_xMn_2O_4$ Cells. *Electrochemical and Solid-State Letters, 1(1),* 7-9.

[53]   Gummow, R. J., De Kock, A., & Thackeray, M. M. (1994). Improved capacity retention

   in rechargeable 4 V lithium/lithium-manganese oxide (spinel) cells. *Solid State Ionics,*

   69(1), 59-67.

[54]   Thackeray, M. M. (1995). Structural considerations of layered and spinel lithiated oxides

   for lithium ion batteries. *Journal of The Electrochemical Society, 142(8),* 2558-2563.

166

[55] MacNeil, D. D., Lu, Z., & Dahn, J. R. (2002). Structure and Electrochemistry of Li [Ni$_x$ Co$_{1-2x}$Mn$_x$] O$_2$ ($0 \leqslant x \leqslant 1/2$). *Journal of The Electrochemical Society*, 149(10), A1332-A1336.

[56] Ohzuku, T., & Makimura, Y. (2001). Layered Lithium Insertion Material of LiCo$_{1/3}$Ni$_{1/3}$Mn$_{1/3}$O$_2$ for Lithium-Ion Batteries. *Chemistry Letters, (7),* 642-643.

[57] Hwang, B. J., Tsai, Y. W., Carlier, D., & Ceder, G. (2003). A combined computational/experimental study on LiNi$_{1/3}$Co$_{1/3}$Mn$_{1/3}$O$_2$. *Chemistry of Materials, 15(19),* 3676-3682.

[58] Koyama, Y., Tanaka, I., Adachi, H., Makimura, Y., & Ohzuku, T. (2003). Crystal and electronic structures of superstructural Li$_{1-x}$[Co$_{1/3}$Ni$_{1/3}$Mn$_{1/3}$]O$_2$ ($0 \leqslant x \leqslant 1$). *Journal of Power Sources, 119*, 644-648.

[59] Choi, J., & Manthiram, A. (2005). Role of Chemical and Structural Stabilities on the Electrochemical Properties of Layered LiNi$_{1/3}$Mn$_{1/3}$Co$_{1/3}$O$_2$ Cathodes. *Journal of The Electrochemical Society, 152(9),* A1714-A1718.

[60] Zeng, Y. W. (2008). Investigation of LiNi$_{1/3}$Mn$_{1/3}$Co$_{1/3}$O$_2$ cathode particles after 300 discharge/charge cycling in a lithium-ion battery by analytical TEM. *Journal of Power Sources, 183(1),* 316-324.

[61] Kitao, H., Fujihara, T., Takeda, K., Nakanishi, N., & Nohma, T. (2005). High-temperature storage performance of Li-ion batteries using a mixture of Li-Mn spinel and Li-Ni-Co-

Mn oxide as a positive electrode material. *Electrochemical and Solid-state Letters, 8(2),* A87-A90.

[62]   Jeong, S. K., Shin, J. S., Nahm, K. S., Kumar, T. P., & Stephan, A. M. (2008). Electrochemical studies on cathode blends of $LiMn_2O_4$ and Li [$Li_{1/15}Ni_{1/5}Co_{2/5}Mn_{1/3}O_2$]. *Materials Chemistry and Physics, 111(2),* 213-217.

[63]   Kobayashi, T., Kawasaki, N., Kobayashi, Y., Shono, K., Mita, Y., & Miyashiro, H. (2014). A method of separating the capacities of layer and spinel compounds in blended cathode. *Journal of Power Sources, 245,* 1-6.

[64]   Arora, P., White, R. E., & Doyle, M. (1998). Capacity fade mechanisms and side reactions in lithium‐ion batteries. *Journal of the Electrochemical Society, 145(10),* 3647-3667.

[65]   Aurbach, D., Markovsky, B., Weissman, I., Levi, E., & Ein-Eli, Y. (1999). On the correlation between surface chemistry and performance of graphite negative electrodes for Li ion batteries. *Electrochimica Acta, 45(1),* 67-86.

[66]   Christensen, J., & Newman, J. (2004). A mathematical model for the lithium-ion negative electrode solid electrolyte interphase. *Journal of The Electrochemical Society, 151(11),* A1977-A1988.

[67]   Aurbach, D., Zinigrad, E., Cohen, Y., & Teller, H. (2002). A short review of failure mechanisms of lithium metal and lithiated graphite anodes in liquid electrolyte solutions. *Solid State Ionics, 148(3),* 405-416.

[68]   Mao, Z. (2011).Commercial 18650 Lithium-ion battery failure mode, Tianjin: Lishen Inc.

[69]   Goodenough, J. B., & Park, K. S. (2013). The Li-ion rechargeable battery: a perspective. *Journal of the American Chemical Society, 135(4),* 1167-1176.

[70]   Gao, J., & Manthiram, A. (2009). Eliminating the irreversible capacity loss of high capacity layered Li [$Li_{0.2}Mn_{0.54}Ni_{0.13}Co_{0.13}$]$O_2$ cathode by blending with other lithium insertion hosts. *Journal of Power Sources, 191(2),* 644-647.

[71]   Tran, H. Y., Täubert, C., Fleischhammer, M., Axmann, P., Küppers, L., & Wohlfahrt-Mehrens, M. (2011). $LiMn_2O_4$ spinel/$LiNi_{0.8}Co_{0.15}Al_{0.05}O_2$ blends as cathode materials for lithium-ion batteries. *Journal of The Electrochemical Society, 158(5),* A556-A561.

[72]   Lee, K. S., Myung, S. T., Kim, D. W., & Sun, Y. K. (2011). AlF_3-coated $LiCoO_2$ and Li [$Ni_{1/3}Mn_{1/3}Co_{1/3}O_2$] O 2 blend composite cathode for lithium ion batteries. *Journal of Power Sources, 196(16),* 6974-6977.

[73]   Albertus, P., Christensen, J., & Newman, J. (2009). Experiments on and modeling of positive electrodes with multiple active materials for lithium-ion batteries. *Journal of the Electrochemical Society, 156(7),* A606-A618.

[74]   Chikkannanavar, S. B., Bernardi, D. M., & Liu, L. (2014). A review of blended cathode materials for use in Li-ion batteries. *Journal of Power Sources, 248,* 91-100.

[75]   Newman, J., Thomas, K. E., Hafezi, H., & Wheeler, D. R. (2003). Modeling of lithium-ion batteries. *Journal of Power Sources, 119,* 838-843.

[76]   Newman, J. (1995). Optimization of porosity and thickness of a battery electrode by means of a reaction‑zone model. *Journal of the Electrochemical Society, 142(1),* 97-101.

[77]   Stewart, S., & Newman, J. (2008). Measuring the salt activity coefficient in lithium-

battery electrolytes. *Journal of The Electrochemical Society, 155(6),* A458-A463.

[78]   Delacourt, C., & Safari, M. (2012). Life simulation of a graphite/LiFePO$_4$ cell under

cycling and storage. *Journal of The Electrochemical Society, 159(8),* A1283-A1291.

[79]   Jung, S. (2014). Mathematical model of lithium-ion batteries with blended-electrode

system. *Journal of Power Sources, 264,* 184-194.

[80]   Dai, Y., Cai, L., & White, R. E. (2014). Simulation and analysis of stress in a Li-ion

battery with a blended LiMn$_2$O$_4$ and LiNi$_{0.8}$Co$_{0.15}$Al$_{0.05}$O$_2$ cathode. *Journal of Power*

Sources, 247, 365-376.

[81]   Schmidt, J. P., Tran, H. Y., Richter, J., Ivers-Tiffée, E., & Wohlfahrt-Mehrens, M. (2013).

Analysis and prediction of the open circuit potential of lithium-ion cells. *Journal of*

Power Sources, 239, 696-704.

[82]   Santhanagopalan, S., Guo, Q., Ramadass, P., & White, R. E. (2006). Review of models for

predicting the cycling performance of lithium ion batteries. *Journal of Power Sources,*

156(2), 620-628.

[83]   Farkhondeh, M., Safari, M., Pritzker, M., Fowler, M., Han, T., Wang, J., & Delacourt, C.

(2014). Full-range simulation of a commercial LiFePO$_4$ electrode accounting for bulk and

surface effects: a comparative analysis. *Journal of The Electrochemical Society, 161(3),*

A201-A212.

[84] Doyle, M., Fuller, T. F., & Newman, J. (1993). Modeling of galvanostatic charge and discharge of the lithium/polymer/insertion cell. *Journal of the Electrochemical Society, 140(6),* 1526-1533.

[85] Thompson, A. H. (1979). Electrochemical potential spectroscopy: a new electrochemical measurement. *Journal of The Electrochemical Society, 126(4),* 608-616.

[86] Yabuuchi, N., Makimura, Y., & Ohzuku, T. (2007). Solid-State chemistry and electrochemistry of $LiNi_{1/3}Mn_{1/3}Co_{1/3}O_2$ for advanced lithium-ion batteries III. rechargeable capacity and cycleability. *Journal of The Electrochemical Society, 154(4)*, A314-A321.

[87] Thackeray, M. M., Johnson, P. J., De Picciotto, L. A., Bruce, P. G., & Goodenough, J. B. (1984). Electrochemical extraction of lithium from $LiMn_2O_4$. *Materials Research Bulletin, 19(2)*, 179-187.

[88] Chikkannanavar, S. B., Bernardi, D. M., & Liu, L. (2014). A review of blended cathode materials for use in Li-ion batteries. *Journal of Power Sources, 248,* 91-100.

[89] Kim, H. S., Kong, M., Kim, K., Kim, I. J., & Gu, H. B. (2009). Electrochemical characteristics of $LiFePO_4/LiCoO_2$ mixed electrode for Li secondary battery. *Journal of Electroceramics, 23(2-4),* 219-224.

[90] Qiu, C., Liu, L., Du, F., Yang, X., Wang, C., Chen, G., & Wei, Y. (2015). Electrochemical performance of $LiMn_2O_4/LiFePO_4$ blend cathodes for lithium ion batteries. *Chemical Research in Chinese Universities. 31(2),* 270-275.

[91] Darling, R., & Newman, J. (1997). Modeling a porous intercalation electrode with two characteristic particle sizes. *Journal of The Electrochemical Society, 144(12*), 4201-4208.

[92] Arora, P., Doyle, M., & White, R. E. (1999). Mathematical modeling of the lithium deposition overcharge reaction in lithium-ion batteries using carbon‐based negative electrodes. *Journal of The Electrochemical Society, 146(10),* 3543-3553.

[93] Nagarajan, G. S., Van Zee, J. W., & Spotnitz, R. M. (1998). A mathematical model for intercalation electrode behavior I. effect of particle-size distribution on discharge capacity. *Journal of the Electrochemical Society, 145(3),* 771-779.

[94] Thomas-Alyea, K. E. (2008). Modeling resistive-reactant and phase-change materials in battery electrodes. *ECS Transactions, 16(13),* 155-165.

[95] Amoli, B. M., Gumfekar, S., Hu, A., Zhou, Y. N., & Zhao, B. (2012). Thiocarboxylate functionalization of silver nanoparticles: effect of chain length on the electrical conductivity of nanoparticles and their polymer composites. *Journal of Materials Chemistry, 22(37),* 20048-20056.

[96] Thomas-Alyea, K. E., & Newman, J. (2004). *Electrochemical Systems*.

[97] Majdabadi, M. M., Farhad, S., Farkhondeh, M., Fraser, R. A., & Fowler, M. (2015). Simplified electrochemical multi-particle model for LiFePO$_4$ cathodes in lithium-ion batteries. *Journal of Power Sources, 275*, 633-643.

[98]   Dargaville, S., & Farrell, T. W. (2010). Predicting active material utilization in LiFePO$_4$

electrodes using a multiscale mathematical model. *Journal of the Electrochemical*

Society, 157(7), A830-A840.

[99]   Stewart, S. G., Srinivasan, V., & Newman, J. (2008). Modeling the performance of

lithium-ion batteries and capacitors during hybrid-electric-vehicle operation. *Journal of*

The Electrochemical Society, 155(9), A664-A671.

[100] Safari, M., & Delacourt, C. (2011). Modeling of a commercial graphite/LiFePO$_4$ cell.

Journal of the Electrochemical Society, 158(5), A562-A571.

[101] Mathieson, I., Brewis, D. M., Sutherland, I., & Cayless, R. A. (1994). Pretreatments of

fluoropolymers. *The Journal of Adhesion, 46(1-4),* 49-56.

[102] Brewis, D. M., Mathieson, I., Sutherland, I., Cayless, R. A., & Dahm, R. H. (1996).

Pretreatment of poly (vinyl fluoride) and poly (vinylidene fluoride) with potassium

hydroxide. *International Journal of Adhesion and Adhesives, 16(2),* 87-95.

[103] Liu, Q. F., Lee, C. H., & Kim, H. (2010). Performance evaluation of alkaline treated poly

(vinylidene fluoride) membranes. *Separation Science and Technology, 45(9),* 1209-1215.

[104] Lee, J. D., & Yoon, H. J. (2012, June). The effect of Electrolyte on the Hybrid Capacitor

of LiMn$_2$O$_4$/AC and LiCoO$_2$/AC Prepared by Chemical Activation. *In Meeting Abstracts*

(No. 6, pp. 554-554). The Electrochemical Society.

[105] Lombardi, I., Bestetti, M., Mazzocchia, C., Cavallotti, P. L., & Ducati, U. (2004). Electrochemical characterization of carbon nanotubes for hydrogen storage. *Electrochemical and Solid-state Letters, 7(5),* A115-A118.

[106] Liu, L., Sun, K., Zhang, N., & Yang, T. (2009). Improvement of high-voltage cycling behavior of Li $(Ni_{1/3}Co_{1/3}Mn_{1/3})$ O_2 cathodes by Mg, Cr, and Al substitution. *Journal of Solid State Electrochemistry, 13(9),* 1381-1386.

[107] Jang, S. B., Kang, S. H., Amine, K., Bae, Y. C., & Sun, Y. K. (2005). Synthesis and improved electrochemical performance of Al (OH) 3-coated $Li[Ni_{1/3}Mn_{1/3}Co_{1/3}]O_2$ cathode materials at elevated temperature. *Electrochimica Acta, 50(20),* 4168-4173.

[108] Liu, X., Wang, J., Zhang, J., & Yang, S. (2006). Fabrication and characterization of Zr and Co co-doped $LiMn_2O_4$ nanowires using sol–gel–AAO template process. *Journal of Materials Science: Materials in Electronics, 17(11),* 865-870.

[109] Valdes, L. B. (1954). Resistivity measurements on germanium for transistors. *Proceedings of the IRE, 42(2),* 420-427.

[110] Ender, M., Weber, A., & Ivers-Tiffée, E. (2013). A novel method for measuring the effective conductivity and the contact resistance of porous electrodes for lithium-ion batteries. *Electrochemistry Communications, 34*, 130-133.

[111] Christensen, J., Srinivasan, V., & Newman, J. (2006). Optimization of lithium titanate electrodes for high-power cells. *Journal of The Electrochemical Society, 153(3),* A560-A565.

[112] Verbrugge, M. W., & Koch, B. J. (1996). Modeling lithium intercalation of single‑fiber carbon microelectrodes. *Journal of The Electrochemical Society, 143(2),* 600-608.

[113] Zhang, Q., Guo, Q., & White, R. E. (2006). A new kinetic equation for intercalation electrodes. *Journal of The Electrochemical Society, 153(2),* A301-A309.

[114] Christensen, J., & Newman, J. (2006). Stress generation and fracture in lithium insertion materials. *Journal of Solid State Electrochemistry, 10(5),* 293-319.

[115] Karthikeyan, D. K., Sikha, G., & White, R. E. (2008). Thermodynamic model development for lithium intercalation electrodes. *Journal of Power Sources, 185(2),* 1398-1407.

[116] Barker, J., West, K., Saidi, Y., Pynenburg, R., Zachau-Christiansen, B., & Koksbang, R. (1995). Kinetics and thermodynamics of the lithium insertion reaction in spinel phase $Li_xMn_2O_4$. *Journal of Power Sources, 54(2),* 475-478.

[117] Drezen, T., Kwon, N. H., Bowen, P., Teerlinck, I., Isono, M., & Exnar, I. (2007). Effect of particle size on $LiMnPO_4$ cathodes. *Journal of Power Sources, 174(2),* 949-953.

[118] Wagemaker, M., Borghols, W. J., & Mulder, F. M. (2007). Large impact of particle size on insertion reactions. A case for anatase Li_xTiO_2. *Journal of the American Chemical Society, 129(14),* 4323-4327.

[119] Sheu, S. P., Yao, C. Y., Chen, J. M., & Chiou, Y. C. (1997). Influence of the $LiCoO_2$ particle size on the performance of lithium-ion batteries. *Journal of Power Sources, 68(2),* 533-535.

175

[120] Cornut, R., Lepage, D., & Schougaard, S. B. (2012). Ohmic drop in LiFePO$_4$ based lithium battery cathodes containing agglomerates. *Journal of The Electrochemical Society, 159(6),* A822-A827.

[121] Garcıa, R. E., Chiang, Y. M., Carter, W. C., Limthongkul, P., & Bishop, C. M. (2005). Microstructural modeling and design of rechargeable lithium-ion batteries. *Journal of The Electrochemical Society, 152(1),* A255-A263.

[122] Dees, D. W., Abraham, D. P., Lu, W., Gallagher, K. G., Bettge, M., & Jansen, A. N. (2015). Electrochemical Modeling and Performance of a Lithium-and Manganese-Rich Layered Transition-Metal Oxide Positive Electrode. *Journal of The Electrochemical Society, 162(4),* A559-A572.

[123] Gowda, S. R., Dees, D. W., Jansen, A. N., & Gallagher, K. G. (2015). Examining the Electrochemical Impedance at Low States of Charge in Lithium-and Manganese-Rich Layered Transition-Metal Oxide Electrodes. *Journal of The Electrochemical Society, 162(7),* A1374-A1381.

[124] Gallagher, K. G., Dees, D. W., Jansen, A. N., Abraham, D. P., & Kang, S. H. (2012). A Volume Averaged Approach to the Numerical Modeling of Phase-Transition Intercalation Electrodes Presented for Li$_x$C$_6$. *Journal of The Electrochemical Society, 159(12),* A2029-A2037.

[125] Bach, P., Stratmann, M., Valencia-Jaime, I., Romero, A. H., & Renner, F. U. (2015). Lithiation and Delithiation Mechanisms of Gold Thin Film Model Anodes for Lithium Ion Batteries: Electrochemical Characterization. *Electrochimica Acta, 164*, 81-89.

[126] Birkl, C. R., McTurk, E., Roberts, M. R., Bruce, P. G., & Howey, D. A. (2015). A parametric open circuit voltage model for lithium ion batteries. *Journal of The Electrochemical Society, 162(12),* A2271-A2280.

[127] Du Pasquier, A., Blyr, A., Courjal, P., Larcher, D., Amatucci, G., Gerand, B., & Tarascon, J. M. (1999). Mechanism for Limited 55 C Storage Performance of $Li_{1.05}Mn_{1.95}O_4$ Electrodes. *Journal of The Electrochemical Society, 146(2),* 428-436.

[128] Tarascon, J. M., Gozdz, A. S., Schmutz, C., Shokoohi, F., & Warren, P. C. (1996). Performance of Bellcore's plastic rechargeable Li-ion batteries. *Solid State Ionics, 86,* 49-54.

[129] Thackeray, M. M., De Kock, A., Rossouw, M. H., Liles, D., Bittihn, R., & Hoge, D. (1992). Spinel Electrodes from the Li‑Mn‑O System for Rechargeable Lithium Battery Applications. *Journal of The Electrochemical Society, 139(2),* 363-366.

[130] Stiaszny, B., Ziegler, J. C., Krauß, E. E., Schmidt, J. P., & Ivers-Tiffée, E. (2014). Electrochemical characterization and post-mortem analysis of aged $LiMn_2O_4$–Li ($Ni_{0.5}$ $Mn_{0.3}Co_{0.2}$)O_2/graphite lithium ion batteries. Part I: Cycle aging. *Journal of Power Sources, 251,* 439-450.

[131] Wang, J., Purewal, J., Liu, P., Hicks-Garner, J., Soukazian, S., Sherman, E., & Verbrugge, M. W. (2014). Degradation of lithium ion batteries employing graphite negatives and nickel–cobalt–manganese oxide+ spinel manganese oxide positives: Part 1, aging mechanisms and life estimation. *Journal of Power Sources, 269,* 937-948.

[132] Waldmann, T., Wilka, M., Kasper, M., Fleischhammer, M., & Wohlfahrt-Mehrens, M. (2014). Temperature dependent ageing mechanisms in Lithium-ion batteries–A Post-Mortem study. *Journal of Power Sources, 262,* 129-135.

[133] Stiaszny, B., Ziegler, J. C., Krauß, E. E., Zhang, M., Schmidt, J. P., & Ivers-Tiffée, E. (2014). Electrochemical characterization and post-mortem analysis of aged $LiMn_2O_4$–NMC/graphite lithium ion batteries part II: Calendar aging. *Journal of Power Sources, 258,* 61-75.

[134] Röder, P., Stiaszny, B., Ziegler, J. C., Baba, N., Lagaly, P., & Wiemhöfer, H. D. (2014). The impact of calendar aging on the thermal stability of a $LiMn_2O_4$–Li $(Ni_{1/3}Mn_{1/3}Co_{1/3})$ O_2/graphite lithium-ion cell. *Journal of Power Sources, 268*, 315-325.

[135] Cordoba-Arenas, A., Onori, S., Guezennec, Y., & Rizzoni, G. (2015). Capacity and power fade cycle-life model for plug-in hybrid electric vehicle lithium-ion battery cells containing blended spinel and layered-oxide positive electrodes. *Journal of Power Sources, 278*, 473-483.

[136] Stevens, D. A., Ying, R. Y., Fathi, R., Reimers, J. N., Harlow, J. E., & Dahn, J. R. (2014). Using high precision coulometry measurements to compare the degradation

mechanisms of NMC/LMO and NMC-only automotive scale pouch cells. *Journal of The Electrochemical Society, 161(9),* A1364-A1370.

[137]   Käbitz, S., Gerschler, J. B., Ecker, M., Yurdagel, Y., Emmermacher, B., André, D., ... & Sauer, D. U. (2013). Cycle and calendar life study of a graphite| LiNi$_{1/3}$Mn$_{1/3}$Co $_{1/3}$O$_2$ Li-ion high energy system. Part A: Full cell characterization. *Journal of Power Sources*, 239, 572-583.

[138]   Schmalstieg, J., Käbitz, S., Ecker, M., & Sauer, D. U. (2014). A holistic aging model for Li(NiMnCo)O$_2$ based 18650 lithium-ion batteries. *Journal of Power Sources, 257,* 325-334.

[139]   Agubra, V., & Fergus, J. (2013). Lithium ion battery anode aging mechanisms. *Materials, 6(4),* 13   10-1325.

[140]   Broussely, M., Herreyre, S., Biensan, P., Kasztejna, P., Nechev, K., & Staniewicz, R. J. (2001). Aging mechanism in Li ion cells and calendar life predictions. *Journal of Power Sources, 97,* 13-21.

[141]   Ploehn, H. J., Ramadass, P., & White, R. E. (2004). Solvent diffusion model for aging of lithium-ion battery cells. *Journal of The Electrochemical Society, 151(3),* A456-A462.

[142]   Aurbach, D., Markovsky, B., Talyossef, Y., Salitra, G., Kim, H. J., & Choi, S. (2006). Studies of cycling behavior, ageing, and interfacial reactions of LiNi$_{0.5}$Mn$_{1.5}$O$_4$ and carbon electrodes for lithium-ion 5-V cells. *Journal of Power Sources, 162(2),* 780-789.

[143] Broussely, M., Biensan, P., Bonhomme, F., Blanchard, P., Herreyre, S., Nechev, K., & Staniewicz, R. J. (2005). Main aging mechanisms in Li ion batteries. *Journal of Power Sources, 146(1),* 90-96.

[144] Smith, A. J., Dahn, H. M., Burns, J. C., & Dahn, J. R. (2012). Long-term low-rate cycling of $LiCoO_2$/graphite Li-ion cells at 55 C. *Journal of The Electrochemical Society, 159(6)*, A705-A710.

[145] Agubra, V. A., Fergus, J. W., Fu, R., & Choe, S. Y. (2014). Analysis of effects of the state of charge on the formation and growth of the deposit layer on graphite electrode of pouch type lithium ion polymer batteries. *Journal of Power Sources, 270,* 213-220.

[146] Belharouak, I., Koenig, G. M., Tan, T., Yumoto, H., Ota, N., & Amine, K. (2012). Performance Degradation and gassing of $Li_4Ti_5O_{12}$/$LiMn_2O_4$ lithium-ion cells. *Journal of The Electrochemical Society*, 159(8), A1165-A1170.

[147] Mao, Z., Farkhondeh, M., Pritzker, M., Fowler, M., Chen, Z., & Safari, M. (2015). Model-based prediction of composition of an unknown blended lithium-ion battery cathode. *Journal of the Electrochemical Society*.162, A716-A721.

[148] Mao, Z., Farkhondeh, M., Pritzker, M., Fowler, M. & Chen, Z. (2016). Multi-particle model for a commercial blended lithium-ion electrode. *Journal of the Electrochemical Society*, 163, A458-A469